A zonal model for radiation heat transfer in coal-fired boiler furnaces

Prepared by:

Whitney Ogalaletseng Monnaemang

MNNWHI001

Department of Mechanical Engineering

University of Cape Town

Supervisor:

Professor P.G. Rousseau

Co-Supervisor:

Professor L. Jestin

August 2015

Submitted to the Department of Mechanical Engineering at the University of Cape Town in partial fulfilment of the academic requirements for a Master of Science degree in Mechanical Engineering.

Key Words: ZONAL METHOD, DIRECT EXCHANGE AREAS, RADIATION HEAT TRANSFER, BOILER FURNACE.

Abstract

Problems associated with boilers are a major contributor to load losses in coal-fired power plants. The boiler furnace exit temperature is a key indicator of the combustion and heat transfer processes taking place and has a profound impact on the operation of the heat exchangers downstream of the furnace. Having a model that can predict the furnace exit temperature and heat flux distributions may enable furnace performance to be predicted without having to conduct extensive experimentation. Also, comparing the results with measurements taken on the plant may enable the identification of operating problems and potential sources of losses.

Thermal radiation is the dominant mode of heat transfer in the boiler furnace. The primary objective of this study is to develop and implement a radiation heat transfer network solution methodology based on the zonal method that may be applied to boiler furnace modelling.

The zonal method allows for the prediction of heat flux and temperature distributions on the walls, inside, and at the exit of the furnace. Direct exchange areas are the basis of the zonal method and are a function of the furnace geometry and radiative properties of the walls and the participating medium that fills the furnace volume. The evaluation of direct exchange areas is done by discrete numerical integration, after which it needs to be smoothed to satisfy energy conservation. After evaluating two different smoothing techniques, the least squares technique using Lagrange multipliers was selected for this study. Following this, the solution of the radiation heat transfer network was implemented for an emitting-absorbing-scattering participating medium for two different scenarios, namely (*i*) solving surface and volume heat fluxes for known surface and medium temperatures, and (*ii*) solving surface heat fluxes and medium temperature distributions for known surface temperatures and volume heat source terms.

Intermediate verification and validation steps throughout the development process show good agreement with other numerical techniques and correlations available in literature. In order to illustrate the applicability of the final model, a number of case studies are conducted. These include an illustration of the effect of slagging on the furnace walls, of a faulty burner and of changes in the radiative properties of the participating medium. The results of the case studies show that the trends of the heat flux and temperature distributions obtained with the new model are in agreement with those found in literature.

Declaration

I, *Whitney Ogalaletseng Monnaemang*, hereby declare the work contained in this dissertation to be my own. All information which has been gained from various journal articles, text books or other sources has been referenced accordingly. I have not allowed, and will not allow, anyone to copy my work with the intention of passing it off as their own work or part thereof.

signature removed

Signed by candidate

Whitney Ogalaletseng Monnaemang

Acknowledgements

The author wishes to thank and express her gratitude towards:

- First and most importantly, the Heavenly father for His unfailing love, sufficient grace and His mercies that are new every morning. He has, without fail, blessed the author with the spiritual strength, patience, courage and wisdom to conduct this study.
- Secondly, the THRIP programme and its industrial partner M-Tech Industrial (Pty) Ltd as well as the National Research Foundation for providing the funding that enabled the opportunity to further the author's studies.
- Thirdly, the Eskom Power Plant Engineering Institute specialisation centre in Energy Efficiency for the opportunity to participate in the programme.
- Fourthly, the author wishes to thank her supervisor, Prof Pieter Rousseau for his invaluable contributions to this research study and all the motivational speeches.
- Next, Prof Louis Jestin and Dr Wim Fuls for their useful contributions and assistance in this study.
- Last but not least, the author is grateful for the love, prayers, motivation and support she received from her family and friends.

Table of Contents

List of Figures

List of Tables

List of Nomenclature

General symbols

B	Enclosure side length, [m]
CO	Carbon monoxide
CO_2	Carbon dioxide
D	Particle diameter, [μm]
F_{ij}	View factor
f_v	Volume fraction
g_i	Row-sum constraints
g_i^*	Column-sum constraints
$H_2O(v)$	Water vapour
H	Irradiation, [kW/m^2]
J	Radiosity, [kW/m^2]
k	Refractive index of refraction
L, W & H	Enclosure length, width & height, [m]
m	Complex index of refraction
n	Absorptive index of refraction
N	Total number of zones (volume zones + surface zones)
N_{gg}	Number of gray gases
N_g	Number of Volume zones
N_p	Particle number density [number of particles/m^3]
N_s	Number of Surface zones
NO	Nitrogen monoxides
NO_x	Oxides of nitrogen
Q_{abs}	Absorption efficiency factor
Q_g	Volume radiative heat transfer rate, [kW]
Q_s	Surface radiative heat transfer rate, [kW]
Q_{sca}	Scattering efficiency factor
q_g	Volume radiative heat transfer flux, [kW/m^2]
q_s	Surface radiative heat transfer flux, [kW/m^2]

SO_2	Sulphur dioxide
$\overline{s_i s_j}$, $\overline{s_i g_j}$, $\overline{g_i g_j}$	Surface-to-surface, Surface-to-volume, Volume-to-volume direct exchange areas, [m^2]
$\overline{S_i S_j}$, $\overline{S_i G_j}$, $\overline{G_i G_j}$	Surface-to-surface, Surface-to-volume, Volume-to-volume total exchange areas, [m^2]
T, U, S, V, Q, W, R, X	Zonal method energy balance matrices
T	Temperature, [K]
T_g	Gas/medium temperature, [K]
T_s	Surface temperature, [K]
x_{ij}	Originally approximated direct exchange area value, [m^2]
$x_{ij}^{'}$	Adjusted direct exchange area value, [m^2]

Greek symbols

α	Absorptivity
β	Extinction coefficient, [m^{-1}]
δ	Kronecker's delta
ε	Emissivity
ε_g	Total gas emissivity
κ	Absorption coefficient, [m^{-1}]
λ	Lagrange multipliers
ρ	Reflectivity
σ_s	Scattering coefficient, [m^{-1}]
σ	Boltzmann constant (= 5.67 x 10^{-8} W/m^2K^4)
ω	Scattering albedo (σ_s/β)
Γ	Gamma function

Acronyms and Abbreviations

CFD	Computational fluid dynamics
DEAs	Direct exchange areas
DFAs	Directed flux areas
DOM	Discrete ordinates method
EBWM	Exponential wide band model

EPPEI	Eskom Power Plant Engineering Institute
FVM	Finite volume method
HRSG	Heat Recovery Steam Generator
RHT	Radiation heat transfer
RTE	Radiative transfer equation
SGG	Simple gray gas
TEAs	Total exchange areas
WSGG	Weighted sum of gray gases

1. Introduction

1.1 Background and motivation

Despite the calls for moving towards larger utilisation of renewable energy sources, the role of coal remains crucial. Coal is regarded the world's most abundant fossil fuel (WNA, 2015) and is used in coal-fired power plants as the key ingredient for the production of electricity. According to the World Coal Association (WCA), coal generates more than 40% of the global electricity supply (WCA, 2014). This is also illustrated in Figure 1.1:

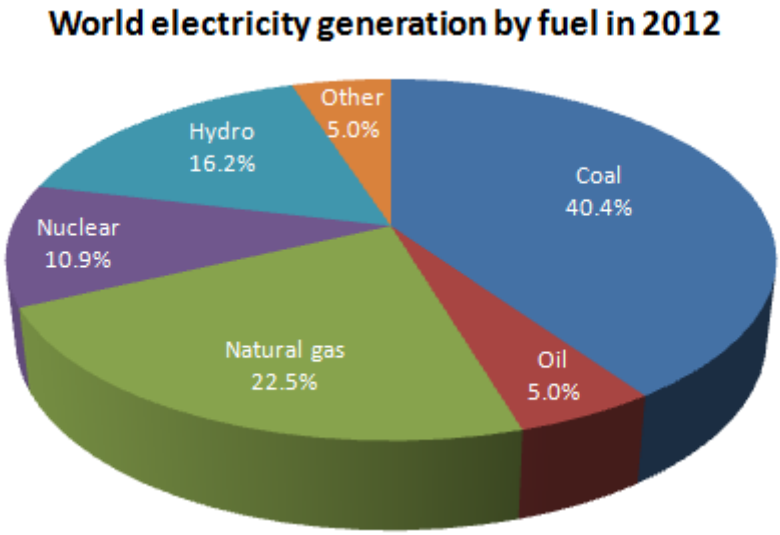

Figure 1.1. World electricity generation by fuel in 2012 (IEA, 2014).

Eskom uses coal to generate about 95% of the electricity in South Africa (de Groot, et al., 2013). The availability of electricity has become an important part of society especially since electricity is regarded as one of the basic needs of life following water and food. As a result, it is vital that the electricity generation process is continuously enhanced to sustain electricity for future civilization.

Nowadays, much attention is given to increasing the overall efficiency of power plants and to reducing the emission of pollutants when burning fossil fuels (Ameri & Shamshirgaran, 2008). The efficiency, availability and environmental impact of pulverised coal-fired power plants are directly dependent on boiler efficiency, downtime and emissions control. The major contributors to inefficiency are heat being carried away in the flue gas, boiler ingress air and leakage in air-heaters. Furthermore, tube failures leading to downtime are often caused by overheating due to excessive fouling.

This highlights a need for heat transfer simulations that can model the mechanisms governing thermal performance. Such simulations offer among other benefits, the benefit of conceptualising original plant designs more efficiently and effectively in shorter times. Another benefit is that they also offer the advantage of allowing the identification and implementation of improvements to existing plants more readily.

The EPPEI (Eskom Power Plant Engineering Institute) Specialization Centre in Energy Efficiency at the University of Cape Town is developing an integrated whole-plant process model of a generic coal-fired power plant. The motivation for engaging in this study is to contribute towards the development of the process model with specific focus on the boiler furnace model where radiation heat transfer is the dominant mode of heat transfer. The model will not be based on the radiative transfer equation (RTE) as is typically the case in conventional computational fluid dynamics (CFD) approaches. It will rather employ the zonal method that has been used extensively to solve radiation heat transfer problems.

The application of the zonal method allows for the prediction of heat flux and temperature distributions inside, on the walls and at the exit of the furnace. A model that can predict heat flux and temperature distributions could be a valuable component in power plant analyses. Comparing the models' results with measurements taken on the plant may enable the identification of operating problems, potential sources of losses and encourage the optimisation of soot blowing procedures to control slagging and fouling. Being able to simulate the operation of the boiler furnace integrated with the rest of the power plant may further enable control optimisation studies. Such optimisation could lead to better balancing between the demands of accurate and responsive load control with the demand for high thermal efficiency, availability and extended plant life expectancy.

1.2 The research problem

Problems associated with boilers are a major contributor to load losses in coal-fired power plants. The boiler furnace flue gas exit temperature is a key indicator of the combustion and heat transfer processes taking place and has a profound impact on the operation of the heat exchangers downstream of the furnace.

Having a model that can predict the furnace exit temperature as well as heat flux distributions may enable furnace performance to be predicted reliably without having to conduct extensive experimentation.

Thermal radiation is the dominant mode of heat transfer in the furnace and is complicated by the fact that the furnace volume contains a participating medium. The radiative transfer equation (RTE) has been the traditional way for solving radiation heat transfer in high temperature industrial systems for many years. However, the challenge in deriving an analytical solution to the integro-differential RTE in the presence of a participating medium has led to the development of a variety of alternative numerical methods over the last few decades (Lari & Nassab, 2011). The numerical methods include but are not limited to the flux method, zonal method and the Monte Carlo method. According to Batu and Selcuk (2002), the zonal method is known to offer a good compromise between accuracy and computational effort (Batu & Selcuk, 2002). In this method, the enclosure representing the furnace is divided into a finite number of volume zones and surface zones that are assumed to be isothermal and have uniform radiative properties (Hottel & Cohen, 1958). Energy balances are performed between every pair of zones by applying pre-calculated direct exchange areas. This process leads to a set of simultaneous equations for solving heat flux and temperature distributions (Modest, 2013).

1.3 The objectives of the study

The primary objective of this study is to develop and implement a radiation heat transfer network solution methodology based on the zonal method that may be applied in boiler furnace modelling.

The secondary objectives set up to meet the primary objective of this study are as follows:

I. Implement a numerical integration technique for the calculation of the direct exchange areas in a three-dimensional enclosure (boiler furnace) filled with a participating medium.
II. Develop a radiation heat transfer network solution model based on the zonal method for an enclosure representing a boiler furnace.
III. Verify and validate the implementation of the network model by comparing results with that of existing graphical techniques and other data available in literature.
IV. Conduct case studies using the network model to illustrate its applicability for boiler furnace modelling.

1.4 The assumptions and scope of the study

Important assumptions applicable to this study are:

I. Appropriate heat source terms representing the combustion flame behaviour are available; hence, heat source values are not calculated but may be specified within appropriate volume zones.
II. The input parameters relating to the properties of the participating medium are readily available from a combustion model upstream of the model developed in this study.

The scope of the study is not to extensively study the radiative properties of the participating medium since they are strongly depend on the coal combustion process which does not form part of the scope of the study. Hence, the primary model is developed based on the assumption that the radiative properties (absorption and scattering coefficients) of the participating medium are available and therefore provided as fixed inputs to the network model. However, for the sake of completeness in cases where the radiative properties are not available, a secondary model is also implemented that uses simplified approximations to estimate the radiative properties of the participating medium based on other input parameters.

The software package that is identified as the platform for developing the radiation heat transfer network solution methodology is Scilab. Scilab is an open source numerical computational software package.

1.5 The dissertation outline

The research outline of this study is as follows:

I. Following the introduction chapter, Chapter 2 provides a literature review pertaining to the zonal method and other relevant material.
II. To gain an appreciation and understanding for the study, the relevant theory is presented in Chapter 3.
III. Chapter 4 presents the heart of the study. In this chapter, the steps taken towards developing the radiation heat transfer network solution methodology are presented.
IV. In Chapter 5, the results and discussions are portrayed in the form of case studies using the network model to illustrate its applicability to boiler furnace modelling.

V. Based on the preceding chapters, conclusions are drawn and recommendations for future studies are made in Chapter 6.

2. Literature review

2.1 Introduction

This chapter contains a review of published literature that may serve as background for the study. It is divided into five sections which include a broad overview of coal-fired power plants given in terms of the heat transfer, combustion as well as the emissions in coal-fired power plants. The subsequent section addresses the application of the zonal method by other researchers. This includes a celebrated example used by multiple researchers to validate their radiation heat transfer models. Applications of the weighted sum of gray gasses (WSGG) model which is used in modelling the non-gray behaviour of gases are also addressed. Finally, a summary of what was learnt from the literature review and will be applied to the present study is presented.

2.2 Coal-fired power plant overview

A coal-fired power plant burns coal to eventually produce electricity (Mahamud, et al., 2013). The process starts off where pulverisers are used to mill coal to a fine powder. Pulverised coal and hot air driven by a forced draught fan from an air-heater is then introduced through burners to the combustion chamber of the boiler furnace wherein it is ignited to form an intense flame. During the energy conversion process in the combustion chamber, the carbon in coal reacts with the oxygen in air. During this exothermic combustion reaction, the chemical energy in coal is released as heat to create high temperatures inside the boiler. The energy conversion by the burning of coal is absorbed by the high pressure (produced by the feedwater pump which is located at the inlet of the boiler) demineralised water in tubes enclosing the boiler to generate steam. The generated steam then enters a superheater or number of superheaters wherein the steam is further heated resulting in the further increase of temperature. High pressure, high temperature steam then enters the turbine, wherein it acts as a working fluid that expands through multiple blade rows towards a lower pressure and converts the energy in the steam into mechanical energy. The mechanical energy is then transferred to the generator to convert to electrical energy. The condensed steam from the turbine is circulated back to the boiler with the aid of feedwater pumps. The electrical energy is finally transferred to the grid through a transformer from where it is fed to the final consumer (Baukal, 2000).

2.2.1 Heat transfer in the boilers of coal-fired power plants

In the boiler, the economisers, water walls (evaporators) and superheaters are the main heat transfer components. Economisers are mostly exposed to convection heat transfer and are placed after the superheater zone in the flue gas path (Teir & Jokivuori, 2002). Demineralised pressurised water from the feedwater pump enters the economiser wherein the water is heated by the flue gas coming from the superheater zone. The water leaves the economiser at a saturation temperature while ensuring that the flue gas temperature remains above the dew point of the gases to prevent corrosion of the precipitators and the ducts (Teir & Jokivuori, 2002). The saturated water leaving the economiser enters the water walls which are located in the high temperature zones of the furnace. The greater part of heat transfer takes place in the water walls (evaporators) where radiation heat transfer is the dominant mode of heat transfer (Palmqvist, 2012). The tube alignment in the furnace is usually vertical but may also be spiral at an angle along the furnace walls. As a result, the water/steam distribution is more uniform since the differences in heat fluxes are smoothed as the water/steam wraps around the boiler furnace (Palmqvist, 2012).

Convection and radiation heat transfer are the two dominating modes of heat transfer in the superheaters depending on whether convection or radiation based superheaters are used. Convection superheaters are used in the case of low steam temperatures and the heat from the flue gas is transferred mainly through convection. These superheaters are located after the furnace. Radiation superheaters on the other hand are used to obtain higher steam temperatures and the heat transfer from the flue gas is mainly through radiation. Radiation superheaters are placed at the top of the furnace within the reach of the flame radiation. They are usually integrated as tubes making up part of the boiler walls or they are built as plates hanging from the roof of the boiler (Wahlberg, 2011). Figure 2.1 is an illustration of a basic Heat Recovery Steam Generator (HRSG) showing the three components discussed namely; an evaporator, superheater and economiser (Wahlberg, 2011):

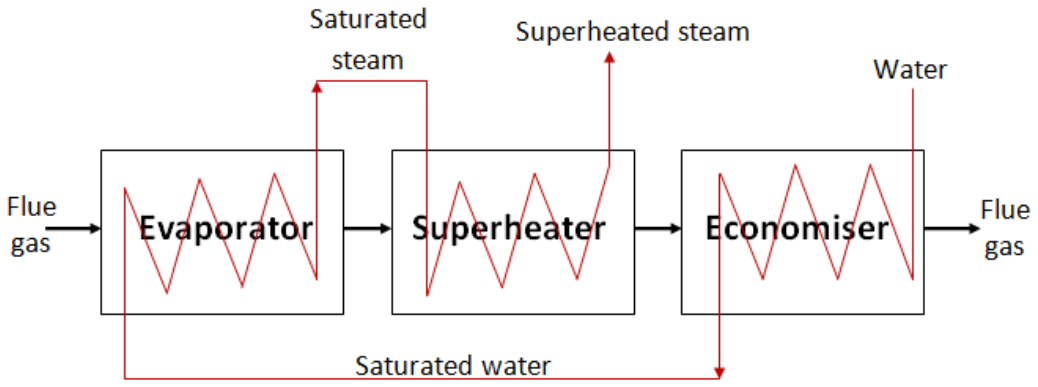

Figure 2.1. Basic Heat Recovery Steam Generator (Wahlberg, 2011).

A component that is not shown in Figure 2.1 is a reheater which is normally located upstream of the economiser, that is downstream of the superheater. Superheated steam from the superheater is sent to the high pressure steam turbine. Steam coming from the high pressure turbine passes through the reheater from which it goes to the intermediate pressure turbine. Figure 2.2 shows a detailed schematic of a boiler with its heat transfer components.

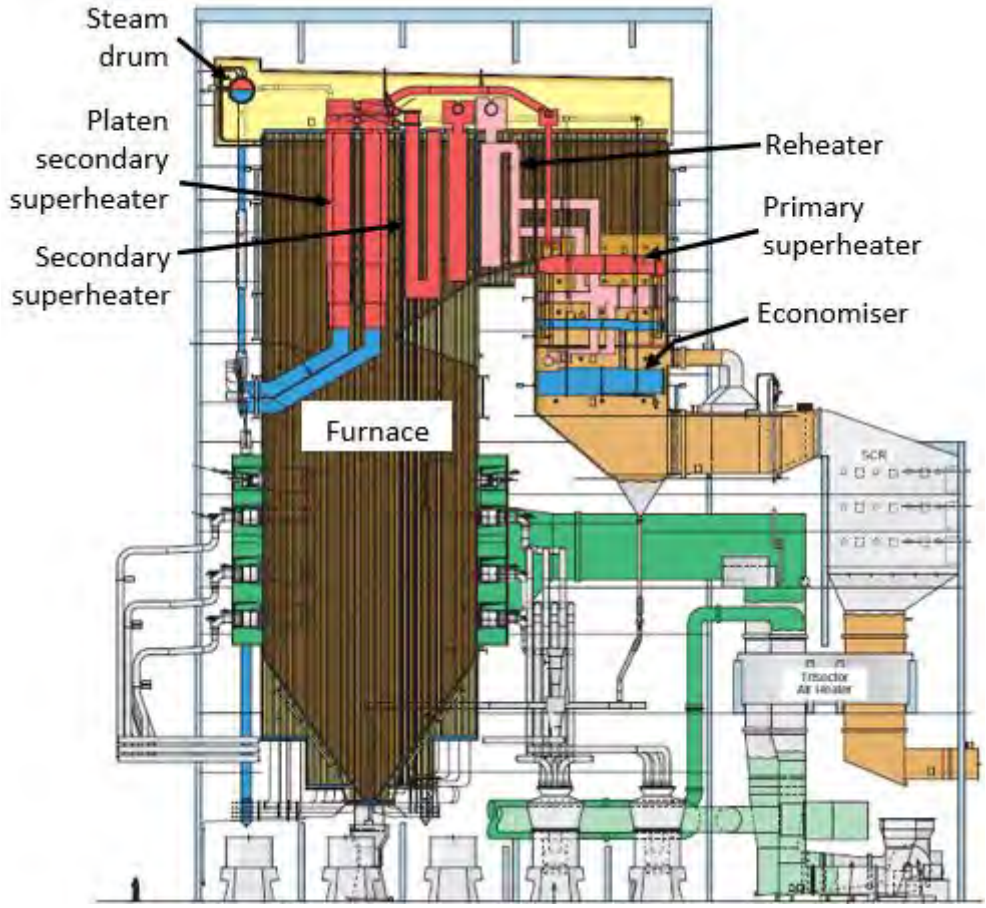

Figure 2.2: Detailed boiler (Kitto & Stultz, 2005).

2.2.2 Combustion in coal-fired power plants

Combustion is the release of energy from a fuel and oxidiser chemical reaction in a controlled environment (Baukal, 2000). This is in contrast to fires or explosions which are usually uncontrolled and undesirable. The majority of the combustion processes present in industrial systems uses hydrocarbons as a fuel. A generalised combustion reaction for a common hydrocarbon fuel and oxidiser can be written as follows (Baukal, 2000):

$$\text{Fuel} + \text{Oxidiser} \rightarrow CO_2 + H_2O + \text{Other species} \tag{2.1}$$

The most commonly used oxidiser is air, which consists of nearly 79% N_2 by volume with most of the balance being O_2. The "Other species" depends on the type of oxidiser and fuel being used as well as the fuel to oxidiser ratio. When coal is used as the fuel, the "Other species" are the particles suspended in the combustion gases and can either be characterised as carbonaceous (char, coal and soot) material or non-carbonaceous (fly-ash) material (Baukal, 2000). The particle size of the coal sample does not remain constant during the combustion process. Swelling takes place followed by a decrease in particle size during the devolatilisation stage as the volatile matter burns and the hydrogen present in the coal sample is converted into water vapour. During char burnout, the fixed carbon is oxidised to carbon dioxide; leaving behind a residue namely, ash (Hua, et al., 2005). The ash that does not fall through the boiler hopper is referred to as fly-ash. Fly-ash continue to radiate in the boiler, therefore making the ash content in the coal sample an important part of the radiation characteristic of the medium in the furnace (Baukal, 2000).

2.2.3 Coal-fired power plant emissions

Coal-fired power plants are significant sources of air pollutants such as oxides of sulphur (SO_x) and nitrogen (NO_x), plus carbon monoxide (CO), particulate matter and trace pollutants (Mahamud, et al., 2013). The oxidation of the nitrogen in the coal as well as the oxidation of the nitrogen in the combustion air produces the oxides of nitrogen (Liu, et al., 2013). NO_x formation is exponentially dependent on flue gas temperature. Minor reductions in the coal combustion flame temperature can result in the drastic reduction of NO_x emissions thus making NO_x formation highly temperature dependent (Baukal, 2000). However, lower coal combustion flame temperatures often reduce radiation heat transfer from the coal combustion flame (Baukal, 2000). This is due to the fact that

radiation heat transfer is proportional to the fourth power of the absolute temperature (Incropera, et al., 2007) of the participating medium. Furthermore, a reduction in NO_x results in an increase in carbon monoxide (CO) concentrations, whereas an increase in CO concentrations is an indication of an incomplete combustion which reduces combustion efficiency (Baukal, 2000).

Internal flue gas recirculation is mostly used to reduce NO_x emissions and to increase thermal efficiency (Baukal, 2000). Thermal efficiency is increased by using some of the energy in the exhaust flue gas to preheat the incoming combustion oxidiser, which is air in most cases (Baukal, 2000). This not only results in reduced flame temperatures, but also reduced NO_x emissions.

2.3 The zonal method applications

Hottel and Cohen introduced the zonal method in 1958. They developed the zonal method for analysing radiation heat transfer in an enclosure containing an emitting, absorbing and non-scattering gray gas with a constant absorption coefficient (Hottel & Cohen, 1958). In 1967, Hottel and Sarofim enhanced this method to cater for more complex three-dimensional geometries with non-gray absorption coefficients as well as with isotropically scattering media (Hottel & Sarofim, 1967). Since then, the zonal method has been widely used by researchers for modelling radiation heat transfer in high temperature industrial systems such as boiler furnaces.

Hottel and Sarofim (1965) used the zonal method to study the effect of plug flow and parabolic flow patterns on gas temperature and surface heat flux distributions in cylindrical furnaces. Gas temperature distributions were found to decrease more rapidly near the walls of the furnace compared to centre of the furnace (Hottel & Sarofim, 1965).

Surface heat fluxes on the other hand were found to be at maximum near the burners and decreased along the height of the furnace as the gas temperature decreased (Hottel & Sarofim, 1965).

Yin and Jaluria (1997) employed the zonal method to model radiation heat transfer in an optical fiber drawing furnace. The drawing of optical fiber requires a cylindrical glass preform to be heated to a temperature of above 1900 K in a furnace wherein the preform is considered a semi-transparent participating medium. They compared the traditional approach for modelling radiation heat transfer in such a furnace, namely the optically thick approximation method to the zonal method by studying the effect of various axial furnace temperatures and radial preform temperatures on heat flux distributions. They concluded that the zonal method produced accurate heat flux results

regardless of the radial preform temperature distribution, whilst the optically thick approximation method produced adequate heat flux results only when the variation within the preform temperature was as small as 5 %. For higher temperature variations, the heat flux results predicted by the zonal method were found to be significantly higher than those of the optically thick approximation method. According to Yin and Jaluria (1997), the difference in the heat flux results of the two methods were due to the fact that the zonal method considered interior emission whereas the optically thick approximation method did not. The limitation of the optically thick approximation method makes its application unfavourable when working with large diameter furnaces since large diameters give rise to varying radial temperatures. Furthermore, a variation in axial furnace temperatures resulted in comparable heat fluxes for both methods, thus indicating that the optically thick approximation method is applicable for a wide range of axial furnace temperature distributions (Yin & Jaluria, 1997). As a result, the use of the optically thick approximation method is recommended only in cases where small furnace diameters are used since temperature variation is then mainly in the axial direction. The zonal method on the other hand yields accurate results for both large and small furnace diameters (Yin & Jaluria, 1997).

Batu and Selcuk (2002) modelled the radiation heat transfer in the freeboard of a fluidised bed combustor using the zonal method. They treated the freeboard area of the combustor as a three-dimensional rectangular enclosure containing an emitting, absorbing and scattering medium. Figure 2.3 shows a comparison between measurements taken from the combustor test rig and the predictions from the zonal method (Batu & Selcuk, 2002):

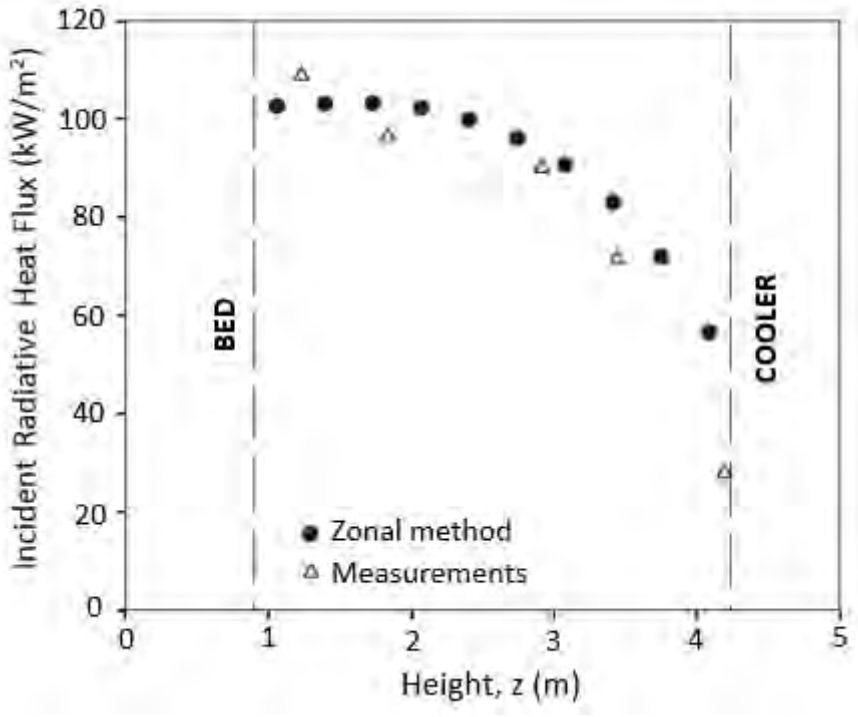

Figure 2.3. Incident radiative heat fluxes on the freeboard wall (Batu & Selcuk, 2002).

It is clear from Figure 2.3 that incident radiative heat flux decreases from the bed surface (bottom) toward the cooler surface (top) and the predictions of the zonal model are in good agreement with measurements taken from the combustor test rig (Batu & Selcuk, 2002).

Bordbar and Hyppänen (2007) employed the zonal method to predict the temperature and heat flux distributions in a utility boiler furnace. From their study, they concluded that the zonal method is one of the most accurate numerical methods for modelling radiation heat transfer in industrial furnaces. Moreover, they emphasised that the complex geometries of real industrial furnaces should be replaced by simpler geometries such as rectangular enclosures that will better suit the zonal method. A major criterion in this method is establishing the best size for the surface and volume zones for conducting the numerical calculations. Selecting a very fine mesh will not only lead to complicated numerical calculations but it may also increase the round off errors during the numerical calculation. A very coarse mesh on the other hand may be unable to adequately explain the details of the radiation heat transfer phenomena inside the boiler furnace (Bordbar & Hyppänen, 2007).

Zamaniyan et al. (2008) developed a combined mathematical model for the simulation of a top fired methane steam reformer using two sub-models, namely a reactor model and a furnace model.

They used a heterogeneous one-dimensional model to model the reactor and the zonal method to model the radiation heat transfer in the furnace. Although computational fluid dynamics can be used to model the combustion and flame behaviour in enclosures, they used an empirical correlation. Their furnace model is based on constant surface temperatures and different emissivity values for firing-end walls. The heat source term is uniformly distributed in all the volume zones inside the furnace and the medium contained in the furnace is assumed to be emitting and absorbing with no scattering. The results from the model indicated that the highest temperatures are located at the flame centre zones (Zamaniyan, et al., 2008). Zamaniyan et al. (2008) also studied the effect of a varying extinction coefficient on gas temperature, which is illustrated in Figure 2.4:

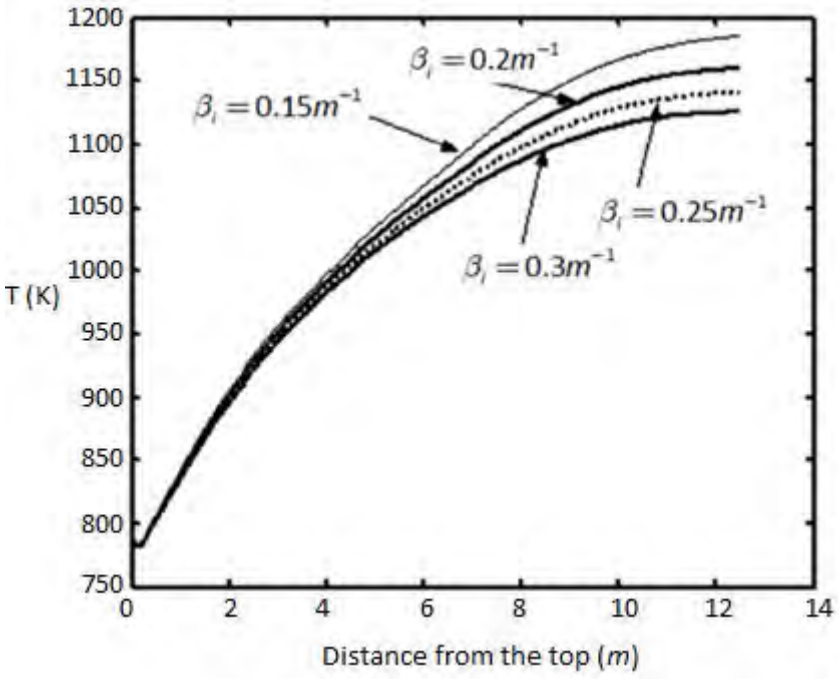

Figure 2.4. Effect of extinction coefficient on gas temperature (Zamaniyan, et al., 2008).

The extinction coefficient is a medium radiative property which is a result of the combined effect of the absorbing and scattering coefficients of a medium and has the unit of inverse distance. The absorption coefficient is defined as the inverse of the path that a beam of radiation will travel before being absorbed. The scattering coefficient is defined as the inverse of the path that a beam of radiation will travel before being scattered (Kumar, 2011). From Figure 2.4 it is evident that a decrease in the extinction coefficient results in the increase of gas temperature. This profile signifies that higher extinction coefficients results in more energy absorption by the combustion medium and less energy being transferred to the reactor (Zamaniyan, et al., 2008).

Cui et al. (2010) developed a mathematical model based on the zonal method for a combustion chamber containing gases with non-gray radiative properties. The radiative properties of the non-gray medium were calculated using the exponential wide band model (EBWM). The direct exchange areas were determined using the three-point Gauss-Legendre integral formula (Cui, et al., 2010).

Next, the total exchange areas were calculated using the Gauss-elimination method, and then finally the energy balances were solved using the variable-correction method. They used the heat flux and temperature distribution results obtained from the model to also study the effect of flame distribution on heat transfer. They used a reheating furnace that heat steel slabs as an example to verify and validate the model developed and compared the results obtained with a similar example. The two methods yielded good results with a maximum relative error of 1.97%. This implied that the developed model was reliable. As for the effect of flame distribution on heat transfer in the combustion chamber, they found that flame distribution has a significant influence on the gas temperature distribution while the flame temperature distribution had insignificant effects on both the slab heat flux and the slab surface temperature. Keeping in mind that the primary function of the reheating furnace is to heat slabs, the conclusion was drawn that the structure of the combustion chamber cannot be ignored in determining the height of the burners in the reheating furnace (Cui, et al., 2010).

Moghari et al. (2012) used the zonal method to predict thermal behaviour in a D-type water cooled steam boiler. Using this method, they found a reduction in the heat flux intensity near the corners of the walls, and that the maximum heat flux was in the front and the rear walls of the furnace where the burners were located. They also reported that the heat flux is highest at the centre of the walls because the central region is positioned best to receive radiation from the other walls as well as the furnace medium. Also, the closeness of the walls to the flame prevents the medium from sufficiently absorbing the radiative heat flux. This leads to a significant increase in the radiative heat flux incident on the walls. Figure 2.5 shows the amount of energy absorbed from the flue gas by every stage in the boiler (Moghari, et al., 2012):

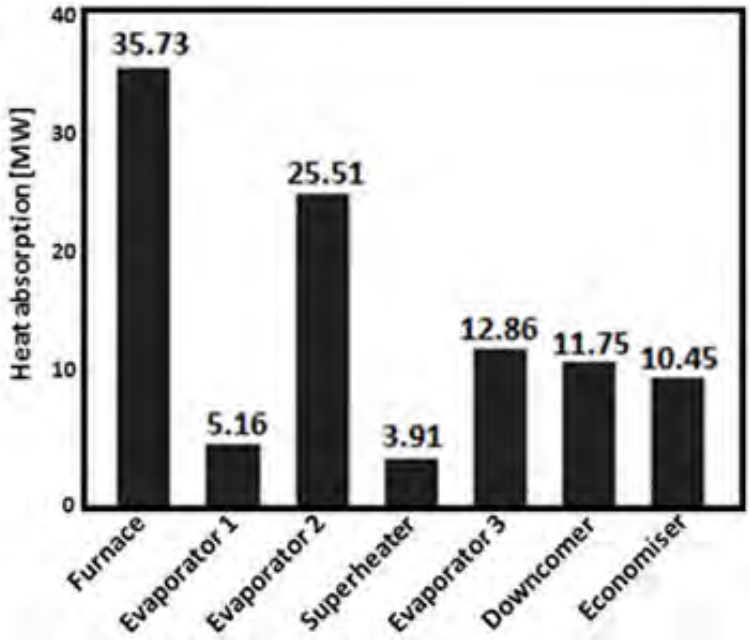

Figure 2.5. Heat absorption in different boiler stages (Moghari, et al., 2012).

From Figure 2.5, it is can be seen that the furnace absorbs the largest amount of energy (Moghari, et al., 2012). This makes the furnace one of the most important components in the boiler.

Gharehkhani et al. (2014) predicted the heat flux and temperature distributions on the walls and within a 150 MWe utility boiler containing a gas-soot mixture using the zonal method. The radiative properties of the gas-soot mixture were calculated using the weighted sum of gray gases model. They analysed scenarios in both the presence and absence of the soot and found that the presence of soot increased the heat flux on the boiler walls that resulted in the decrease of gas temperature. A similar result was reported by Méchi et al. (2010). This is due to the fact that soot enhances the radiation intensity since it radiates continuously throughout the wavelength spectrum. Furthermore, radiation heat transfer was concentrated towards the walls, which resulted in reduced gas temperatures since the gas absorbs radiation only in discrete bands of the wavelength spectrum. The predicted results showed good agreement with the measured data from the plant (Gharehkhani, et al., 2014).

2.3.1 Celebrated case study

Radiation heat transfer in a three-dimensional rectangular enclosure containing an emitting and absorbing participating medium has been studied by numerous researchers.

Figure 2.6 shows a schematic representation of an idealised furnace that was used for the analysis of radiation heat transfer by Mengüc & Viskanta (1985), Chai et al. (1994), Borjini et al. (2003) and Ebrahimi et al. (2004), just to mention a few:

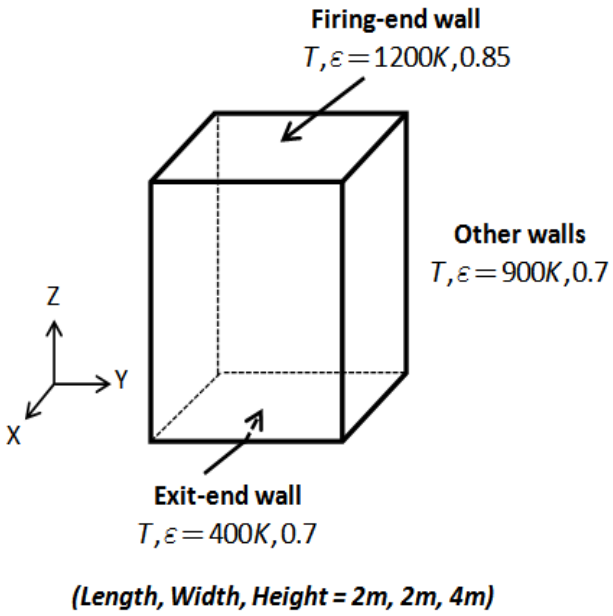

Figure 2.6. 3-Dimensional rectangular enclosure containing a participating medium (Ebrahimi, et al., 2004).

The medium enclosed by the furnace in Figure 2.6 has an extinction coefficient of 0.5 m^{-1} with a uniform internal heat source of 5 kW/m^3.

Mengüc and Viskanta (1985) used the first-order and third-order spherical harmonics approximation to predict gas temperature distributions in the furnace. For the purpose of validating the method used, they then compared the results obtained to the zonal method. They found that the methods used yielded similar results at the centre of the enclosure while there were deviations in the order of 5% between the two methods at the lower and upper parts of the enclosure. The deviations however decreased with increased optical thickness (Mengüc & Viskanta, 1985).

Chai et al. (1994) and Borjini et al. (2003) used the finite volume method (FVM) to investigate the problem at hand and found that the gas temperature distributions obtained were in good agreement with the zonal method.

Ebrahimi et al. (2004) used the zonal method to analyse the radiation heat transfer problem by also computing gas temperature distributions. They compared the results obtained to those of Borjini et al. (2003). The comparison is portrayed in Figure 2.7:

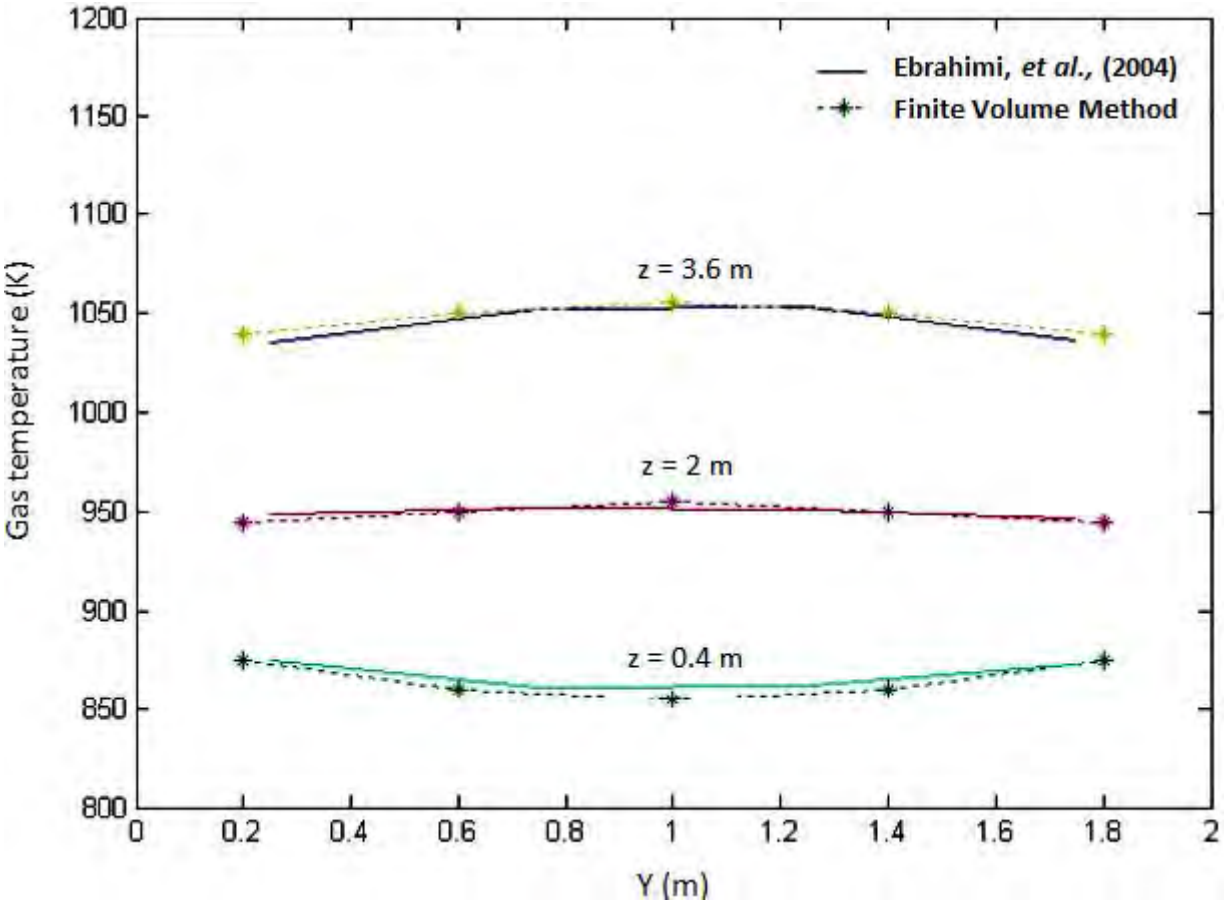

Figure 2.7. Gas temperature distribution along the length (Y) at three heights of the enclosure and the plane X=0.6 m (Ebrahimi, et al., 2004).

As can be seen, the results from the zonal method by Ebrahimi et al. (2004) and the FVM by Borjini et al. (2003) are in good agreement.

Given its wide application, this celebrated example will be a good case study for the validation of the radiation heat transfer network solution methodology to be developed in the current study.

2.4 Weighted sum of gray gases model applications

The weighted sum of gray gasses (WSGG) model was introduced by Hottel and Sarofim in 1967 around the same time when Hottel and Sarofim (1967) enhanced the zonal method to cater for non-gray participating media. The WSGG model has since gained its popularity for the calculation of non-gray (real) gas radiative properties. A non-gray gas is a gas of which its radiative properties are dependent on wavelength (Siegel & Howell, 1972). In this model, the non-gray gas is replaced with a finite number of gray gases of which one of them is a transparent gas.

Radiative heat fluxes are then evaluated independently for each gas after which the final heat fluxes are obtained from multiplying the respective radiative heat fluxes with a weighting factor and then adding the different contributions (Hottel & Sarofim, 1967). Smith et al. (1982) and Truelove (1976) among others investigated the determination of the weighting factors required for the WSGG model. According to Lallemant et al. (1996), the results of the total emissivity when using the WSGG model deviates from the line-by-line spectral model which is one of the most accurate models in radiative properties analyses by about 5% (Lallemant, et al., 1996).

Liu et al. (1998) conducted a comparative study of radiation heat transfer modelling in gas-fired furnaces using the simple gray gas (SGG) and the weighted sum of gray gases (WSGG) models and solved the radiative transfer equation (RTE) using the discrete ordinates method (DOM). They found that the use of the SGG model resulted in noteworthy errors when compared to the WSGG model results for the case when the temperature distributions are specified and the RTE is solved for the wall heat flux distributions. Consequently, they concluded that the WSGG model predicted more accurate heat fluxes and gas temperature distributions compared to the SGG model (Liu, et al., 1998).

Boutoub et al. (2006) used the WSGG model to investigate the radiative properties of non-gray participating media and coupled the model to the finite volume method (FVM) to solve the radiative transfer equation. In the study, they used four gray gases (3 + 1 transparent gas) and applied the model to a gas turbine combustion simulator in order to predict radiative heat fluxes. Upon comparison of the model with experimental measurements, satisfactory agreements of the radiative wall flux results were achieved (Boutoub, et al., 2006).

2.5 Summary

It is evident that the zonal method has influenced and contributed extensively to the evaluation of radiation heat transfer problems. This method aids in conducting case studies and sensitivity analyses on the systems to gain an in-depth understanding of what is happening in the systems. For instance, if the radiative properties of the participating medium are known, the effect of changes in the radiative properties on medium temperature can be predicted.

Case studies will also be conducted in this study and trends will be compared qualitatively to what is reported by researchers in the preceding sections.

Trends such as:

- Gas temperature distributions decrease more rapidly near the walls of the furnace compared to centre of the furnace (Hottel & Sarofim, 1965).
- Wall heat flux distributions are at maximum near the burners and decrease along the height of the furnace as the gas temperature decrease (Hottel & Sarofim, 1965).
- A decrease in the medium extinction coefficient results in the increase of gas temperature (Zamaniyan, et al., 2008).

From Figure 2.5 reported by Moghari et al. (2012), it is evident that the furnace absorbs the largest amount of energy compared to the other heat exchangers, thus making it one of the most important components in the high temperature systems. The celebrated example can also be applied in the present study to serve as a validation step in the model development process. The WSGG model is portrayed to be a reliable model for modelling the non-gray behaviour of gases. It will be used in this study to predict the radiative properties of the gases forming part of the participating medium found in coal-fired boiler furnaces.

3. Theoretical background

This chapter contains applicable theoretical background information required to obtain a better understanding for the present study as well as the approaches that will be followed in developing the radiation heat transfer network solution methodology.

3.1 Fundamentals of radiation heat transfer

3.1.1 Electromagnetic spectrum

Three fundamental modes of heat transfer exist and they are; conduction, convection and radiation heat transfer. Conduction from one point to another point is due to the direct exchange of kinetic energy between adjacent particles. Convection includes the effect of the bulk motion of particles wherein a fluid flowing near a hot wall is heated due to the particles adjacent to the wall and is carried away with the flow (Jones, 2000). Radiation heat transfer (also referred to as thermal radiation) on the other hand is a distinctive mode of heat transfer in that it requires no medium for energy transport. As a result it can be transmitted at a distance through transparent media and vacuum (Perry, et al., 1997). Thermal radiation is the transport of energy by electromagnetic waves, and electromagnetic waves are characterised by their wavelength or frequency, with frequency being the inverse of wavelength (Incropera, et al., 2007). Figure 3.1 shows the position of thermal radiation in the electromagnetic spectrum:

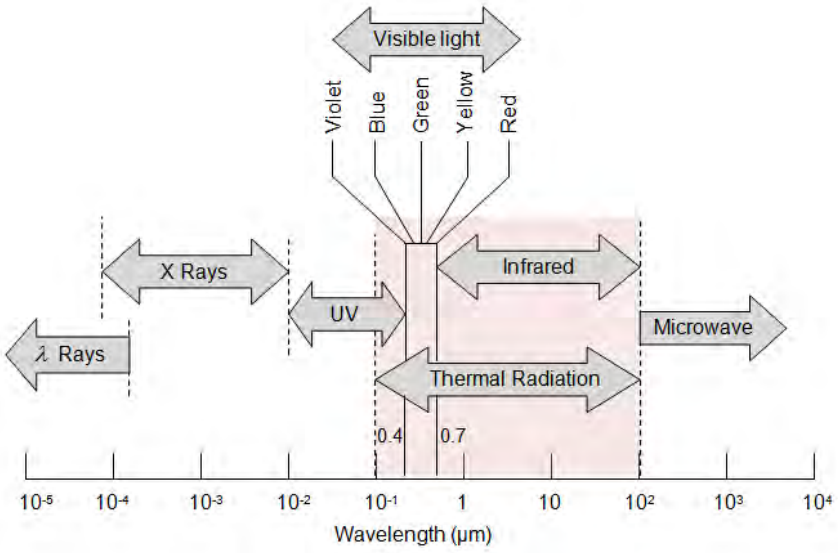

Figure 3.1. Electromagnetic spectrum (Incropera, et al., 2007).

Figure 3.1 illustrates that thermal radiation is transmitted for ranges between wavelengths of 0.1 and 100 µm, which encompasses ultraviolet, visible and infrared regions. In other words, when radiation in the wavelength range of 0.1- 100 µm is incident on a body, the radiation will heat up the body (Incropera, et al., 2007).

Radiation incident upon a body (irradiation), whether it is a gas, solid or liquid, gives rise to absorption, transmission and/or reflection (Baukal, 2000) as illustrated in Figure 3.2:

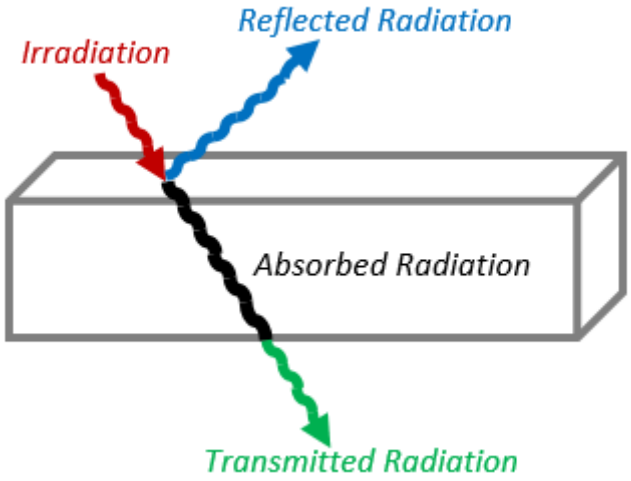

Figure 3.2. Absorbed, Reflected and Transmitted Radiation (Baukal, 2000).

Different fractions of the incident radiation are absorbed (α), reflected (ρ) and transmitted (τ) hence, $\alpha+\rho+\tau=1$. Furthermore, α is called the absorptivity, ρ the reflectivity and τ the transmissivity. The fraction of absorbed, reflected and transmitted radiation by a material is dependent on the wavelength of the incident radiation. For opaque media, $\tau=0$ since there is no transmission through an opaque medium, as a result, $\alpha+\rho=1$. Highly smooth and polished surfaces behave like mirrors to thermal radiation which results in an angle of reflection that is equal to the angle of incident radiation. This type of reflection is referred to as specular reflection. The reflectivity of rough surfaces are called diffuse since its reflection goes in all directions (Gray & Müller, 1974).

3.1.2 Net radiation heat transfer

The traditional net radiation heat transfer between a pair of blackbody surfaces is calculated as (Baukal, 2000):

$$Q_{1\Leftrightarrow 2} = \sigma A_1 F_{1\to 2}(T_1^4 - T_2^4) = \sigma A_2 F_{2\to 1}(T_1^4 - T_2^4) \tag{3.1}$$

where $Q_{1\Leftrightarrow 2}$ is the net energy transferred from surface 1 to surface 2, σ is the Boltzmann constant (= 5.67 x 10^{-8} W/m^{2}K^4) and $F_{1\to 2}$ as well as $F_{2\to 1}$ are the view factors which will be elaborated later on. A blackbody is an idealised object in that it absorbs all the radiation that is incident on it and emits the maximum amount of thermal radiation (Incropera, et al., 2007). Since surfaces in reality do not absorb all incident radiation, assumptions such as opaque, diffuse and gray surfaces are made to calculate radiation heat transfer for more realistic surfaces. Opaque signifies no transmission through the surface, diffuse means that the reflection of radiation is in all directions and gray represents a surface whose emissivity is constant with varying wavelength (Gray & Müller, 1974).

The net radiation heat transfer away from an opaque, diffuse and gray surface in an enclosure is defined as (Incropera, et al., 2007):

$$Q_i = \frac{\varepsilon_i A_i}{(1-\varepsilon_i)}(E_{bi} - J_i) \tag{3.2}$$

where ε_i, A_i, E_{bi} and J_i are the emissivity, surface area, emissive power and radiosity of the surface, respectively. The radiation heat transfer between two surfaces, i and j can also be expressed in terms of view factor as (Incropera, et al., 2007):

$$Q_i = \sum_{j=1}^{N_s} A_i F_{ij}(J_i - J_j) \tag{3.3}$$

where N_s is the total number of surfaces. Combining Equations (3.2) and (3.3) yields:

$$\frac{\varepsilon_i A_i}{(1-\varepsilon_i)}(E_{bi} - J_i) = \sum_{j=1}^{N_s} A_i F_{ij}(J_i - J_j) \tag{3.4}$$

Equation (3.4) becomes useful when surface temperatures (T_i) are known, since $E_{bi} = \sigma T_i^4$. In situations where the net radiation heat transfer is known, Equation (3.3) is preferred and can be rearranged as:

$$Q_i = \sum_{j=1}^{N_s} \frac{J_i - J_j}{(A_i F_{ij})^{-1}} \tag{3.5}$$

where $(J_i - J_j)$ is the driving potential and $(A_i F_{ij})^{-1}$ is a space geometrical resistance. The relationships given above may be represented by a radiation network (Incropera, et al., 2007).

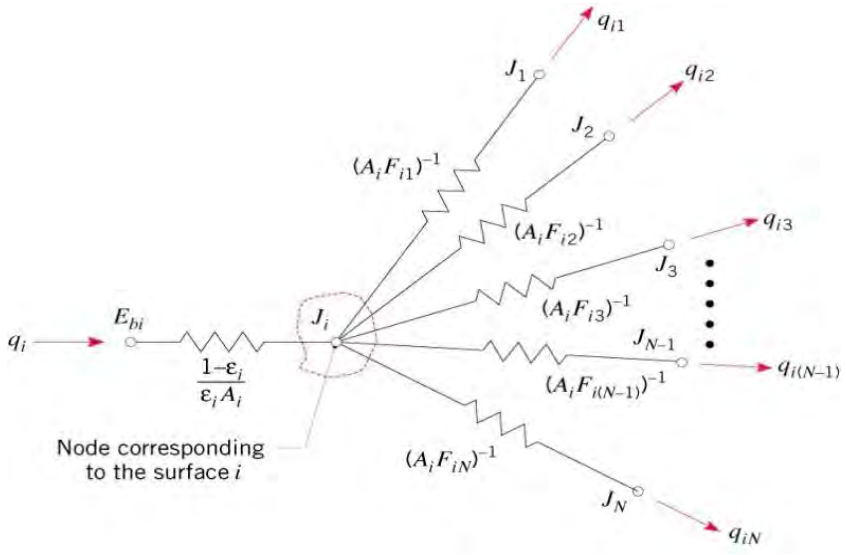

Figure 3.3. Network representation of radiation heat transfer (Incropera, et al., 2007).

Figure 3.3 is an illustration of the radiation heat transfer from one surface to all the other surfaces of an enclosure.

3.1.3 View factors

The view factor, also known as a configuration or shape factor, F_{ij} is calculated as (Incropera, et al., 2007):

$$F_{ij} = \frac{1}{A_i} \int_{A_i} \int_{A_j} \frac{\cos\theta_i \cos\theta_j}{\pi R^2} dA_j dA_i \tag{3.6}$$

The view factor, F_{ij} defines the fraction of the radiation leaving surface *i* that is intercepted by surface *j* (Incropera, et al., 2007). Equation (3.6) is developed based on Figure 3.4:

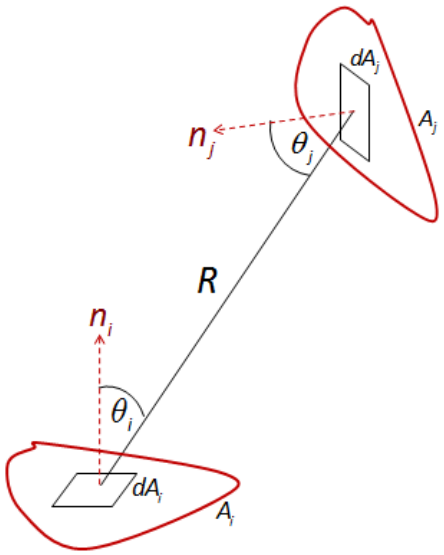

Figure 3.4. View factor between two elemental surfaces (Incropera, et al., 2007).

The view factor between two arbitrarily orientated surfaces, namely A_i and A_j is determined by considering the elemental areas on each surface, namely dA_i and dA_j. The elemental areas are connected by a line of length, R which forms polar angles, θ_i and θ_j with the surface normal vectors, n_i and n_j. The fraction of radiation leaving surface *j* that arrives at surface *i* lead to an equation identical to Equation (3.6) except that the subscripts *i* and *j* are interchanged (Incropera, et al., 2007):

$$F_{ji} = \frac{1}{A_j}\int_{A_j}\int_{A_i}\frac{\cos\theta_j \cos\theta_i}{\pi R^2} dA_i dA_j \tag{3.7}$$

Based on Equations (3.6) and (3.7), the reciprocity rule emerges (Incropera, et al., 2007):

$$A_i F_{ij} = A_j F_{ji} \tag{3.8}$$

The summation rule also holds (Incropera, et al., 2007):

$$\sum_{j=1}^{N_s} F_{ij} = 1 \tag{3.9}$$

If the two surfaces A_i and A_j are divided into N_s finite sub-surfaces, $A_i : i = 1,2,...N_s$ and $A_j : j = 1,2,...N_s$ Equation (3.6) may be approximated by:

$$F_{ij} = \frac{1}{A_i} \sum_{i=1}^{N_s} \sum_{j=1}^{N_s} \frac{\cos\theta_j \cos\theta_i \triangle A_j \triangle A_i}{\pi R^2} \tag{3.10}$$

The zonal method deals with direct exchange areas in the place of view factors. View factors are the simplest forms of direct exchange areas (DEAs) in that it does not take participating media (medium that is not transparent to radiation but rather absorbs some of the radiation passing through it) into consideration whereas DEAs does.

3.2 Zonal method theory

In the zonal method, the enclosure of interest is divided into a finite number of N_g volume/gas zones denoted by g_i and the walls of the enclosure are divided into N_s surface zones denoted by s_j (Ebrahimi, et al., 2013). Each zone is assumed to be isothermal and have uniform radiative properties. The zonal method requires first the calculation of direct exchange areas (DEAs) followed by the calculation of total exchange areas (TEAs). TEAs are functions of the DEAs in that they are determined using the matrix inversion of DEAs (Méchi, et al., 2010). DEAs measures the amount of radiation emitted by one zone that is directly intercepted by another zone, whilst taking the absorbing and scattering characteristics of the participating medium between the zones into account (Hottel & Sarofim, 1967). Hence, the computation of DEAs is dependent on the geometric orientation of zones and the radiative properties of the participating medium. The computation of TEAs on the other hand is dependent on direct exchange areas and surface emissivities. Direct and total exchange areas are independent of medium temperatures for a known extinction coefficient, as a result the exchange areas are calculated once before solving the energy balance equations on every surface and volume zone for unknown medium temperatures and surface heat fluxes.

The net radiation heat transfer rate on a surface zone and volume zone is the difference between the rate of energy lost by emission of radiation and the rate of energy absorbed by way of radiation (Ebrahimi, et al., 2004). Equations (3.11) and (3.12) show the net radiation heat transfer rate on a surface zone ($Q_{s,i}$) and volume zone ($Q_{g,i}$) in terms of direct exchange areas, respectively (Modest, 2013):

$$Q_{s,i} = \varepsilon_i \left(A_i E_{bs,i} - \sum_{j=1}^{N} \overline{s_i s_j} J_{s,j} - \sum_{k=1}^{K} \overline{s_i g_k} J_{g,k} \right) \tag{3.11}$$

$$Q_{g,i} = 4\beta_i V_i E_{bg,i} - \sum_{j=1}^{N} \overline{g_i s_j} J_{s,j} - \sum_{k=1}^{K} \overline{g_i g_k} J_{g,k} \tag{3.12}$$

where β, V, J, E_{bg}, A and ε are the extinction coefficient, volume of the zone, radiosity, gas emissive power, surface zone area and surface emissivity, respectively. Furthermore, $\overline{s_i s_j}$, $\overline{s_i g_k}$, $\overline{g_i s_j}$ and $\overline{g_i g_k}$ are the surface-to-surface, surface-to-volume, volume-to-surface and volume-to-volume direct exchange areas, respectively. The net radiation heat transfer rate on a surface zone and volume zone can also be given in terms of total exchange areas as (Modest, 2013):

$$Q_{s,i} = A_i \varepsilon_i E_{bs,i} - \sum_{j=1}^{N_s} \overline{S_i S_j} E_{bs,j} - \sum_{k=1}^{N_g} \overline{S_i G_k} E_{bg,k} \tag{3.13}$$

$$Q_{g,i} = 4\beta_i V_i E_{bg,i} - \sum_{j=1}^{N_s} \overline{G_i S_j} E_{bs,j} - \sum_{k=1}^{N_g} \overline{G_i G_k} E_{bg,k} \tag{3.14}$$

Here, $\overline{S_i S_j}$, $\overline{S_i G_k}$, $\overline{G_i S_j}$ and $\overline{G_i G_k}$ are the surface-to-surface, surface-to-volume, volume-to-surface and volume-to-volume total exchange areas, respectively, E_{bs} is the surface emissive power and E_{bg} is the medium emissive power. These equations are however mainly for an absorbing and emitting participating medium. When working with an absorbing, emitting and scattering participating medium, minor changes in the Equations are introduced.

Section 3.2.1 shows how an energy balance on a surface zone ($Q_{s,i}$) is conducted.

3.2.1 Basic zonal method energy balance

Here a basic zonal method energy balance on a surface zone is shown to indicate how the zonal method relates to the traditional net radiation heat transfer energy balance shown in Section 3.1.2. The energy balance is conducted for an enclosure with opaque, diffuse and gray surfaces enclosing a gray medium. A medium is said to be gray when its radiative properties are wavelength independent (Gray & Müller, 1974). The radiation heat transfer rate on the i^{th} surface zone is given by (Khan, et al., 1997):

$$Q_{s,i} = Q_{out,i} - Q_{in,i} = A_i(q_{out,i} - q_{in,i}) \quad i = 1,\ldots,N_s \tag{3.15}$$

where $Q_{s,i}$ is the net radiation heat transfer rate on the surface zone, $Q_{out,i}$ and $Q_{in,i}$ are the outgoing and incoming radiation heat transfer rates, respectively. The surface area is denoted by A_i ; $q_{out,i}$ and $q_{in,i}$ are the outgoing and incoming radiation heat fluxes, respectively. The total heat flux leaving the surface of interest is called the radiosity ($J_{s,i}$) and consists of the emitted as well as the reflected radiation by the surface and is given as (Khan, et al., 1997):

$$q_{out,i} = J_{s,i} = \varepsilon_i E_{bs,i} + \rho_s q_{in,i} \tag{3.16}$$

Here ε_i is the surface emissivity, $E_{bs,i}$ is the blackbody emissive power and ρ_s is the surface reflectivity. The total incoming heat flux also known as the incident heat flux is called the irradiation ($H_{s,i}$), thus:

$$q_{in,i} = H_{s,i} \tag{3.17}$$

Equation (3.16) becomes:

$$J_{s,i} = q_{out,i} = \varepsilon_i E_{bs,i} + \rho_s H_{s,i} \tag{3.18}$$

Rewriting Equation (3.15) in terms of Equations (3.16) and (3.17) yields:

$$Q_{s,i} = Q_{out,i} - Q_{in,i} = A_i(J_{s,i} - H_{s,i}) \tag{3.19}$$

An assumption which the zonal method is based on is that the enclosure surfaces are diffuse and opaque (Hottel & Cohen, 1958). Opaque implies that $\rho_s = (1 - \varepsilon_i)$. Substituting this into Equation (3.18) gives:

$$J_{s,i} = \varepsilon_i E_{bs,i} + (1 - \varepsilon_i) H_{s,i} \tag{3.20}$$

Rearranging Equation (3.20) yields:

$$H_{s,i} = \frac{J_{s,i} - \varepsilon_i E_{bs,i}}{(1 - \varepsilon_i)} \tag{3.21}$$

Substituting Equation (3.21) into Equation (3.19) and simplifying gives:

$$Q_{s,i} = \frac{\varepsilon_i A_j}{1-\varepsilon_i}(E_{bs,i} - J_{s,i}) \tag{3.22}$$

Also, substituting Equation (3.20) into Equation (3.19) and simplifying gives:

$$Q_{s,i} = \varepsilon_i A_j (E_{bs,i} - H_{s,i}) \tag{3.23}$$

Hence,

$$Q_{s,i} = \frac{\varepsilon_i A_j}{1-\varepsilon_i}(E_{bs,i} - J_{s,i}) = \varepsilon_i A_j (E_{bs,i} - H_{s,i}) \tag{3.24}$$

The rate at which radiation leaves any surface zone j and is incident on surface zone i is written in terms of DEAs as $(\overline{s_i s_j})H_{s,i}$ where $\overline{s_i s_j}$ is the surface-to-surface direct exchange area between surface j and surface i, which will be shown to be equal to $\overline{s_j s_i}$. The rate at which radiation leaves any volume zone k and is incident on surface zone i is written in terms of DEAs as $(\overline{s_i g_k})H_{s,i}$ where $\overline{s_i g_k}$ is the surface-to-volume direct exchange area between volume k and surface i, which will be shown to be equal to $\overline{g_k s_i}$ (Khan, et al., 1997). There are similar definitions for volume-to-volume DEAs as well. In Equation (3.24), the surface irradiation $(H_{s,i})$ becomes the sum of all the surface and medium radiosities and the surface area becomes the DEAs:

$$A_i H_{s,i} = \left(\sum_{j=1}^{N_s} \overline{s_i s_j} J_{s,j} + \sum_{k=1}^{N_g} \overline{s_i g_k} J_{g,k} \right) \tag{3.25}$$

Substituting Equation (3.25) into Equation (3.23) gives the radiation heat transfer rate on a surface zone (Modest, 2013):

$$Q_{s,i} = \varepsilon_i \left(A_i E_{bs,i} - \left(\sum_{j=1}^{N_s} \overline{s_i s_j} J_{s,j} + \sum_{k=1}^{N_g} \overline{s_i g_k} J_{g,k} \right) \right) \tag{3.26}$$

This shows the relation of the zonal method energy balance to the traditional net radiation heat transfer energy balance on a surface zone.

3.2.2 Direct exchange areas

When dealing with an enclosure containing a non-participating medium, the direct exchange areas are equal to the view factors multiplied by area. However, in the presence of a participating medium that emits, absorbs and scatters thermal radiation, the calculation of direct exchange areas (DEAs) becomes complex because the extinction of radiation along the path connecting two areas (surface-surface, surface-volume and volume-volume) cannot be disregarded. The calculation of direct exchange areas is the basis of the zonal method, thus making DEAs a basic ingredient of the zonal method. The majority of the computation required by the zonal method is found in the calculation of the DEAs (Lawson, 1996). They are calculated from multi-dimensional integral formulae (Hottel & Sarofim, 1967). Calculating these multi-dimensional integral formulae analytically is rarely possible, even when the extinction coefficient of the participating medium is uniform throughout the enclosure (Lawson, 1996).

Three types of direct exchange areas exist for an enclosure, namely surface-to-surface, surface-to-volume and volume-to-volume direct exchange areas and they are shown in Figure 3.5 (Martins, et al., 2012):

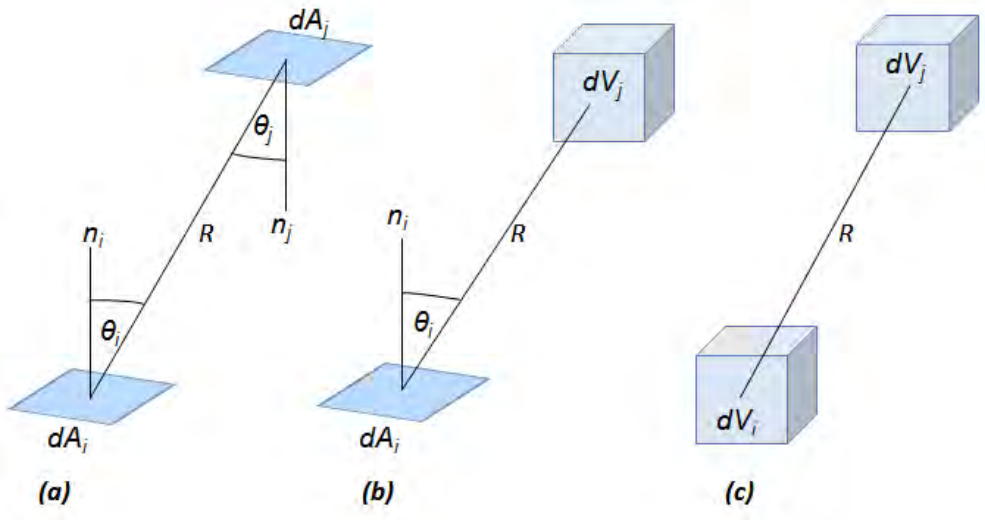

Figure 3.5. (a) Surface-to-surface, (b) Surface-to-volume & (c) Volume-to-volume DEAs (Martins, et al., 2012).

In Figure 3.5, A is the area of the surface zone and V is the volume of the volume zone. R is the line connecting two zones and θ is the angle between R and the surface normal vector denoted by n. The surface-to-surface, surface-to-volume and volume-to-volume DEAs are respectively mathematically expressed as (Ebrahimi, et al., 2013):

$$\overline{s_i s_j} = \int_{A_i}\int_{A_j} \exp(-\beta R)\frac{\cos\theta_i \cos\theta_j}{\pi R^2} dA_j dA_i \tag{3.27}$$

$$\overline{s_i g_j} = \int_{V_j}\int_{A_i} \exp(-\beta R)\frac{\beta\cos\theta_i}{\pi R^2} dA_i dV_j \tag{3.28}$$

$$\overline{g_i g_j} = \int_{V_i}\int_{V_j} \exp(-\beta R)\frac{\beta^2}{\pi R^2} dV_j dV_i \tag{3.29}$$

Here, β is the extinction coefficient of the participating medium. The extinction coefficient represents the combined effect of the absorption and scattering coefficients of the medium (Siegel & Howell, 1972). Hence, it is a measure of how the intensity of a beam of radiation passing through a medium changes with distance (Siegel & Howell, 1972). The term, "$\exp(-\beta R)$" forming part of Equations (3.27), (3.28) and (3.29) is the transmittance which gives the fraction of energy that passes through two points in a medium along a straight line of length *R* (Hottel & Sarofim, 1967). These direct exchange areas must satisfy reciprocity relations and therefore (Hottel & Sarofim, 1967):

$$\overline{s_i s_j} = \overline{s_j s_i} \qquad \overline{g_i s_j} = \overline{s_j g_i} \qquad \overline{g_i g_j} = \overline{g_j g_i} \tag{3.30}$$

Equations (3.31) and (3.32) show relationships representing the energy conservation principles that must also be satisfied by the DEAs (Hottel & Sarofim, 1967):

$$\sum_{j=1}^{N_s} \overline{s_i s_j} + \sum_{k=1}^{N_g} \overline{s_i g_k} = A_i \tag{3.31}$$

$$\sum_{j=1}^{N_s} \overline{g_i s_j} + \sum_{k=1}^{N_g} \overline{g_i g_k} = 4\beta_i V_i \tag{3.32}$$

For $i = 1,\ldots,N_s$ in Equation (3.31) and $i = 1,\ldots,N_g$ in Equation (3.32) where N_s and N_g are the number of surface and volume zones, respectively.

3.2.3 Smoothing of direct exchange areas

The calculation of direct exchange areas (DEAs) involves a large set of double area/area, area/volume and volume/volume integrals. These multi-dimensional integrals indicate that numerical evaluation is essential.

Achieving high accuracy in performing the multiple integrals is challenging and numerical techniques for evaluating the DEAs results in inherent numerical errors (Méchi, et al., 2010). As a result, DEAs are expected to include random inaccuracies merely because the calculated DEAs are approximations to the correct value and may not satisfy conservation and reciprocity conditions (Tian & Chiu, 2003). If the DEAs do not satisfy the conservation principles then the sum of the surface heat fluxes will be non-zero.

The process of taking a set of approximated DEAs and transforming them to satisfy the conservation and reciprocity conditions is called smoothing (Lawson, 1995). Since the conservation principles ((3.31) and (3.32)) hold for the condition of zero numerical errors in the evaluation of such exchange areas, smoothing methods are very essential to satisfy the conservation principles.

Smoothing by Larsen and Howell (1986)

Larsen and Howell (1986) proposed a smoothing technique for direct exchange areas that makes it possible for all required relationships to be satisfied. This technique is referred to as the least-squares smoothing using Lagrange multipliers technique. This is essentially a constrained optimisation problem that optimises the objective function with respect to the direct exchange areas in the presence of energy conservation constraints.

Here, the initial set of direct exchange areas are assembled to form one matrix as shown below (Larsen & Howell, 1986):

$$[X]=\begin{bmatrix} [\overline{ss}] & [\overline{sg}] \\ [\overline{sg}]^T & [\overline{gg}] \end{bmatrix} \tag{3.33}$$

The energy conservation principles in Equations (3.31) and (3.32) require that (Larsen & Howell, 1986):

$$\sum_{j=1}^{N} x_{ij} = c_i \text{ where}$$
$$c_i = A_i \quad \text{for } i \le N_s$$
$$c_i = 4\beta V_i \quad \text{for } i > N_s \tag{3.34}$$

The idea is to adjust $[X]$ to meet the reciprocity relationships and energy conservation principles while minimising the disturbance to the originally calculated direct exchange area (DEA) values. Hence, an objective function (*H*) is defined as (Larsen & Howell, 1986):

$$H = \sum_{i=1}^{N} \sum_{j=1}^{N} \frac{1}{2w_{ij}} \cdot \left(x'_{ij} - x_{ij} \right)^2 \tag{3.35}$$

where *N* is the total number of surface and volume zones, w_{ij} are arbitrary weighting factors, x'_{ij} are the adjusted DEA values and x_{ij} are the original DEA values. When using weighting factors of equal size ($w_{ij} = 1$), the direct exchange areas are adjusted equally and the zero valued exchange areas ($s_i s_i = x_{ii} = 0$) are disturbed, resulting in negative areas. Using weighting factors that are equal to the square of the originally calculated DEAs ($w_{ij} = x_{ij}^2$) results in new direct exchange area values that are adjusted in proportion to its original size (Larsen & Howell, 1986).

Due to the fact that Lagrange multipliers are used, the Lagrangian is set as:

$$L = H + \sum_{i=1}^{N} \lambda_i \left(g_i - g_i^* \right) \tag{3.36}$$

where λ_i are the Lagrange multipliers, g_i are the row-sum constraints and g_i^* are the column-sum constraints (Larsen & Howell, 1986). These constraints are defined as (Larsen & Howell, 1986):

$$g_i = c_i - \sum_{j=1}^{N} x'_{ij} \qquad for \quad i = 1,2,\ldots,N \tag{3.37}$$

and

$$g_i^* = c_i - \sum_{j=1}^{N} x'_{ji} \qquad for \quad i = 1,2,\ldots,N \tag{3.38}$$

Substituting Equations (3.37) and (3.38) into Equation (3.36) gives:

$$\begin{aligned} L &= H + \sum_{i=1}^{N} \lambda_i \left(g_i - g_i^* \right) \\ &= \sum_{i=1}^{N} \sum_{j=1}^{N} \frac{1}{2w_{ij}} \cdot \left(x_{ij}^{'} - x_{ij} \right)^2 + \sum_{i=1}^{N} \lambda_i \left[\left(c_i - \sum_{j=1}^{N} x_{ij}^{'} \right) + \left(c_i - \sum_{j=1}^{N} x_{ji}^{'} \right) \right] \end{aligned} \tag{3.39}$$

Partially differentiating L in Equation (3.39) with respect to $x_{ij}^{'}$ and equating to zero yields:

$$\frac{\partial L}{\partial x_{ij}^{'}} = 0 = \frac{1}{w_{ij}} (x_{ij}^{'} - x_{ij}) + \left(-\lambda_i - \lambda_j \right) \tag{3.40}$$

The adjusted direct exchange area values are obtained from rearranging Equation (3.40) as (Larsen & Howell, 1986):

$$x_{ij}^{'} = x_{ij} + w_{ij} \cdot \left(\lambda_i + \lambda_j \right) \tag{3.41}$$

The adjusted direct exchange area values must satisfy reciprocity and conservation principles thus:

$$c_i - \sum_{j=1}^{N} x_{ij} = \lambda_i \sum_{j=1}^{N} w_{ij} + \sum_{j=1}^{N} w_{ij} \lambda_j \tag{3.42}$$

Writing Equation (3.42) for every direct exchange area value results in a set of equations simplified as (Larsen & Howell, 1986):

$$[R]\lambda = \delta \tag{3.43}$$

where

$$\begin{aligned} r_{ij} &= w_{ij} \qquad for \quad i \neq j \\ r_{ii} &= w_{ii} + \sum_{j=1}^{N} w_{ij} \\ \delta_i &= c_i - \sum_{j=1}^{N} x_{ij} \end{aligned} \tag{3.44}$$

Subsequently, Lagrange multipliers are solved using Equation (3.43).

Smoothing by Lawson (1995)

Lawson (1995) proposed a smoothing technique referred to as the generalised Lawson smoothing technique, for the DEAs. Here, each direct exchange area value is adjusted according to its size and it ensures that no adjusted direct exchange area value is negative. Furthermore, the error in the conservation condition is firstly calculated for a surface by taking the difference between the area of the surface and the sum of all the DEAs from the same surface ($\delta_i = A_i - \sum \overline{s_i s_j}$). Following this, the direct exchange area value is adjusted by adding the error difference relative to the sum of all the DEAs to the original direct exchange area value, resulting in a smoothing equation (Lawson, 1995):

$$\overline{s_i s_j}' = \overline{s_i s_j} + \frac{\overline{s_i s_j}}{\sum \overline{s_i s_j}} \cdot \delta_i \tag{3.45}$$

Simplifying Equation (3.45) yields (Lawson, 1995):

$$\overline{s_i s_j}' = \overline{s_i s_j} \left(\frac{A_i}{\sum \overline{s_i s_j}} \right) \tag{3.46}$$

Lawson (1995) has proposed this method for a set of surface-to-surface direct exchange areas in a transparent medium.

Extension of Lawson's (1995) smoothing technique

Méchi et al. (2010) extended Lawson's technique to an absorbing semi-transparent medium. For semi-transparent media, the surface-to-gas and the gas-to-gas DEAs are non-zero. Analogous expressions for smoothed surface-to-surface, surface-to-volume and volume-to-volume DEAs, respectively are (Méchi, et al., 2010):

$$\overline{s_i s_j}' = \overline{s_i s_j} \cdot \left(\frac{A_i}{\sum_{j=1}^{N_s} \overline{s_i s_j} + \sum_{k=1}^{N_g} \overline{s_i g_k}} \right) \tag{3.47}$$

$$\overline{s_i g_j}' = \overline{s_i g_j} \cdot \left(\frac{A_j}{\sum_{j=1}^{N_s} \overline{s_i s_j} + \sum_{k=1}^{N_g} \overline{s_i g_k}} \right) \tag{3.48}$$

$$\overline{g_i g_j}' = \overline{g_i g_j} \cdot \left(\frac{4\beta_j V_j}{\sum_{j=1}^{N_s} \overline{g_i s_j} + \sum_{k=1}^{N_g} \overline{g_i g_k}} \right) \tag{3.49}$$

3.2.4 Numerically evaluated direct exchange areas

Hottel and Sarofim (1967) prepared graphs and tables providing values for direct exchange areas between pairs of surface zones, volume zones and surface-to-volume zones that can be obtained from known enclosure dimensions and the radiative properties of the participating medium. The tables however only cater for cylindrical enclosures. Therefore, Hottel and Sarofim (1967) numerically evaluated the direct exchange area integrals and derived equations for the different DEAs applicable to cubic and rectangular enclosures. Figure 3.6 shows the geometry of direct exchange areas between parallel and perpendicular squares for enclosures (Hottel & Cohen, 1958):

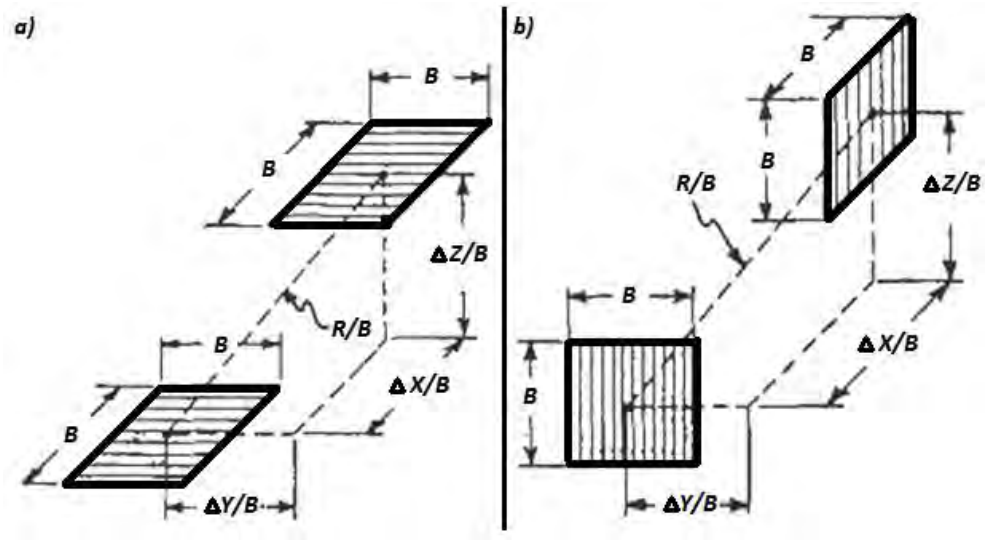

Figure 3.6. Geometry of direct exchange areas between parallel and perpendicular squares (Hottel & Cohen, 1958).

Figure 3.6a shows the geometry of direct exchange areas between parallel (Bottom $\Leftrightarrow$ Top) squares and Figure 3.6b shows the geometry of direct exchange areas between perpendicular (Front $\Leftrightarrow$ Right) squares for enclosures.

Equation (3.50) shows only the Bottom $\Leftrightarrow$ Top direct exchange area equation by Hottel and Sarofim (1967), while the comprehensive set is provided in Appendix C.1:

$$\overline{s_j s_i}(\|) = B^2 \cdot \frac{\exp(-\beta R)\cdot\left(\frac{\triangle z}{B}\right)^2}{\pi\cdot\left(\frac{R}{B}\right)^4} \qquad \text{Bottom} \Leftrightarrow \text{Top} \tag{3.50}$$

B is the side length of the surface zone, *R* is the line connecting the two surface zones and $\triangle z$ is the difference between the z-coordinates of the surface centres, as indicated in Figure 3.7:

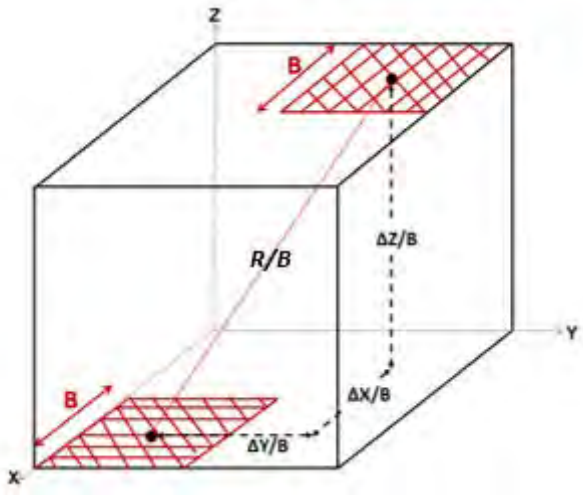

Figure 3.7. Surface-to-surface direct exchange area equation illustration.

Tucker (1986) numerically integrated, correlated, graphed and suggested exponential expressions for the direct exchange areas of cubic and rectangular enclosures which covers a range of optical thicknesses (βB) from 0 to 18 (Tucker, 1986). Among others, the exponential expressions for the direct exchange area between a pair of parallel surface zones is given by (Tucker, 1986):

$$\frac{\overline{s_j s_i}}{B^2}(\|) = C\cdot\exp(-A\cdot\beta B) \tag{3.51}$$

In Equation (3.51), *B* is the side length of the surface zone as indicated in Figure 3.7 above; *A* and *C* are correlation coefficients (some coefficients are provided in Appendix C.3) and β is the extinction coefficient of the medium.

3.3 Participating media

When an enclosure contains a gaseous medium such as air, which is basically transparent to radiation, the medium contained inside the enclosure is referred to as a non-participating medium (Baukal, 2000). The same holds for a space that is maintained under vacuum. This indicates that the medium does not emit, absorb or scatter any of the radiation passing through it. A participating medium is said to be present when an enclosure contains an emitting, absorbing and/or scattering medium. An example of a participating medium is CO_2, which emits and absorbs part of the radiation passing through it (Baukal, 2000).

The combustion flame in a coal-fired boiler furnace is a two-phase mixture of dispersed particles and gaseous products of combustion which play a major role in radiation heat transfer (Crnomarkovic, et al., 2012). Radiation incident on a suspension of particles in a gas is partly absorbed and scattered. The radiation travelling along a path is extinguished by absorption, while scattering enhances radiation through emission into other directions. The absorbing and scattering influence of the participating medium is obtained from the radiative properties of the medium and is collectively called the extinction influence of the participating medium (Gray & Müller, 1974).

3.4 Radiative properties of coal combustion particles

Coal, char, fly-ash and soot are the dispersed particles that form part of the participating medium in coal-fired boiler furnaces. They emit, absorb and/or scatter radiation continuously throughout the electromagnetic spectrum (Lou, et al., 2007). As a result, their radiative properties are usually considered gray in the calculation of radiation heat transfer. 'Gray' signifies that the radiative properties of the medium are independent of wavelength (Crnomarkovic, et al., 2012). In terms of the location of the particles inside the furnace; coal particles mostly exist in the vicinity of the burners and char particles are found in the combustion zone (Crnomarkovic, et al., 2012). According to Marakis et al. (2000), coal and char strongly extinguish thermal radiation. Crnomarkovic et al. (2012) stated that the soot particles present in the coal flame are in negligible amounts.

Various studies, including Gupta et al. (1983), Boothroyd & Jones (1986) as well as Crnomarkovic et al. (2012) indicate that fly-ash particles however, not only cover the whole furnace volume but also have the strongest influence on the radiative properties of the coal combustion flame (Crnomarkovic, et al., 2012).

According to references cited in Viskanta et al. (1987), the influence of fly-ash particles to radiation substantially exceeds the contribution of char and soot as well as that of the combustion gases. Char particles essentially contributes to radiation heat transfer over the length of the coal combustion flame. At the walls of the furnace, the char particles concentration is so small that it exerts insignificant influence on the radiative heat flux (Viskanta & Mengüc, 1987). Figure 3.8 shows the contributions of coal, fly-ash, soot and combustion gases (mainly CO_2 and H_2O vapour) on the radiative heat flux along the height of the furnace (Viskanta & Mengüc, 1987):

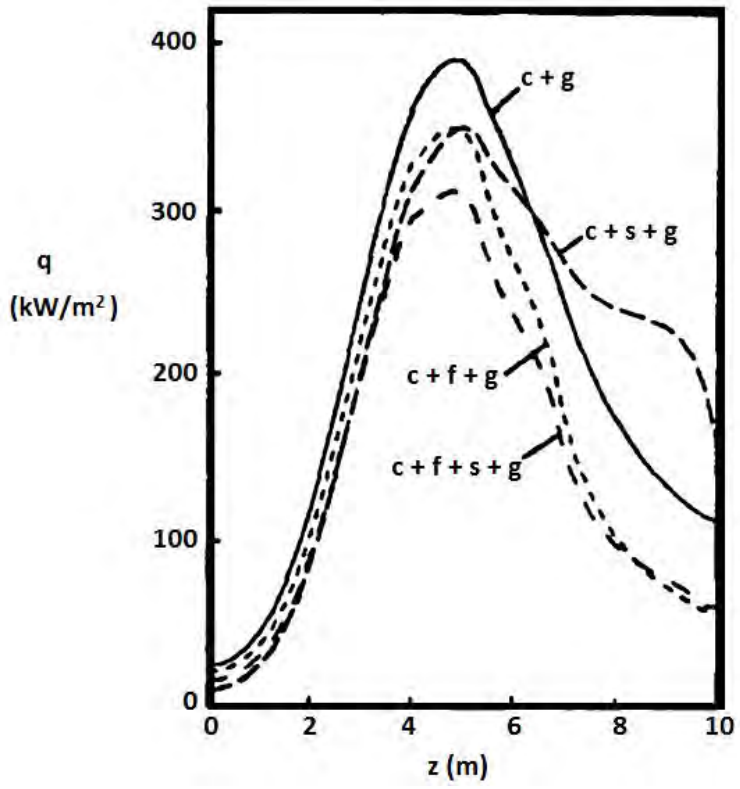

Figure 3.8. Radiative heat flux distribution along the wall of a pulverised coal-fired furnace; (c = coal, f = fly-ash, s = soot & g = combustion gases) (Viskanta & Mengüc, 1987).

Looking at Figure 3.8, in terms of location in the furnace; up to about 3 m from the bottom of the furnace, the distinction between the curves accounting for different combinations of components (coal, fly-ash, soot and gases) is not significant. However, beyond 3 m there are clear differences and it is also normally the area where the burners are located and the highest temperatures are observed. At this point combustion is also the most intense, hence the components behaves differently.

What can be seen in Figure 3.8 is that neglecting the contribution of the fly-ash $(c+g+s)$ versus $(c+f+g)$ yields a noteworthy change in the radiative heat flux. The primary reason for this difference is that the significant scattering by the fly-ash particles is neglected.

Neglecting the soot $(c+f+g)$ versus $(c+f+g+s)$ increases the radiative heat flux since the significant absorption of the soot is neglected (Viskanta & Mengüc, 1987). From Figure 3.8, it can also be seen that regardless of the insignificance of soot according to Crnomarkovic et al. (2012), its role in radiation heat transfer cannot be disregarded.

In order to predict the radiative properties, that is, the absorption and scattering coefficients of participating particles, the particles are approximated as spheres (Viskanta & Mengüc, 1987). Depending on the particle size, specific theories are applied. The most widely used theory to predict the radiative properties of coal combustion particles is the Mie theory. Using this theory, the absorption efficiency factors Q_{abs} and scattering efficiency factors Q_{sca} of the particles can be evaluated. These efficiency factors represent the ratio of energy absorbed and scattered by the particle to the total energy that is incident on the particle (Farias & Carvalho, 1998).

In order to evaluate the efficiency factors, information of the optical properties of the particles are important. Optical properties are characterised in terms of size parameter, $\left(x=\pi D/\lambda\right)$ and complex index of refraction, $\left(m=n-ik\right)$ (Kim & Lior, 1995). *D* in the size parameter (*x*) is the particle diameter. The optical constants, *n* and *k* in the complex index of refraction are called the absorptive and refractive index of refraction, respectively. The complex index of refraction for soot, different types of coal, fly-ash and char are tabulated in Table 3.1 (Modest, 2013):

Table 3.1. Representative values for refractive indexes.

Particle Type	**Complex index of refraction** $\left(m=n-ik\right)$
Carbon & Soot	$m=2.20-1.12i$ (Modest, 2003)
Anthracite	$m=2.05-0.54i$ (Modest, 2003)
Bituminous	$m=1.85-0.22i$ (Modest, 2003)
Lignite	$m=1.70-0.07i$ (Modest, 2003)
Fly-ash	$m=1.50-0.02i$ (Modest, 2003)

Char	$m = 1.93 - 1.02i$ (Smoot & Pratt, 1979)

The complex index of refraction is an indication of the amount of scattering and absorption of an electromagnetic wave by a particle with a given wavelength (Modest, 2013).
According to Smoot and Pratt (1979), although the values for the complex index of refraction are calculated at specific wavelengths, they can be used throughout the combustion process because as the particle size increases, the optical behaviour of particles loses its wavelength dependence.

Efficiency factors together with the volume fraction and/or number density of the particles are variables in the absorption coefficient and scattering coefficient equations. The absorption and scattering coefficients of fly-ash, char and coal are then calculated from (Smoot & Pratt, 1979):

$$\kappa_p = N_p Q_{abs} \frac{\pi D^2}{4} = \frac{3}{2} \frac{Q_{abs} f_v}{D}, m^{-1} \tag{3.52}$$

and

$$\sigma_s = N_p Q_{sca} \frac{\pi D^2}{4} = \frac{3}{2} \frac{Q_{sca} f_v}{D}, m^{-1} \tag{3.53}$$

where N_p is the particle number density and $\pi D^2/4$ is the projected particle area. Q_{abs} and Q_{sca} are the absorption and scattering efficiency factors, respectively, f_v is the particle volume fraction and D is the particle diameter. The volume fraction is obtained from dividing the particle concentration by the particle density (Trivic, 2014). Equations (3.52) and (3.53) are however only valid when the particle size distribution is monodisperse, that is when the particle size is uniform (Smoot & Pratt, 1979). The pulverised coal flame on the contrary consists of particles with a wide range of sizes, for such a polydisperse nature of particles, the particle number density (N_p) is represented by a particle size distribution gamma function as (Modest, 2013):

$$N_p = \int_0^\infty n(r) dr = \int_0^\infty a r^\alpha e^{-br} dr = \frac{a\Gamma(\alpha+1)}{b^{(\alpha+1)}} \tag{3.54}$$

where a, α and b are constants, r is the varying particle radius and Γ is the gamma function defined as (Modest, 2013):

$$\Gamma(z) = (z-1)! \tag{3.55}$$

If there is no particle size distribution function defined, the absorption and scattering coefficients can be found by numerical summation over different sizes as (Smoot & Pratt, 1979):

$$\kappa_p = \sum_i N_{p,i} Q_{abs,i} \frac{\pi D_i^2}{4}, m^{-1} \tag{3.56}$$

and

$$\sigma_s = \sum_i N_{p,i} Q_{sca,i} \frac{\pi D_i^2}{4}, m^{-1} \tag{3.57}$$

Here, the subscript i represents the different particle sizes that are considered for the calculations. A scattering coefficient is not calculated for soot since it scatters in negligible amounts (Smoot & Pratt, 1979). The absorption coefficient of soot is traditionally calculated from (Modest, 2013):

$$\kappa_s = \frac{3.72 f_v C_0 T_g}{C_2}, m^{-1} \tag{3.58}$$

This equation is derived from the mean-Planck and mean-Rosseland functions combined (Modest, 2013).

Here $C_0 = \frac{36\pi nk}{(n^2-k^2+2)^2+4n^2k^2}$ and $C_2 = 1.4388 \times 10^{-2}\ m\ K$.

Furthermore, f_v is the soot volume fraction which ranges between 10^{-8} and 10^{-6} (Crnomarkovic & Sijercic, 2008). T_g is the temperature of the soot particles which is equated to the gas temperature; n and k is the absorptive and refractive index of refraction of the complex index of refraction, respectively.

3.4.1 Efficiency factor approximations

The approximation of efficiency factors (Q_{abs} and Q_{sca}) based on the Mie theory is known to be a time consuming and complex process (Kim & Lior, 1995). As a result, simplified approximations have been derived for limiting cases of complex index of refractions and size parameters which are suitable for pulverised coal combustion furnaces that are comparable to the Mie theory (Kim & Lior,

1995). The efficiency factor approximations for coal, char and fly-ash are as follows (Kim & Lior, 1995):

Coal and char efficiency factors

Pulverised coal typically has an average diameter that is in the order of 100 μm (Kim & Lior, 1995). Char has an average diameter of the same magnitude for wavelengths of 1 μm to 10 μm. As a result, the size parameter is as large as 10π – 100π. The complex index of refraction of char particles ranges between 1.6 and 3.6 at a wavelength of 2 μm. For these values of size parameter and complex index of refraction, the geometrical limit which is an asymptotic approach to the efficiency factors is used (Kim & Lior, 1995). Here, the extinction and scattering efficiency factors for coal and char are given, as (Kim & Lior, 1995):

$$Q_{ext} = 2 \tag{3.59}$$

and

$$Q_{sca} = \frac{1}{2}(f_1 + f_2) \tag{3.60}$$

where

$$f_i = \frac{8}{q_i^2}\left[q_i - \ln(1 + q_i + \frac{1}{2}q_i^2)\right] \qquad i = 1,2 \tag{3.61}$$

with

$$q_1 = (nk)^{-1/2} \text{ and } q_2 = 2/q_1 \tag{3.62}$$

Here n and k are the real and imaginary parts of the complex index of refraction.

The complex index of refraction for char is $m = 1.93 - 1.02i$ at a wavelength of 2 μm (Smoot & Pratt, 1979). The complex indexes of refraction for the different types of coal are tabulated in Table 3.1. The absorption efficiency factor is then calculated from (Smoot & Pratt, 1979):

$$Q_{abs} = Q_{ext} - Q_{sca} \tag{3.63}$$

Fly-ash efficiency factors

Each char particle breaks up into typically five ash particles that is about 10-30 µm in diameter (Kim & Lior, 1995). The typical size parameter of fly-ash is in the order of 10 at a wavelength of 2 µm. The real part of the complex index of refraction of fly-ash (*n*) is less than 2 and the imaginary part (*k*) is close to zero (Van de Hulst, 1957). The complex index of refraction for fly-ash is $m = 1.50 - 0.02i$ (Modest, 2003) and its absorption efficiency factor is approximated from (Kim & Lior, 1995):

$$Q_{abs} = 1 + \frac{e^{-4xk}}{2xk} + \frac{e^{-4xk} - 1}{8x^2k^2} \tag{3.64}$$

where *n* is the real part of the complex index of refraction and *x* is the fly-ash size parameter.

The scattering efficiency factor is then calculated from the difference between the extinction and scattering efficiency factors. The extinction efficiency factor is calculated from (Kim & Lior, 1995):

$$Q_{ext} = 2 - 4\left(\frac{\cos\phi}{\rho}\right)\sin(\rho - \phi)e^{-\rho\cdot\tan\phi} - 4\left(\frac{\cos\phi}{\rho}\right)^2\cos(\rho - 2\phi)e^{-\rho\cdot\tan\phi} + 4\left(\frac{\cos\phi}{\rho}\right)^2\cos(2\phi) \tag{3.65}$$

where $\rho = 2x(n-1)$ and $\phi = \tan^{-1}\left(\frac{k}{n-1}\right)$

As a result, the scattering efficiency factor is then calculated from:

$$Q_{sca} = Q_{ext} - Q_{abs} \tag{3.66}$$

Figure 3.9 and Figure 3.10 shows the extinction and scattering efficiency factors of fly-ash particles. In both figures, the efficiency factors are computed using the anomalous limit (A), dielectric limit (D), geometrical limit (G), and Mie theory (E) approximations. Here, the anomalous limit and the dielectric limit have an oscillating pattern which is similar to the Mie theory (Kim & Lior, 1995).

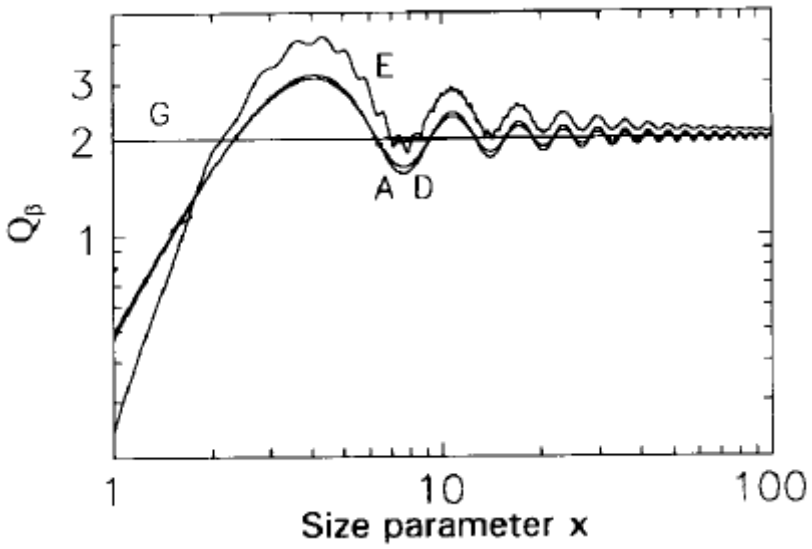

Figure 3.9. Extinction efficiency factors of fly-ash as a function of size parameter (Kim & Lior, 1995).

From Figure 3.9, it is evident that the fly-ash extinction efficiency factor approximations from the anomalous limit and the dielectric limit correspond better to the Mie theory and the geometrical limit is not preferred. The same is observed for the fly-ash scattering efficiency factor in Figure 3.10:

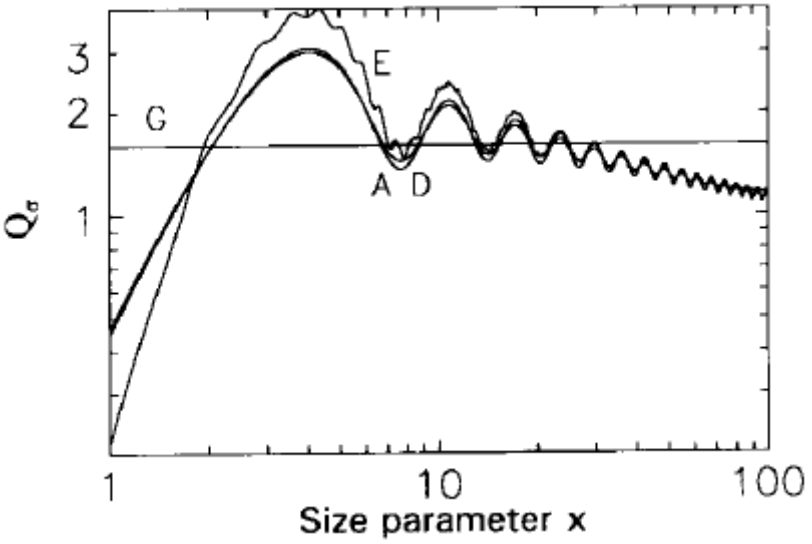

Figure 3.10. Scattering efficiency factors of fly-ash as a function of size parameter (Kim & Lior, 1995).

The deviation in the scattering efficiency factor from the Mie theory is 1.0% for the anomalous limit and 4.8% for the dielectric limit. In the present study, the anomalous limit was used (Kim & Lior, 1995).

3.5 Radiative properties of combustion gases

It is mainly the radiative properties of CO_2 and H_2O that are considered in the evaluation of radiation heat transfer of coal-fired boiler furnace (Smith, et al., 1982). Gases such as NO, SO_2 and CO which also form part of the gaseous mixture are not considered because their total contribution to flame emission in large furnaces is relatively small (Holkar & Hebbal, 2013). These gases emit and absorb radiation in discrete bands of the electromagnetic spectrum (Lou, et al., 2007). Radiation outside these bands is not affected by the presence of the gases, thus making the gases essentially transparent to radiation. Furthermore, gases do not scatter radiation significantly; as a result, their scattering contribution is neglected in radiation heat transfer calculations (Crnomarkovic, et al., 2013). The wavelength dependence of these gases makes them non-gray gases. Figure 3.11 summarises the concept of radiation behaviour of non-gray gases and surface characteristics (Khan, et al., 1997):

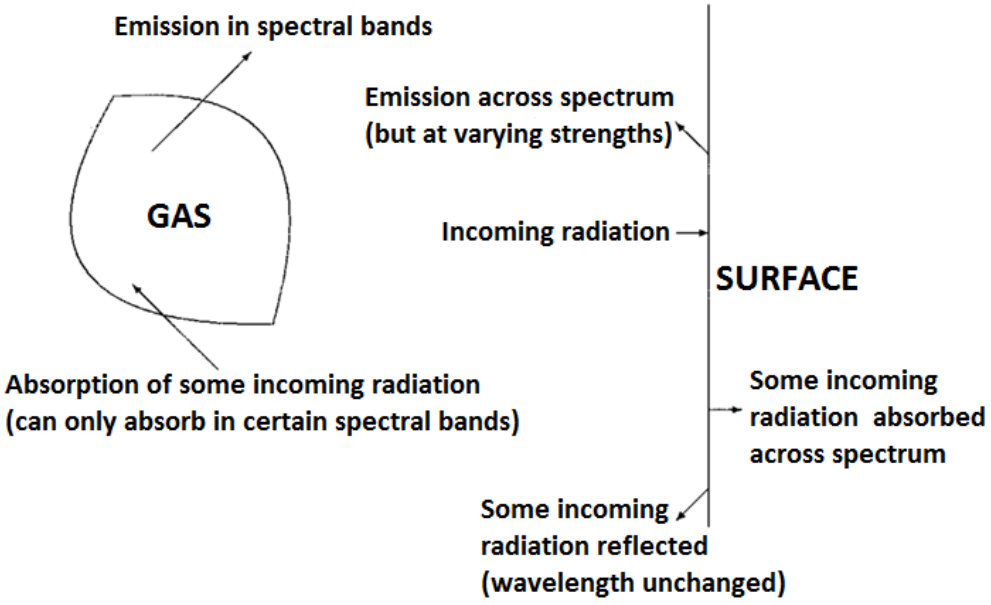

Figure 3.11. Behaviour of non-gray gas and surface characteristics (Khan, et al., 1997).

Models used to determine the radiative properties of gases are categorised as band models, line-by-line models and global models. Using band models, the radiative properties of the gases are determined from the electromagnetic spectrum by dividing the entire electromagnetic spectrum into several bands. The accuracy of the properties increases as the width of the bands become narrower (Viskanta & Mengüc, 1987). An example of a band model is the exponential wide band model (EWBM), developed by Edwards (1976).

Line-by-line models result in more accurate spectral radiative properties and are expensive from a computational effort point of view while global models show less accuracy, but produce acceptable results with less computational load (Yoon, et al., 2010). Among the global models is the weighted sum of gray gases (WSGG) model which was introduced by Hottel & Sarofim (1967). The radiative properties of a gas mixture using the WSGG model is represented by a single parameter named the effective absorption coefficient (Liu, et al., 1998). Another example of a global model is the simple gray gas (SGG) model which is the simplest model that is applied to calculate the radiative properties of the gaseous combustion products. This model assumes that the radiation absorption and emission by gases are independent of the wavelength of the radiation (Liu, et al., 1998).

3.5.1 Weighted sum of gray gasses model

The weighted sum of gray gases (WSGG) model is used to model the radiative properties of non-gray gases. In this model, the non-gray gas is replaced with a finite number of gray gases (traditionally three gases and one transparent gas) (Hottel & Sarofim, 1967). Total gas emissivities are represented in this model as (Hottel & Sarofim, 1967):

$$\varepsilon_g = \sum_{i}^{N_{gg}} a_i(T_g)\left[1-\exp(-\kappa_i p L_m)\right] \tag{3.67}$$

where a_i is the gas temperature dependent weighting factor of the i^{th} gray gas. This weighting factor is physically interpreted as "the fractional amount of black body energy in the spectral region where a gray gas having an absorption coefficient exists" (Boutoub, et al., 2006). The temperature independent absorption coefficients of each gray gas and the partial pressure of the mixture are denoted by κ_i and p, respectively. L_m is the characteristic dimension of the system, also referred to as the mean beam length or path length. For multiple geometries (cubical and rectangular enclosures), the mean beam length is approximated as (Jones, 2000):

$$L_m = 3.6\frac{V}{A} \tag{3.68}$$

Here, V is the volume of the enclosure and A is the total bounding surface area. The mean beam lengths for different geometries are shown in Table 3.2 (Jones, 2000):

Table 3.2. Mean beam lengths for gas radiation in a number of geometries (Jones, 2000).

Geometry	**Mean beam length,** $L_m = 3.6\frac{V}{A}$
Cube side length, B radiating to one surface	$L_m = 3.6\frac{B^3}{B^2} = 3.6B$
Cube side length, B radiating to all surface	$L_m = 3.6\frac{B^3}{6B^2} = 0.6B$
Rectangle radiating to all surface	$L_m = 3.6\frac{l \times b \times h}{2(l \times b) + 2(b \times h) + 2(l \times h)}$

According to Liu et al. (1998), the use of two or three gray gas components and a transparent gas is adequate to accurately evaluate the total emissivity of a H_2O vapour/ CO_2/ transparent gas mixture for a wide range of temperatures, partial pressures and path lengths. Smith et al. (1982) reported weighting factors for the WSGG model that are based on total gas emissivities for CO_2, H_2O vapour and mixtures thereof. These weighting factors are applicable to surface and gas temperatures that vary between 600 K and 2400 K, a total pressure of 1 atm and mean beam lengths of 0.001 m to 10 m. The weighting factors are calculated from (Smith, et al., 1982):

$$a_i = \sum_{j=1}^{J=3} b_{i,j} T_g^{j-1} \tag{3.69}$$

where, T_g is the gas temperature and $b_{i,j}$ are coefficients tabulated in Table 3.3:

Table 3.3. Weighting factor coefficients by Smith et al. (1982).

i	κ_i	$b_{i,1} \times 10^1$	$b_{i,2} \times 10^4$	$b_{i,3} \times 10^7$	$b_{i,4} \times 10^{11}$
1	0.4201	6.508	-5.551	3.029	-5.353
2	6.516	-0.2504	6.112	-3.882	6.528
3	131.9	2.718	-3.118	1.221	1.612

For the transparent gas, the weighting factor is calculated as (Smith, et al., 1982):

$$a_0 = 1 - \sum_{i=1}^{I=3} a_i \tag{3.70}$$

4. Model development

The primary objective of this study is to develop and implement a radiation heat transfer network solution methodology based on the zonal method that may be applied in boiler furnace modelling. The knowledge gained from the preceding chapters will be applied in this chapter to address the primary objective of this study. The specific objectives that are formulated in order to meet the primary objective will form part of the steps taken towards developing the network model. The model to be developed in this chapter can be solved for two different cases defined as a primary case and a secondary case. The primary case is based on the assumption that the radiative properties, that is, the absorption and scattering coefficients of the participating medium are readily available. This means that the absorption and scattering coefficients of the medium are fixed inputs to the network model. The secondary case on the other hand uses simplified approximations of the Mie theory and the weighted sum of gray gases (WSGG) model to estimate the radiative properties of the participating medium in a coal-fired boiler furnace based on other inputs that will be presented later on. The software package that is identified as the platform for developing the radiation heat transfer network is Scilab. The methodology of the network model development is summarised in Figure 4.1:

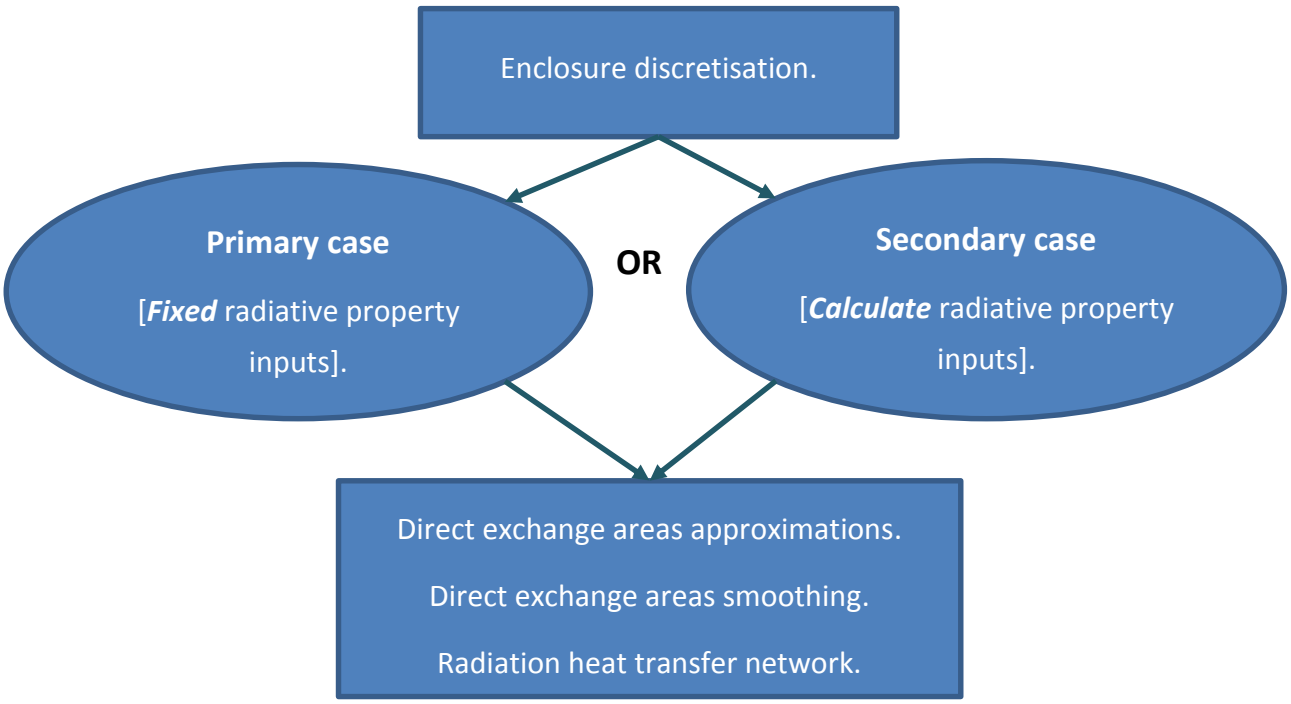

Figure 4.1. Model development methodology.

Figure 4.1 shows that the radiation heat transfer network can be solved for either the primary case or the secondary case. The two cases will be discussed in Sections 4.2 and 4.3 after discussing the enclosure discretisation step in the next section.

4.1 Enclosure discretisation

The first step towards developing the model was discretising the enclosure representing the boiler furnace into surface zones and volume zones. The enclosure in this study was developed on a three-dimensional Cartesian coordinate system along the positive x, y and z-coordinates plane where the width, length and the height of the enclosure is along the x-axis, y-axis and z-axis, respectively. The enclosure was then further divided into a finite number of increments along the x, y and z direction to make up a discretised enclosure. As a result, the enclosure consists of surface zones as well as volume zones. Each zone is represented by a centre node which holds information such as the location of the node in terms of its x, y and z-coordinates. The surface node also holds the surface normal vector as well as the surface area and the volume node hold the volume size. Figure 4.2 shows a representation of a discretised enclosure as well as a surface and volume zone with its centre node and information.

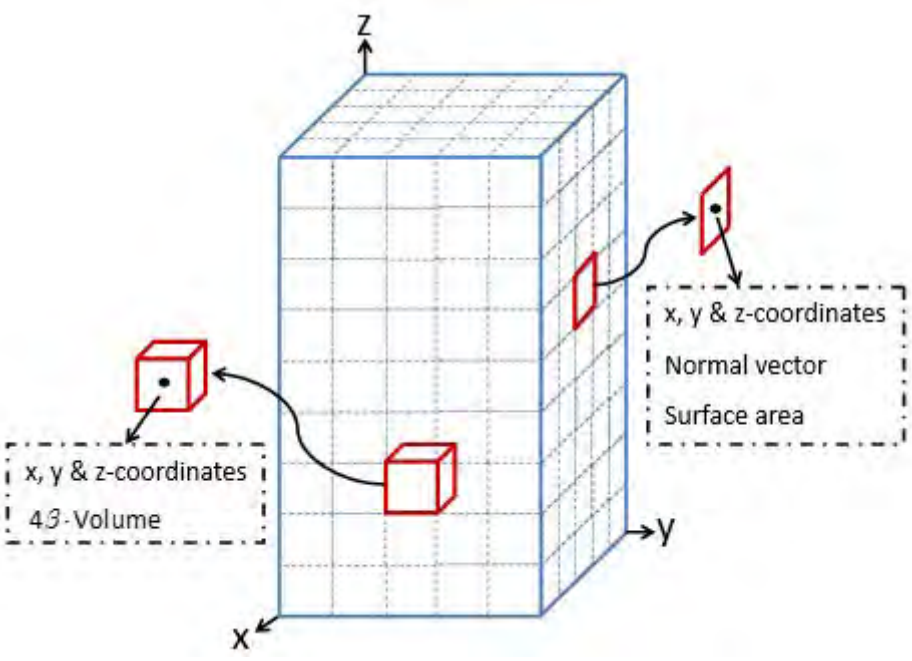

Figure 4.2. Discretised enclosure with a zoomed-in surface zone.

The x-coordinates of the nodes on the FRONT surface are equal to the width of the enclosure and the x-coordinates of the nodes on the BACK (also known as REAR) surface are equal to zero.

The y-coordinates of the nodes on the LEFT surface are zero and on the RIGHT surface, the y-coordinates of the nodes are equal to the length of the enclosure. Finally, the z-coordinates of the nodes on the BOTTOM surface are zero and on the TOP surface, the z-coordinates of the nodes are equal to the height of the enclosure. This is shown in Figure 4.3:

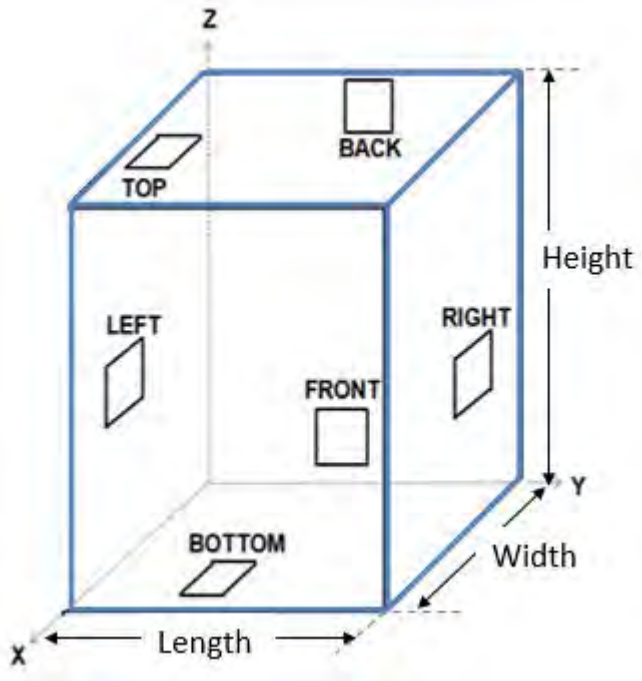

Figure 4.3. Furnace enclosure sides.

The input parameters to the model at this point are the enclosure dimensions (width, length and height) as well as the number of increments for the size discretisation along the width, length and height, respectively.

4.2 Medium radiative properties for primary case

As mentioned, the primary case is based on the assumption that the radiative properties of the participating medium are readily available. This means that the absorption coefficient (κ) and scattering coefficient (σ_s) of the participating medium are known and thus provided as inputs to the network model. The sum of the absorption and scattering coefficient of the medium is called the extinction coefficient (β) and is shown in Equation (4.1).

$$\beta = \kappa + \sigma_s \tag{4.1}$$

The extinction coefficient is used to perform the direct exchange area approximations.

4.3 Medium radiative properties for secondary case

The second case makes use of simplified approximations of the Mie theory and the WSGG model to estimate the radiative properties of the participating medium. The WSGG model is used to estimate the absorption coefficient of gases and simplified approximations of the Mie theory are used to estimate the radiative properties of the particles making up the participating medium in a coal-fired boiler furnace. The medium temperature is an important parameter because the estimation for the gas radiative properties is a function of medium temperature. In the case when medium temperatures are unknown, an iterative solution process is required (Khan, et al., 1997). The coal combustion flame in a coal-fired boiler furnace is a two-phase mixture of particles and gases. The evaluation of their radiative properties is discussed in Sections 4.3.1 and 4.3.2.

4.3.1 Radiative properties of gases

Gases are known to be non-gray, that is, their radiative properties are wavelength dependent. In this study, as mentioned, the WSGG model which accounts for the wavelength dependence of the gases is used to estimate the radiative properties of the gases. These gases are mainly water vapour and carbon dioxide. Multiple researches, namely Smith et al. (1982), Coppalle and Venisch (1983) and Truelove (Khan, et al., 1997) to mention a few, have published coefficients used in the WSGG model for the calculation of total gas emissivities. Subsequently, the total gas emissivities are used to estimate an absorption coefficient for the gaseous medium. A scattering coefficient is not calculated for the gaseous medium because as mentioned previously, the gaseous medium's scattering contribution is insignificant in the coal combustion participating medium. In developing this part of the model, the coefficients of Truelove (Khan, et al., 1997) and Smith et al. (1982) were employed. The coefficients of Truelove are tabulated in Table 4.1:

Table 4.1. Weighting factor coefficients by Truelove for p = 1 atm (Khan, et al., 1997).

i	$\kappa(\mathrm{m^{-1}atm^{-1}})$	$b_{1,i}$	$b_{2,i} \times 10^3$
1	0	0.423	0.0433
2	0.89	0.285	0.0513
3	15.5	0.227	-0.0676
4	240	0.065	-0.027

These coefficients are used in the polynomial shown in Equation (4.2) to calculate weighting factors (with the temperature value in Kelvin) (Khan, et al., 1997).

$$a_i(T_g) = b_{1,1} + b_{2,i} T_g \tag{4.2}$$

The weighting factors are then used to calculate the total gas emissivity from the WSGG model as (Smith, et al., 1982):

$$\varepsilon_g = \sum_{i}^{N_{gg}=4} a_i(T_g)\, 1 - \exp(-\kappa_i p L_m) \tag{4.3}$$

where p is the partial pressure and L_m is the mean beam length. From Equation (4.3), an effective absorption coefficient for the gaseous medium is calculated as (Coelho, 2002):

$$\kappa_g = \frac{1}{L_m} \ln\left(\frac{1}{1-\varepsilon_g}\right) \tag{4.4}$$

This then serve as the absorption coefficient of the gaseous medium.

The coefficients of Smith et al. (1982) are tabulated in Table 3.3. They were also applied in a similar fashion as described for the Truelove coefficients.

A case study available in literature for verifying the implementation of the WSGG model gives results of the radiation heat transfer rates on the walls of a three-dimensional cubic enclosure. These results can only be obtained after calculating the direct exchange areas, smoothing them and then solving the radiation heat transfer network in Scilab. Hence, the verification of the implementation of the WSGG model will be shown at a later stage once the direct exchange areas and the radiation heat transfer network have been solved and verified.

4.3.2 Radiative properties of particles

Calculating the absorption and scattering coefficients for the particles forming part of the coal combustion participating medium is a rather complex phenomena because the particles not only constantly undergo changes in size, but the particles also exist in a wide range of shapes (Smoot & Pratt, 1979). The most important step in approximating the radiative properties is calculating the absorption efficiency factors (Q_{abs}) and scattering efficiency factors (Q_{sca}) of coal, char and fly-ash.

These efficiency factors are calculated using mean particle diameters and complex index of refraction data. The complex index of refraction data of the particles are tabulated in Table 3.1. The Mie theory is a famous model for evaluating the efficiency factors for the particulate media, but it is known to be a time consuming and complex model. As a result, Kim and Lior (1995) proposed simplified approximations for the evaluation of efficiency factors for the particulate media which gives acceptable results. These approximations are thoroughly discussed in Section 3.4.1. It is however worth mentioning that any prediction of radiative properties usually has significant uncertainty associated with them and the results may only be regarded as fairly crude approximations (Li, et al., 2011). The absorption and scattering coefficients are then calculated as (Smoot & Pratt, 1979):

$$\kappa_p = \sum_i N_{p,i} Q_{abs,i} \frac{\pi D_i^2}{4}, m^{-1} \tag{4.5}$$

and

$$\sigma_s = \sum_i N_{p,i} Q_{sca,i} \frac{\pi D_i^2}{4}, m^{-1} \tag{4.6}$$

Here, the subscript i represents the different particle sizes that are considered for the calculations, D is the particle diameter, N_p is the particle number density and Q_{abs} as well as Q_{sca} are the absorption and scattering efficiency factors, respectively. Soot, which also form part of the particulate participating medium, only has an absorption coefficient and not a scattering coefficient, because like gases, it also scatters radiation in negligible amounts (Smoot & Pratt, 1979). The absorption coefficient of soot is traditionally calculated from (Modest, 2003):

$$\kappa_s = \frac{3.72 f_v C_0 T_g}{C_2} \tag{4.7}$$

Here $C_0 = \dfrac{36\pi nk}{(n^2 - k^2 + 2)^2 + 4n^2k^2}$ and $C_2 = 1.4388 \times 10^{-2}\ m\ K.$

where f_v is the soot volume fraction which ranges between 10^{-8} and 10^{-6} (Crnomarkovic & Sijercic, 2008) and T_g is the gas temperature.

The optical constants, *n* and *k* are called the absorptive and refractive indexes, respectively and is also called the complex index of refraction when presented as $m = n - ik$; for soot, $m = 2.20 - 1.12i$ (Crnomarkovic & Sijercic, 2008).

4.3.3 Verification of the implementation of the efficiency factor approximations from the Mie theory

To verify the implementation of the efficiency factor approximations by Kim and Lior (1995), the scattering efficiency factor of fly-ash approximated in this study was plotted against that of Kim and Lior (1995) and is shown in Figure 4.4:

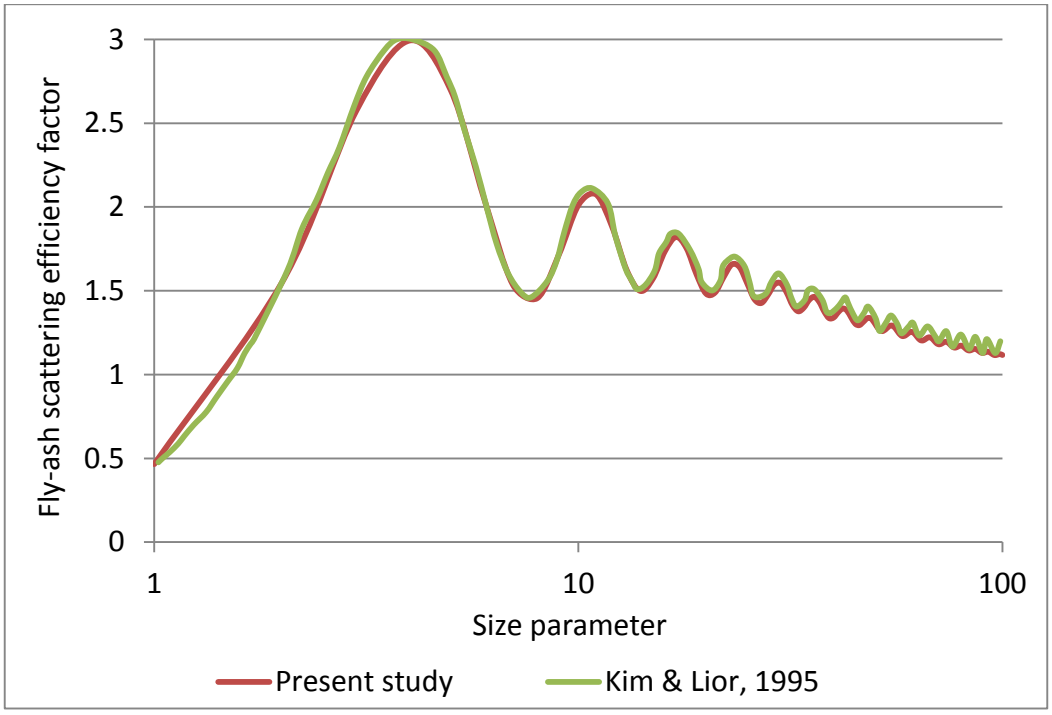

Figure 4.4. Scattering efficiency factor of fly-ash versus size parameter by the anomalous limit.

Figure 4.4 shows good agreement between the results of current study and that provided in the literature and confirms successful implementation of the model.

In this secondary case, the absorption coefficient (κ) of the medium is the sum of the gas absorption coefficient (κ_g) and the absorption coefficient of the particles (κ_p). The calculated scattering coefficient is denoted by σ_s. Once again, the sum of the absorption and scattering coefficient of the medium is the extinction coefficient (β) and is a used to perform the direct exchange area approximations.

The input parameters needed for the radiative properties in this case are:

- Particle diameters for coal, char, fly-ash and soot.
- Particle number density for coal, char and fly-ash.
- Volume fraction for soot.
- Densities for coal, char, fly-ash and soot.
- Medium temperatures.

Once the enclosure has been discretised and the radiative properties of the participating medium are known, the evaluation of the direct exchange areas can be performed.

4.4 Direct exchange area approximations

The evaluation of direct exchange areas involves a set of double area/area, area/volume and volume/volume integrals. Solving these integrals analytically is rather complex and therefore in this study the direct exchange areas are approximated through discrete numerical integration.

The surface-to-surface direct exchange area integral in Equation (4.8):

$$\overline{s_i s_j} = \int_{A_i}\int_{A_j} \exp(-\beta R)\frac{\cos\theta_i \cos\theta_j}{\pi R^2} dA_j dA_i \tag{4.8}$$

is approximated with Equation (4.9) as:

$$\overline{s_i s_j} = \sum_{i=1}^{N_s}\sum_{j=1}^{N_s} \exp(-\beta R)\frac{\cos\theta_i \cos\theta_j \Delta A_i \Delta A_j}{\pi R^2} \tag{4.9}$$

The extinction coefficient β is the absorption coefficient plus the scattering coefficient of the participating medium and has the unit of reciprocal length. The elemental areas on each discretised surface, is $\triangle A_i$ and $\triangle A_j$. The midpoints of the discretised surface are connected by a line of length, R. The line represents the beam of radiation leaving one surface and then intercepts the other. The x, y and z-coordinates of the midpoints on the elemental surfaces are used to calculate the length of *R* as:

$$|R| = \sqrt{(x_i - x_j)^2 + (y_i - y_j)^2 + (z_i - z_j)^2} \tag{4.10}$$

R forms polar angles, θ_i and θ_j with the surface normal vectors, n_i and n_j as seen in Figure 3.5a. The magnitudes of these angles are calculated using the dot product as:

$$\cos\theta_i = \frac{n_i \cdot R}{|n_i||R|} \quad and \quad \cos\theta_j = \frac{n_j \cdot R}{|n_j||R|} \tag{4.11}$$

Substituting Equations (4.10) and (4.11) into Equation (4.9) yields:

$$\overline{s_i s_j} = \sum_{i=1}^{N_s}\sum_{j=1}^{N_s} \exp(-\beta|R|) \frac{\left(\frac{n_i \cdot R}{|n_i||R|}\right)\left(\frac{n_j \cdot R}{|n_j||R|}\right)\Delta A_i \Delta A_j}{\pi |R|^2} \tag{4.12}$$

Equation (4.12) was then used to approximate the surface-to-surface direct exchange areas. The same procedure was followed for the surface-to-volume and volume-to-volume direct exchange area approximations. These are available in Appendix B.2.

The use of discrete numerical integration results in inherent errors that are inevitable. These errors lead to direct exchange areas that do not satisfy the energy conservation principles stipulated in Equations (3.31) and (3.32). This motivates the use of a smoothing technique for the direct exchange areas which is the next step of the model development.

4.5 Direct exchange area smoothing

This step ensures that the direct exchange areas satisfy reciprocity and energy conservation principles. Two smoothing techniques, namely least-squares smoothing using Lagrange multipliers (Larsen & Howell, 1986) and generalised Lawson smoothing (Lawson, 1995) were applied in this study. The idea was to compare the two techniques with data available in literature and eventually use the preferred one amongst the two for the network model. For both techniques, the set of direct exchange areas are assembled into one matrix as shown in Equation (4.13):

$$[X] = \begin{bmatrix} [\overline{ss}] & [\overline{sg}] \\ [\overline{sg}]^T & [\overline{gg}] \end{bmatrix} \tag{4.13}$$

4.5.1 Least-squares smoothing using Lagrange multipliers

For this technique, an objective function (*H*) was defined as (Larsen & Howell, 1986):

$$H = \sum_{i=1}^{N}\sum_{j=1}^{N}\frac{1}{2w_{ij}}\cdot\ x_{ij}^{'} - x_{ij}\ ^{2} \tag{4.14}$$

where *N* is the total number of surface and volume zones, w_{ij} are arbitrary weighting factors, $x_{ij}^{'}$ are the adjusted direct exchange area values and x_{ij} are the original direct exchange area values calculated in Section 4.4. The weighting factors are equal to the square of the original direct exchange area values so that the DEAs are adjusted in proportion to the originally calculated direct exchange areas, hence the weighting factors matrix W is:

$$[W] = \lfloor x_{ij}^{2} \rfloor \tag{4.15}$$

Furthermore, the Lagrangian for the Lagrange multiplier is defined as (Larsen & Howell, 1986):

$$L = H + \sum_{i=1}^{N}\lambda_i\left(g_i - g_i^{*}\right) \tag{4.16}$$

where λ_i are the Lagrange multipliers, g_i are the row-sum constraints and g_i^{*} are the column-sum constraints. These constraints are defined as (Larsen & Howell, 1986):

$$g_i = c_i - \sum_{j=1}^{N}x_{ij}^{'} \quad \text{for} \quad i = 1,2,\ldots,N \tag{4.17}$$

and

$$g_i^{*} = c_i - \sum_{j=1}^{N}x_{ji}^{'} \quad \text{for} \quad i = 1,2,\ldots,N \tag{4.18}$$

where

$$\sum_{j=1}^{N} x_{ij} = c_i \text{ where}$$
$$c_i = A_i \quad \text{for } i \le N_s$$
$$c_i = 4\beta V_i \quad \text{for } i > N_s \tag{4.19}$$

Substituting Equations (4.17) and (4.18) into Equations (4.16) gives (Larsen & Howell, 1986):

$$\begin{aligned} L &= H + \sum_{i=1}^{N} \lambda_i \left(g_i - g_i^* \right) \\ &= \sum_{i=1}^{N} \sum_{j=1}^{N} \frac{1}{2w_{ij}} \cdot \left(x_{ij}^{'} - x_{ij} \right)^2 + \sum_{i=1}^{N} \lambda_i \left(\left(c_i - \sum_{j=1}^{N} x_{ij}^{'} \right) + \left(c_i - \sum_{j=1}^{N} x_{ji}^{'} \right) \right) \end{aligned} \tag{4.20}$$

Partially differentiating L in Equation (4.20) with respect to $x_{ij}^{'}$ and equating to zero yields (Larsen & Howell, 1986):

$$\frac{\partial L}{\partial x_{ij}^{'}} = 0 = \frac{1}{w_{ij}} (x_{ij}^{'} - x_{ij}) - \left(\lambda_i + \lambda_j \right) \tag{4.21}$$

Finally, the adjusted values are obtained from (Larsen & Howell, 1986):

$$x_{ij}^{'} = x_{ij} + w_{ij} \cdot \left(\lambda_i + \lambda_j \right) \tag{4.22}$$

This details of this technique was discussed Section 3.2.3.

4.5.2 Generalised Lawson smoothing

Here, the sum of all the entries in the first column of matrix X in Equation (4.13) is equal to:

$$\sum_{i=1}^{N} x_{i1} = \sum_{j=1}^{N_s} \overline{s_i s_j} + \sum_{k=1}^{N_g} \overline{s_i g_k} \tag{4.23}$$

Every DEA entry in the first column was then multiplied with a deviation factor to get the new direct exchange area values:

$$x'_{i1} = x_{i1} \cdot \left(\frac{A_i}{\sum_{j=1}^{N_s} \overline{s_i s_j} + \sum_{k=1}^{N_g} \overline{s_i g_k}} \right) \tag{4.24}$$

The new direct exchange areas of the first column transposed are then set equal to the first row of the next DEA matrix to preserve reciprocity. The process is repeated for every column and row until the N_s^{th} column and row. For every DEA entry in the $N_s + 1^{th}$ column of matrix X, the DEA was multiplied with another deviation factor to get the new direct exchange area values:

$$x'_{i(N_s+1)} = x_{i(N_s+1)} \cdot \left(\frac{4\beta V_i}{\sum_{j=1}^{N_s} \overline{g_i s_j} + \sum_{k=1}^{N_g} \overline{g_i g_k}} \right) \tag{4.25}$$

Again, every entry in the $N_s + 1^{th}$ column transposed is then set equal to the $N_s + 1^{th}$ row of the next DEA matrix to preserve reciprocity. The process is then repeated for every column and row until the last column and row. This progression leads to a matrix that holds direct exchange areas that satisfy reciprocity rules and energy conservation principles. This was done using Excel.

4.6 Direct exchange area verifications

Before going onto the last step of solving the radiation heat transfer network model, the calculations of the direct exchange areas were verified using different approaches. The different approaches include comparison with other numerical techniques as well as with an analytical solution available in literature. The motivation for the verification step at this point was to ensure that the direct exchange areas were satisfactory for its implementation into the zonal method since the calculation of direct exchange areas is the basis of the zonal method.

4.6.1 Present study's DEA calculations compared to Hottel & Sarofim (1967):

The initial effort made towards verifying the direct exchange areas calculated in this study was to compare them to the numerical equations by Hottel & Sarofim (1967). All these equations are available in Appendix C.1. For illustration purposes, the surface-to-surface direct exchange area equation by Hottel & Sarofim (1967) for a parallel $\text{Bottom} \Leftrightarrow \text{Top}$ surface is:

$$\overline{s_j s_i}(\|) = B^2 \cdot \frac{\exp(-\beta R) \cdot \left(\frac{\triangle z}{B}\right)^2}{\pi \cdot (\frac{R}{B})^4} \qquad \text{Bottom} \Leftrightarrow \text{Top} \tag{4.26}$$

where B is the surface side length, β is the extinction coefficient of the medium, R is the distance between the two surfaces and $\triangle z$ is the difference between the z-coordinates of the two surfaces. Equation (4.26) is accompanied by Figure 4.5 which shows the positions of $\triangle z$ and B for parallel $\text{Bottom} \Leftrightarrow \text{Top}$ surfaces:

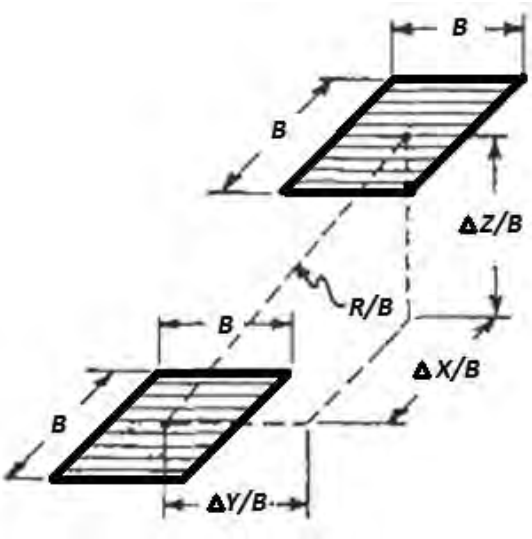

Figure 4.5. Geometry of direct exchange between parallel squares (Hottel & Cohen, 1958).

The comparison was conducted for a cubic enclosure with side lengths of 4 m that is discretised into four nodes per surface. Furthermore, the enclosure holds a medium that has an extinction coefficient (β) of 0.1 m^{-1}.

The direct exchange area results of the top surface of the enclosure obtained from the model in this study and the numerical technique by Hottel & Sarofim (1967) are tabulated in Table 4.2:

Table 4.2. DEAs of present study versus the numerical technique of Hottel & Sarofim (1967).

Present study	**Numerical technique by Hottel & Sarofim (1967)**
$DEA_{Study} = \begin{pmatrix} 0.213 \\ 0.130 \\ 0.130 \\ 0.087 \end{pmatrix} m^2$	$DEA_{Hottel\,\&\,Sarofim} = \begin{pmatrix} 0.213 \\ 0.130 \\ 0.130 \\ 0.087 \end{pmatrix} m^2$

It is evident that the results of the present study and the numerical technique shown in Table 4.2 yield identical results.

4.6.2 Present study's DEA calculations compared to view factors

Next, the surface-to-surface direct exchange areas calculated for an enclosure containing a non-participating medium (extinction coefficient, $\beta = 0$) were compared to analytically solved view factors. A short derivation is shown in Equation (4.27) which indicates how surface-to-surface direct exchange areas relate to view factors.

$$\begin{aligned} \overline{s_i s_j} &= \int_{A_i}\int_{A_j} \exp(-\beta R)\frac{\cos\theta_i \cos\theta_j}{\pi R^2} dA_j dA_i \\ &\text{for} \quad \beta = 0 \quad \Rightarrow \quad \exp(-\beta R) = 1 \\ \therefore \overline{s_i s_j} &= \int_{A_i}\int_{A_j} \frac{\cos\theta_i \cos\theta_j}{\pi R^2} dA_j dA_i \\ \frac{\overline{s_i s_j}}{A_i} &= \frac{1}{A_i}\int_{A_i}\int_{A_j} \frac{\cos\theta_i \cos\theta_j}{\pi R^2} dA_j dA_i \\ &= F_{ij} \end{aligned} \tag{4.27}$$

View factors for rectangular/cubic enclosures are calculated for parallel and perpendicular aligned rectangles/cubes. The two alignments are illustrated in Figure 4.6:

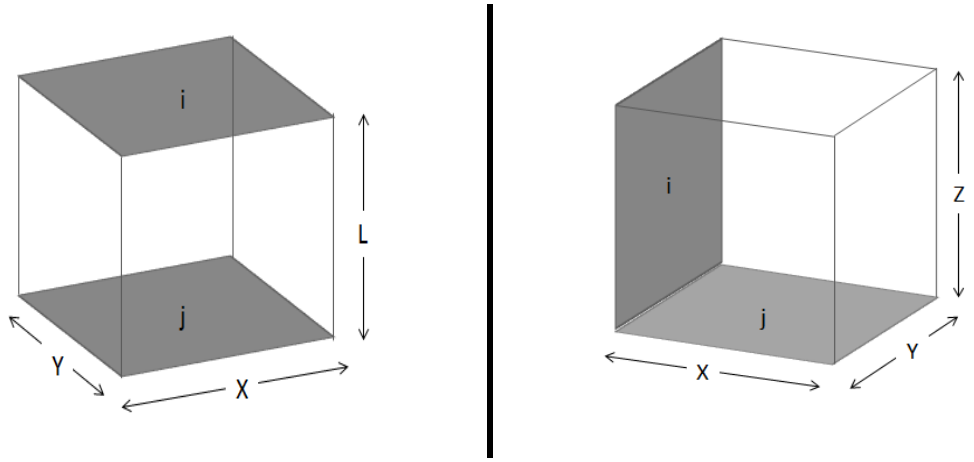

Figure 4.6. Parallel and perpendicular aligned rectangles, respectively (Incropera, et al., 2007).

The analytical expression for view factors between ***parallel aligned rectangular*** surfaces are given by Incropera et al. (2007) as:

$$\bar{X} = {}^{X}\!/_{L}; \quad \bar{Y} = {}^{Y}\!/_{L}$$

$$F_{ij} = \frac{2}{\pi \bar{X}\bar{Y}} \left\{ \begin{aligned} &\ln\left[\frac{(1+\bar{X}^2)(1+\bar{Y}^2)}{1+\bar{X}^2+\bar{Y}^2}\right]^{1/2} + \bar{X}^2(1+\bar{Y}^2)^{1/2}\tan^{-1}\frac{\bar{X}}{(1+\bar{Y}^2)^{1/2}} - \bar{X}^2\tan^{-1}\bar{X} + \\ &\bar{Y}^2(1+\bar{X}^2)^{1/2}\tan^{-1}\frac{\bar{Y}}{(1+\bar{X}^2)^{1/2}} - \bar{Y}^2\tan^{-1}\bar{Y} \end{aligned} \right\} \tag{4.28}$$

The analytical expression for view factors between ***perpendicular aligned rectangular*** surfaces are given by Incropera et al. (2007) as:

$$H = {}^{Z}\!/_{W}; \quad W = {}^{Y}\!/_{X}$$

$$F_{ij} = \frac{1}{\pi W} \left\{ \begin{aligned} &\frac{1}{4}\ln\left[\frac{(1+W^2)(1+H^2)}{1+W^2+H^2}\left(\frac{W^2(1+W^2+H^2)}{(1+W^2)(W^2+H^2)}\right)^{W^2}\left(\frac{H^2(1+W^2+H^2)}{(1+H^2)(W^2+H^2)}\right)^{H^2}\right] + \\ &W\tan^{-1}\frac{1}{W} + H\tan^{-1}\frac{1}{H} - (H^2+W^2)^{1/2}\tan^{-1}\frac{1}{(H^2+W^2)^{1/2}} \end{aligned} \right\} \tag{4.29}$$

Functions were written in Mathcad for the two alignments and the function codes are available in Appendix C.2. The comparison the DEA calculations and view factors were conducted for an enclosure with a width, length and height of 5 m, 5 m and 10 m, respectively. Table 4.3 holds the analytical view factor solution for the $5\,\text{m} \times 5\,\text{m} \times 10\,\text{m}$ enclosure:

Table 4.3. Analytically solved view factors.

Analytically solved view factors
$V = \begin{pmatrix} 0 & 0.286 & 0.233 & 0.233 & 0.241 & 0.241 \\ 0.286 & 0 & 0.233 & 0.233 & 0.241 & 0.241 \\ 0.116 & 0.116 & 0 & 0.069 & 0.116 & 0.116 \\ 0.116 & 0.116 & 0.069 & 0 & 0.116 & 0.116 \\ 0.241 & 0.241 & 0.233 & 0.233 & 0 & 0.286 \\ 0.241 & 0.241 & 0.233 & 0.233 & 0.286 & 0 \end{pmatrix}$

Table 4.4 hold the view factors from the model developed in this study after smoothing. The left hand side column of Table 4.4 shows the view factors for the enclosure without discretisation. The right hand side column of Table 4.4 shows the view factors for the enclosure after discretising it into 5, 5 and 10 nodes along the width, length and height of the enclosure, respectively.

Table 4.4. View factors from the model without and with discretisation.

$(1\times1\times1)$ nodes	$(5\times5\times10)$ nodes
$V = \begin{pmatrix} 0 & 0.257 & 0.228 & 0.228 & 0.257 & 0.257 \\ 0.257 & 0 & 0.228 & 0.228 & 0.257 & 0.257 \\ 0.114 & 0.114 & 0 & 0.090 & 0.114 & 0.114 \\ 0.114 & 0.114 & 0.090 & 0 & 0.114 & 0.114 \\ 0.257 & 0.257 & 0.228 & 0.228 & 0 & 0.257 \\ 0.257 & 0.257 & 0.228 & 0.228 & 0.257 & 0 \end{pmatrix}$	$V = \begin{pmatrix} 0 & 0.285 & 0.233 & 0.233 & 0.241 & 0.241 \\ 0.285 & 0 & 0.233 & 0.233 & 0.241 & 0.241 \\ 0.116 & 0.116 & 0 & 0.069 & 0.116 & 0.116 \\ 0.116 & 0.116 & 0.069 & 0 & 0.116 & 0.116 \\ 0.241 & 0.241 & 0.233 & 0.233 & 0 & 0.285 \\ 0.241 & 0.241 & 0.233 & 0.233 & 0.285 & 0 \end{pmatrix}$

The view factors in Table 4.4 for the discretised case are in good agreement with the analytically calculated view factors in Table 4.3. This is an indication that discretisation yields better results. To further substantiate the idea of discretisation, Figure 4.7 shows how the view factors from the model for the front surface to the back surface approaches the analytical solution with finer discretisation. This was done for the model's view factors before and after smoothing.

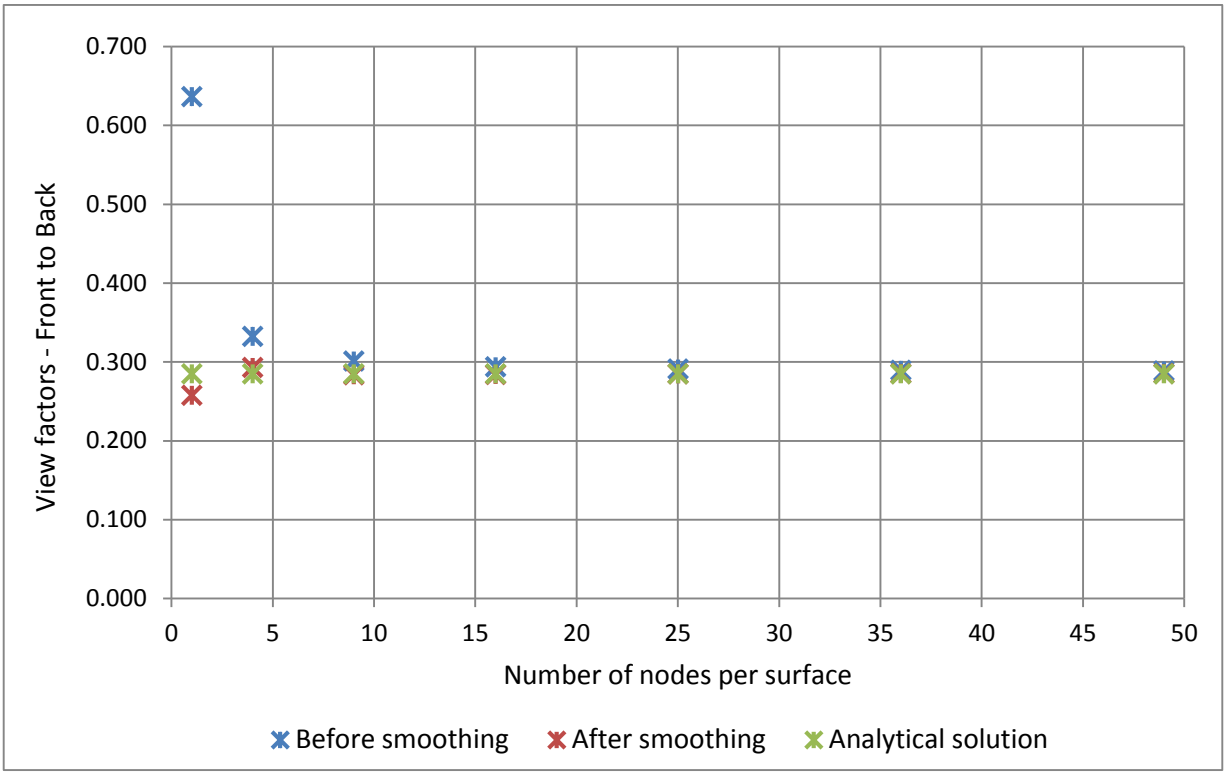

Figure 4.7. Front to back view factors with increase in discretisation.

4.6.3 Present study's DEA calculations compared to Tucker (1986):

Another comparison of the calculated direct exchange areas was with Tucker's correlations for the direct exchange areas. Amongst others, the correlation for direct exchange areas between a pair of surface zones is given by (Tucker, 1986):

$$\overline{s_j s_i} = B^2 \, C \cdot \exp(-A \cdot \beta B) \quad \text{where}$$
$$A = a_0 + a_1 \cdot \beta B + \ldots + a_4 \cdot \beta B^4 \tag{4.30}$$

Here, B is the enclosure side length as indicated in Figure 3.7 above; A and C are correlation coefficients found in Appendix C.3 and β is the extinction coefficient of the medium. A cubic enclosure with side lengths of 4 m, discretised into four nodes per side was used to generate results for the direct exchange areas before after smoothing at different extinction coefficients using the model. The results were then plotted and compared to Tucker's correlations as schematically represented in Figure 4.8, Figure 4.9 and Figure 4.10:

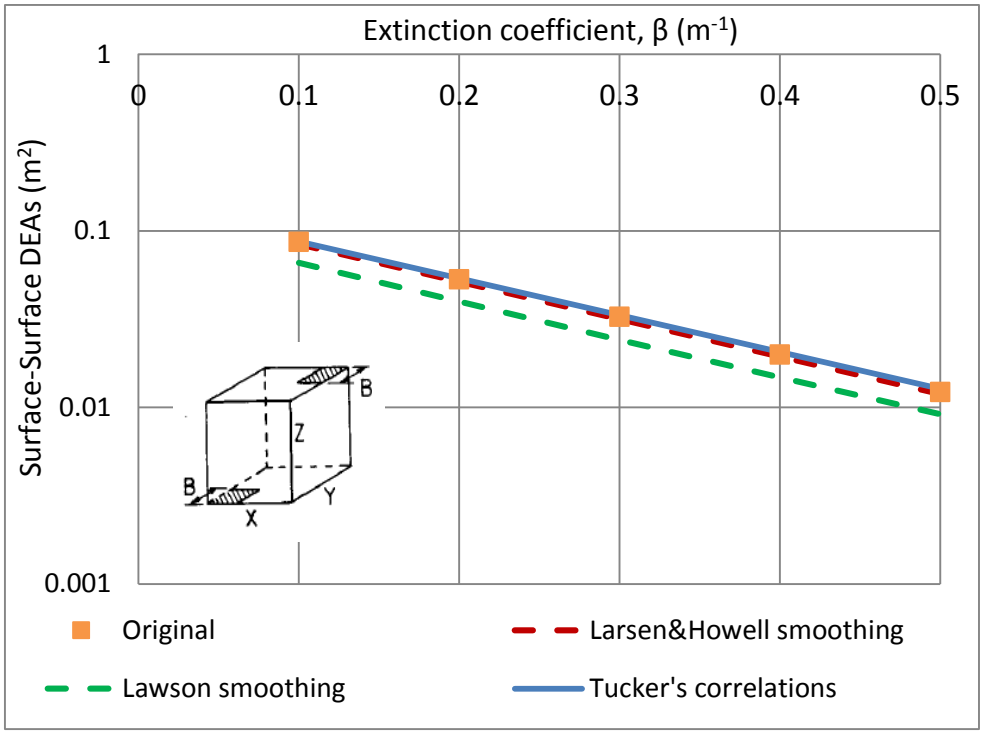

Figure 4.8. Surface-to-surface direct exchange areas comparisons.

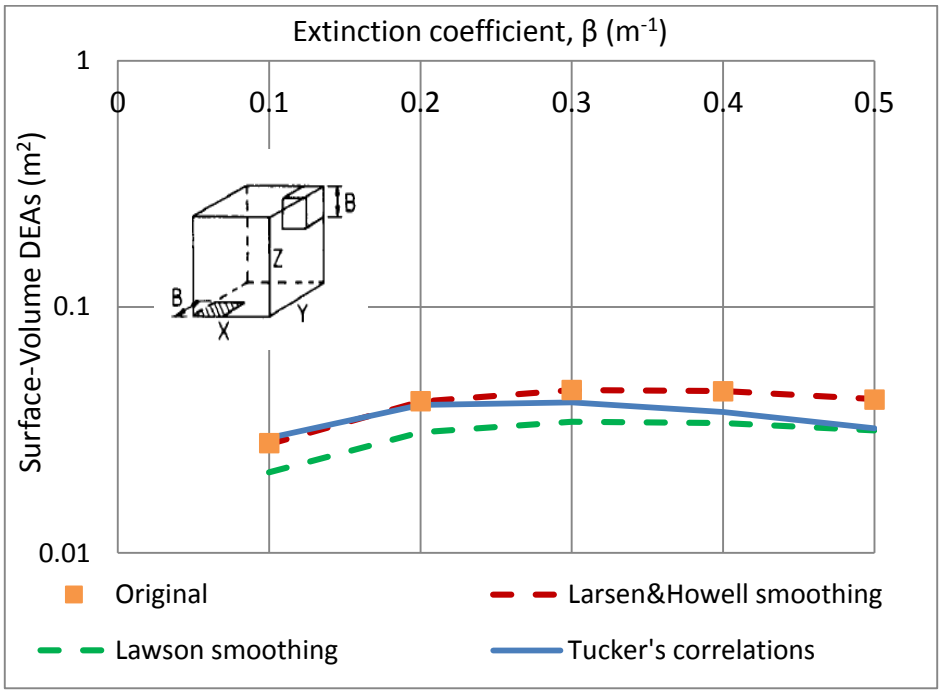

Figure 4.9. Surface-to-volume direct exchange areas comparisons.

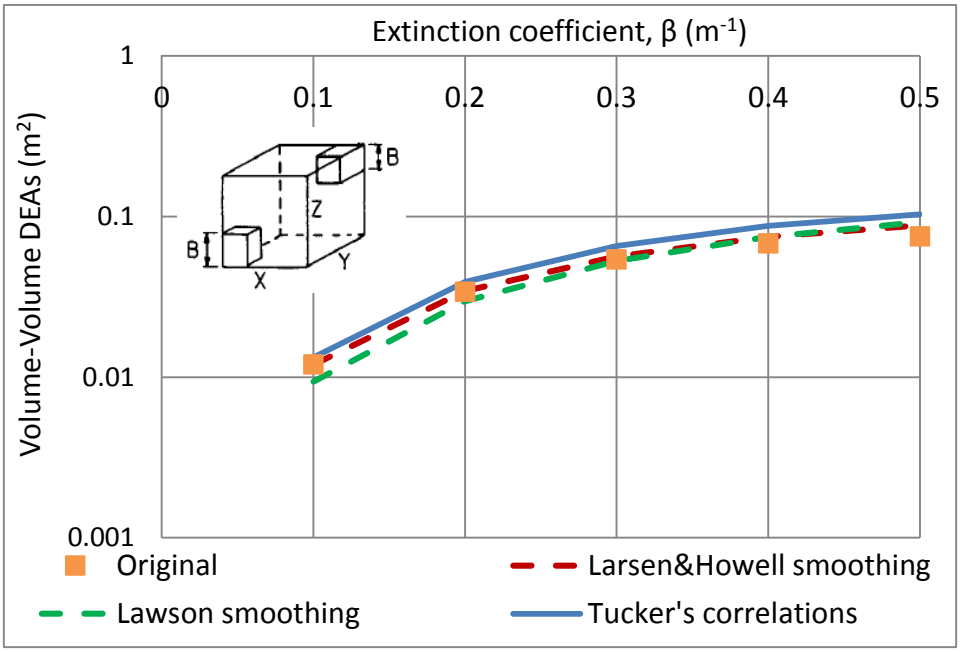

Figure 4.10. Volume-to-volume direct exchange areas comparisons.

Figure 4.8, Figure 4.9 and Figure 4.10 all display the originally approximated DEAs, the DEAs after smoothing by means of least squares smoothing using Lagrange multipliers by Larsen and Howell (1986) and generalised smoothing by Lawson (1995). It is clear from Figure 4.8 and Figure 4.9 that the DEAs after smoothing using Lawson's smoothing deviates significantly from the originally calculated direct exchange areas. Since the idea is that the DEAs are adjusted in proportion to the original DEAs. As a result, the least squares smoothing using Lagrange multipliers technique was used for the model going forward. Furthermore, these direct exchange areas correlates very well with those of Tucker (1986).

4.7 Radiation heat transfer network

As mentioned, the radiation heat transfer network is the last step of the model development process. The radiation heat transfer network model was developed starting with the simplest case of radiation heat transfer for a non-participating medium where heat fluxes were calculated on the surfaces of the enclosure. Next, the network was solved for an enclosure containing an emitting and absorbing medium. Finally, the network was solved for an enclosure containing an emitting, absorbing and scattering medium. The development of the latter is shown in this section and can be used to solve the radiation heat transfer network for both an emitting and absorbing medium as well as an emitting, absorbing and scattering medium.

The radiation heat transfer network is based on the zonal method. This method requires that energy balances are performed on every surface and volume zone by employing pre-calculated direct exchange areas and then solving the set of energy balances simultaneously (Hottel & Sarofim, 1965). A schematic representation of an energy balance on a surface zone is shown in Figure 4.11 and mathematically shown in Equation (4.31):

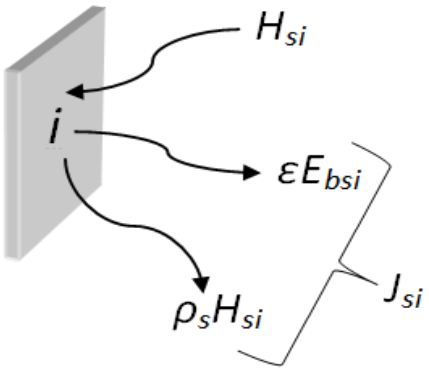

$$\begin{aligned} q_{s,i} &= q_{out} - q_{in} \\ &= (q_{emission} + q_{reflection}) - q_{irradiation} \\ &= (\varepsilon_i E_{bs,i} + \rho_s H_{s,i}) - H_{s,i} \\ \text{for} \quad J_{s,i} &= \varepsilon E_{bs,i} + \rho_s H_{s,i} \\ q_{s,i} &= J_{s,i} - H_{s,i} \end{aligned} \tag{4.31}$$

Figure 4.11. Radiation heat transfer on a surface zone.

In Equation (4.31), ε_i and ρ_s are the surface emissivity and reflectivity, respectively with respect to surface i. Furthermore, the outgoing heat flux, in other words, the rate at which radiation leaves the surface zone per unit area is called radiosity, $J_{s,i}$. Radiosity is due to emission, $\varepsilon_i E_{bs,i}$ and reflection, $\rho_s H_{s,i}$ in all directions and the fact that radiation goes in all directions is an indication that the surfaces are diffuse. 'Diffuse surfaces' is an underlying assumption of the zonal method. The irradiation denoted by $H_{s,i}$ is defined as the rate at which radiation is incident on a surface from all directions per unit area of the surface (Incropera, et al., 2007).

Multiplying the heat flux in Equation (4.31) with the surface area in terms of direct exchange areas, the radiation heat transfer rate on a surface zone becomes:

$$Q_{s,i} = \varepsilon_i \left(A_i E_{bs,i} - \sum_{j=1}^{N_s} \overline{s_i s_j} J_{s,j} - \sum_{k=1}^{N_g} \overline{s_i g_k} J_{g,k} \right), \; i = 1,2,\ldots,N_s \tag{4.32}$$

An energy balance on a volume zone is shown in Appendix B.3. The process of substitution and rearranging of Equation (4.32) and the radiation heat transfer rate on a volume zone leads to Equations (4.33) and (4.34):

$$\sum_{j=1}^{N_s}\left(\frac{\delta_{ij}}{\varepsilon_j}-\frac{\rho_{sj}}{\varepsilon_j}\frac{\overline{s_i s_j}}{A_j}\right)h_{s,j}-\sum_{k=1}^{N_g}\left(\frac{\overline{s_i g_k}\omega_k}{4\kappa_k V_k}\right)h_{g,k} = \sum_{j=1}^{N_s}\overline{s_i s_j}\varepsilon_j\ E_{bs,j}+\sum_{k=1}^{N_g}\overline{s_i g_k}(1-\omega_k)\,E_{bg,k},\ i=1,2,\ldots,N_s \tag{4.33}$$

$$-\sum_{j=1}^{N_s}\left(\frac{\overline{g_i s_j}}{A_j}\frac{\rho_{sj}}{\varepsilon_j}\right)h_{s,j}+\sum_{k=1}^{N_g}\left(\frac{\delta_{ik}}{1-\omega_k}-\frac{\overline{g_i g_k}\omega_k}{4\kappa_k V_k}\right)h_{g,k} = \sum_{j=1}^{N_s}\overline{g_i g_j}\varepsilon_j\ E_{bs,j}+\sum_{k=1}^{N_g}\overline{g_i g_k}(1-\omega_k)\,E_{bg,k},\ i=1,2,\ldots,N_g \tag{4.34}$$

Here, $j=1,2,\ldots,N_s$ and $k=1,2,\ldots,N_g$. Furthermore, $h_{s,j}=\varepsilon_j A_j H_{s,j}$ and $h_{g,k}=\kappa_k V_k H_{g,k}$ are the irradiation on the surface and volume zones. Also, δ_{ij} is a kronecker's delta function, ω_k is the scattering albedo, κ_k is the absorption coefficient of the medium and $E_{bs,j}$ as well as $E_{bg,k}$ are the surface and medium emissive powers. Detailed derivatives of Equations (4.33) and (4.34) are found in Appendix B.3. For simplicity, Equations (4.33) and (4.34) are rewritten in terms of the *T, U, S, V, Q, W, R* and *X* matrices as:

$$T\cdot h_s - U\cdot h_g = S\cdot E_{bs}+V\cdot E_{bg} \tag{4.35}$$

and

$$-Q\cdot h_s + W\cdot h_g = R\cdot E_{bs}+X\cdot E_{bg} \tag{4.36}$$

It is from Equations (4.35) and (4.36) that certain terms are cancelled out to suite the assumptions made in specific cases, for instance, when computing radiation heat transfer in emitting and absorbing media without scattering, matrix *U* becomes zero since the scattering albedo, ω is then equal to zero. However, the model is developed in such a way that it can solve the radiation heat transfer network for emitting-absorbing media without scattering as well as emitting-absorbing media with scattering.

Furthermore, the radiation heat transfer network can be solved for two scenarios. The one is solving surface and volume heat fluxes for known surface and medium temperatures.

The other is solving surface heat fluxes and medium temperature distributions for known surface temperatures and heat source terms. For an emitting-absorbing-scattering medium, the evaluations of the two scenarios are discussed in sections 4.7.1 and 4.7.2.

4.7.1 Known surface and medium temperatures

For known surface and gas temperatures, the irradiation in Equations (4.35) and (4.36) for surface and volumes zones are obtained from matrix inversion as:

$$h_s = P^{-1}\left[C \cdot E_{bs} + D \cdot E_{bg}\right] \tag{4.37}$$

and

$$h_g = W^{-1}\left[(\mathrm{Q} \cdot P^{-1} \cdot C + \mathrm{R}) \cdot E_{bs} + (\mathrm{Q} \cdot P^{-1} \cdot D + \mathrm{X}) \cdot E_{bg}\right] \tag{4.38}$$

where,

$$P = T - U \cdot W^{-1} Q, \quad C = S + U \cdot W^{-1} R, \quad D = V + U \cdot W^{-1} X \tag{4.39}$$

Equations (4.37) and (4.38) are then substituted into Equations (4.40) and (4.41) to calculate unknown surface and volume heat fluxes, respectively.

$$q_{s,i} = \frac{1}{A_i}(\varepsilon_i A_i E_{bs,i} - h_{s,i}) \tag{4.40}$$

and

$$q_{g,i} = \frac{1}{A_i}(4\kappa_i V_i E_{bg,i} - h_{g,i}) \tag{4.41}$$

Thus, the result of this scenario is surface and volume/medium heat fluxes. Section 4.7.2 will present the second scenario that can also be solved using the model in this study.

4.7.2 Known surface temperatures and heat source terms

For this scenario, a heat source term is introduced as:

$$Q_{g,i} = 4\kappa_i V E_{bg,i} - h_{g,i} \tag{4.42}$$

The medium emissive power (E_{bg}) is obtained from substituting Equations (4.42) into (4.38) and rearranging to get:

$$E_{bg} = \left[4\kappa V - W^{-1} \cdot \mathrm{Q} \cdot P^{-1} \cdot D + \mathrm{X}\right]^{-1} \left[W^{-1} \cdot \mathrm{Q} \cdot P^{-1} \cdot C + \mathrm{R}\right] \cdot E_{bs} + Q_g \tag{4.43}$$

The medium temperature distributions can then be calculated from Equation (4.43). Equation (4.43) can further be substituted into Equations (4.37) and subsequently into Equations (4.40) to finally obtain the surface heat fluxes.

Hence, the result of this scenario is medium temperature and surface heat flux distributions.

Finally, the input parameters to the network model are listed as:

- Enclosure dimensions and discretisation size.
- Surface emissivities.
- Primary case **or** Secondary case.
- <u>For scenario 1:</u> Surface and medium temperatures **or** <u>for scenario 2:</u> Surface temperatures and heat source terms.

4.8 Sample calculation in Mathcad

A verification step was conducted for the complete network model in the form of a sample calculation on a different software package, namely Mathcad. For this calculation, a rectangular enclosure of dimensions, 2 m by 2 m by 4 m along the length, width and height, discretised into two nodes per axis was considered. The enclosure has a surface emissivity of 0.7 and encloses a medium with an extinction coefficient of 0.4 m^{-1}. Furthermore, a volume heat source of 5 kW/m^3 was specified.

The result of this scenario is surface heat fluxes and medium temperature distributions. The results for the net surface heat fluxes for each surface making up the enclosure are shown in Figure 4.12, for both the Scilab and Mathcad programs:

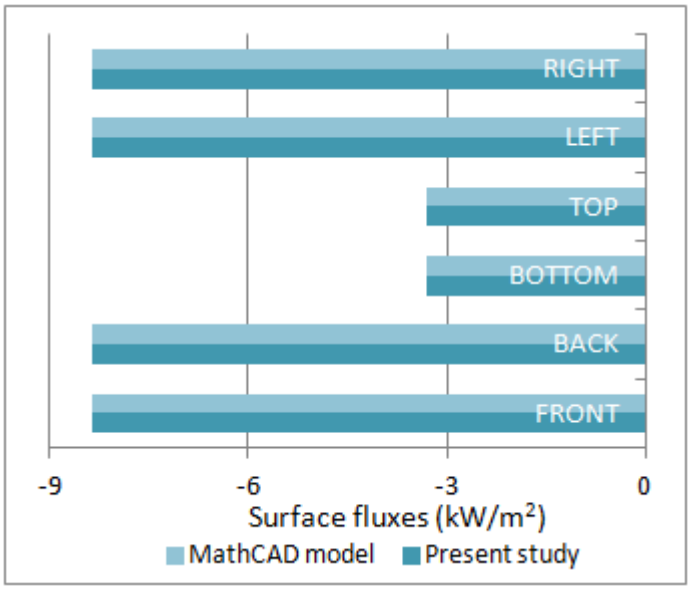

Figure 4.12. Surface heat fluxes.

Figure 4.13 shows the medium temperature distribution for each volume zone. The enclosure had eight volume zones. The reason for the uniform temperature is because a uniform heat source term was specified.

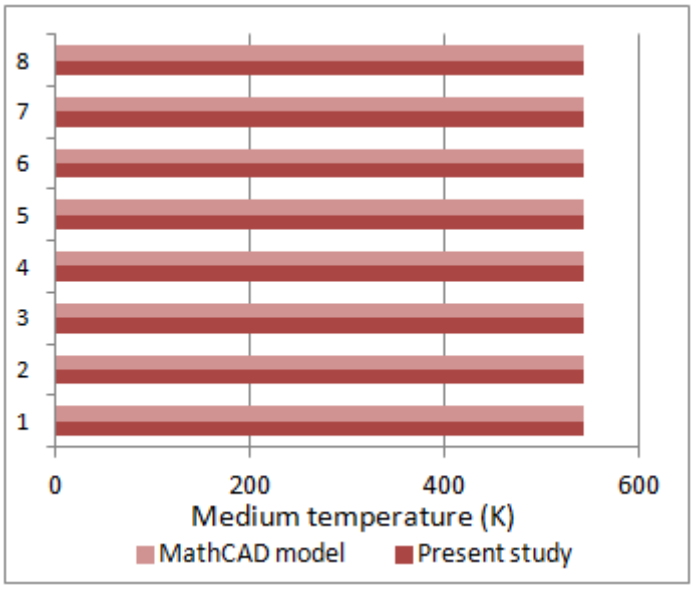

Figure 4.13. Medium temperature distributions.

It is clear from both Figure 4.12 and Figure 4.13 that Scilab and Mathcad yields identical results. Parts of the Mathcad sample calculation are available in Appendix D.

This verification steps indicated that the model developed in this study was implemented correctly in the Scilab software. To answer the question of whether the right model was being developed, a validation step was introduced.

4.9 Radiation heat transfer network model validation

The model developed in this study was validated using the celebrated case study discussed in the literature review (Section 2.3.1). In this case study, a three-dimensional enclosure representing an idealised furnace with a length, width and height of 2 m, 2 m and 4 m, respectively was used. The enclosure is discretised into five nodes along the x and y-axes and 10 nodes along the z-axis. The furnace is filled with an emitting-absorbing participating medium that does not scatter radiation. The medium has an extinction coefficient of 0.5 m^{-1} throughout and a heat source term that is equivalent to 5 kW/m^3 is uniformly distributed in all the volume zones. The boundary conditions of the enclosure are tabulated in Table 4.5:

Table 4.5. Enclosure boundary conditions (Ebrahimi, et al., 2004).

Bottom surface (z = 0 m) - (firing end wall)	T = 1200 K	ε = 0.85	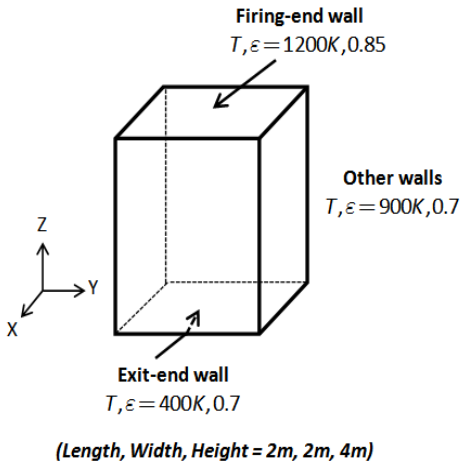
Top surface (z = 4 m) -(Exit end wall)	T = 400 K	ε = 0.70	
Others -(Side walls)	T = 900 K	ε = 0.70	

Figure 4.14 shows the medium temperature distributions inside the furnace volume at different heights. These medium temperature distribution results were obtained from the model developed in the present study and were compared to the results provided by Ebrahimi et al. (2004) and Borjini et al. (2003).

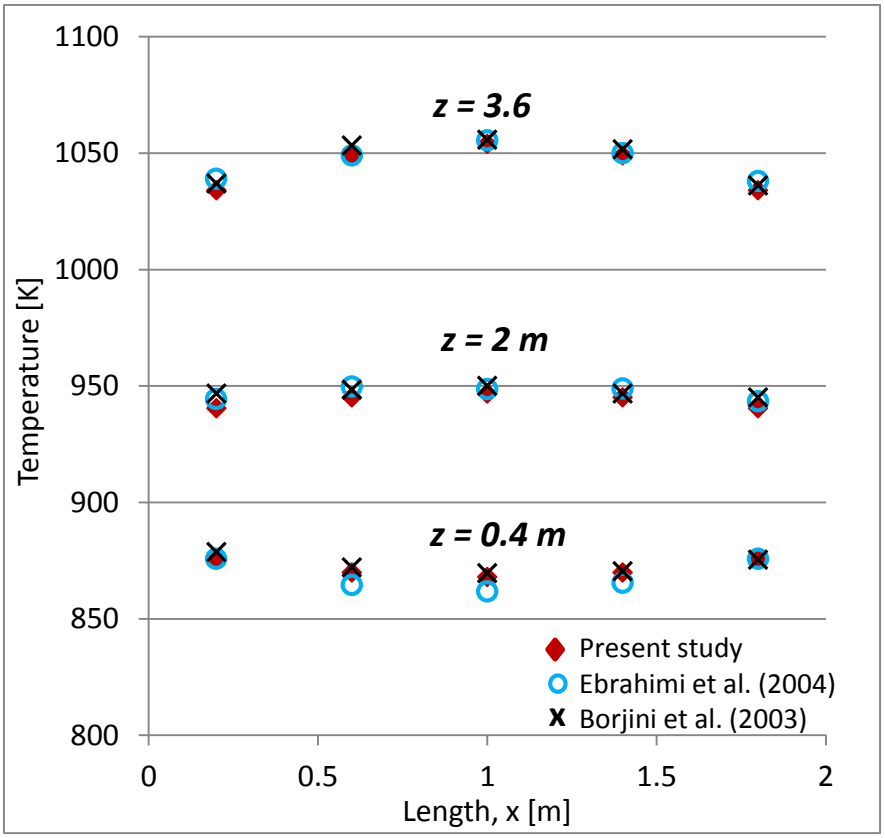

Figure 4.14. Gas temperature distributions at different heights in the enclosure along the length at a width of 0.6 m.

From Figure 4.14 it can be seen that the medium temperatures are highest (varying around 1050 K) closer to the firing-end wall where the wall temperature is 1200 K and lowest (varying between 850 K and 900 K) closer to the exit-end wall where the wall temperature is 400 K. Figure 4.14 also indicates a good agreement between the medium temperature distribution results of this study and the results provided in literature by Ebrahimi et al. (2004) and Borjini et al. (2003).

4.10 Verification of the implementation of the WSGG model

As mentioned, the case study available in literature for verifying the implementation of the WSGG model gives results of the radiation heat transfer rates on the walls of a three-dimensional cubic enclosure. At this point, the direct exchange areas and the radiation heat transfer network has been solved and verified, therefore the implementation of the WSGG model as discussed in Section 4.3.1 can finally be verified. The WSGG models based on the weighting factor coefficients of Smith et al. (1982), and Truelove (Khan, et al., 1997) are compared to the case study from literature.

The case study reported by Khan et al. (1997) is based on a cubic enclosure with side lengths of 1 m. The bottom surface temperature and emissivity was specified to be 300 ^{o}C and 0.27, respectively.

All the other surfaces had a surface temperature and emissivity of 1127 ^{o}C and 0.23, respectively. The medium temperature was specified to be 727 ^{o}C. These temperatures and emissivities were inputs to the network model developed in this study.

Figure 4.15 shows the net radiation heat transfer rate results from employing the weighting coefficients of Truelove (Khan, et al., 1997) and Smith et al. (1982) in the WSGG model. These results are compared to those published by Khan et al. (1997):

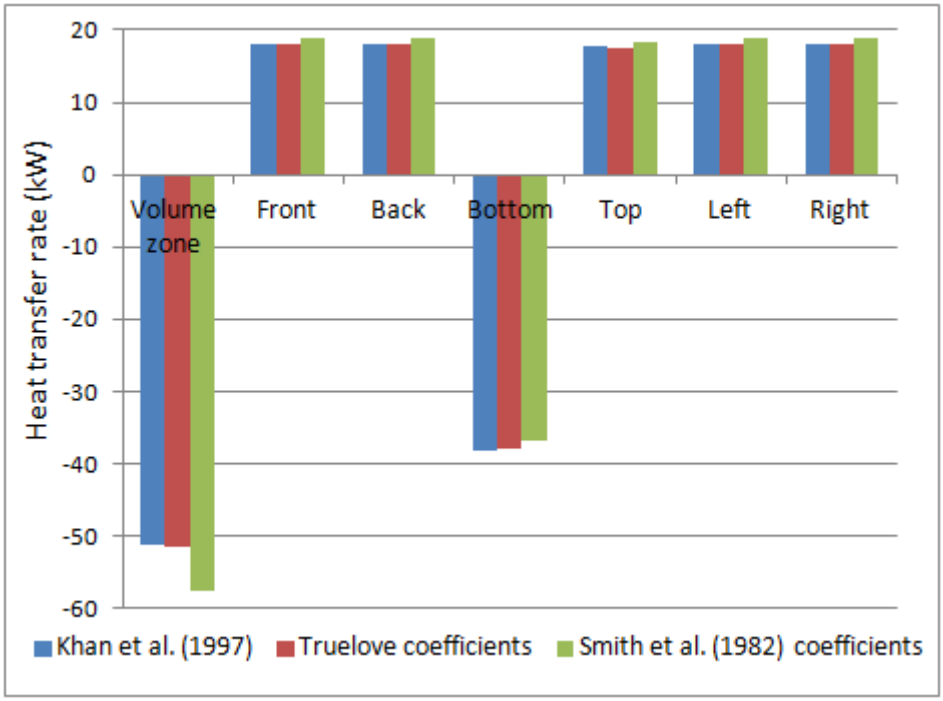

Figure 4.15. Heat transfer rates from the WSGG model.

It is clear from Figure 4.15 that the implementation of the WSGG model was successful. It is also evident that the radiation heat transfer rates obtained from employing the coefficients of Truelove correlates very well with those of Khan et al. (1997) with a maximum error of 1.9%. The maximum error for using the coefficients of Smith et al. (1982) was 12%. As a result, the coefficients of Truelove were implemented in the radiation heat transfer network developed in this study.

Network model input parameters

All the input parameters of the radiation heat transfer network developed in this study are tabulated in Table 4.6**:**

Table 4.6. Table of input parameters.

<table>
<tr><td colspan="3">> Enclosure dimensions and discretisation size.
> Surface emissivities.</td></tr>
<tr><td>Primary case input parameters</td><td colspan="2">Secondary case input parameters:</td></tr>
<tr><td>> Medium absorption and scattering coefficients.</td><td>> Particle diameters for coal, char, fly-ash and soot.
> Particle number density for coal, char and fly-ash.</td><td>> Volume fraction for soot.
> Densities for coal, char, fly-ash and soot.
> medium temperatures</td></tr>
<tr><td colspan="3">> <u>For scenario 1:</u> Surface and medium temperatures or <u>for scenario 2:</u> Surface temperatures and heat source terms</td></tr>
</table>

Finally, a schematic representation of the radiation heat transfer network solution methodology developed in this study is presented in Section 4.11.

4.11 Network solution methodology

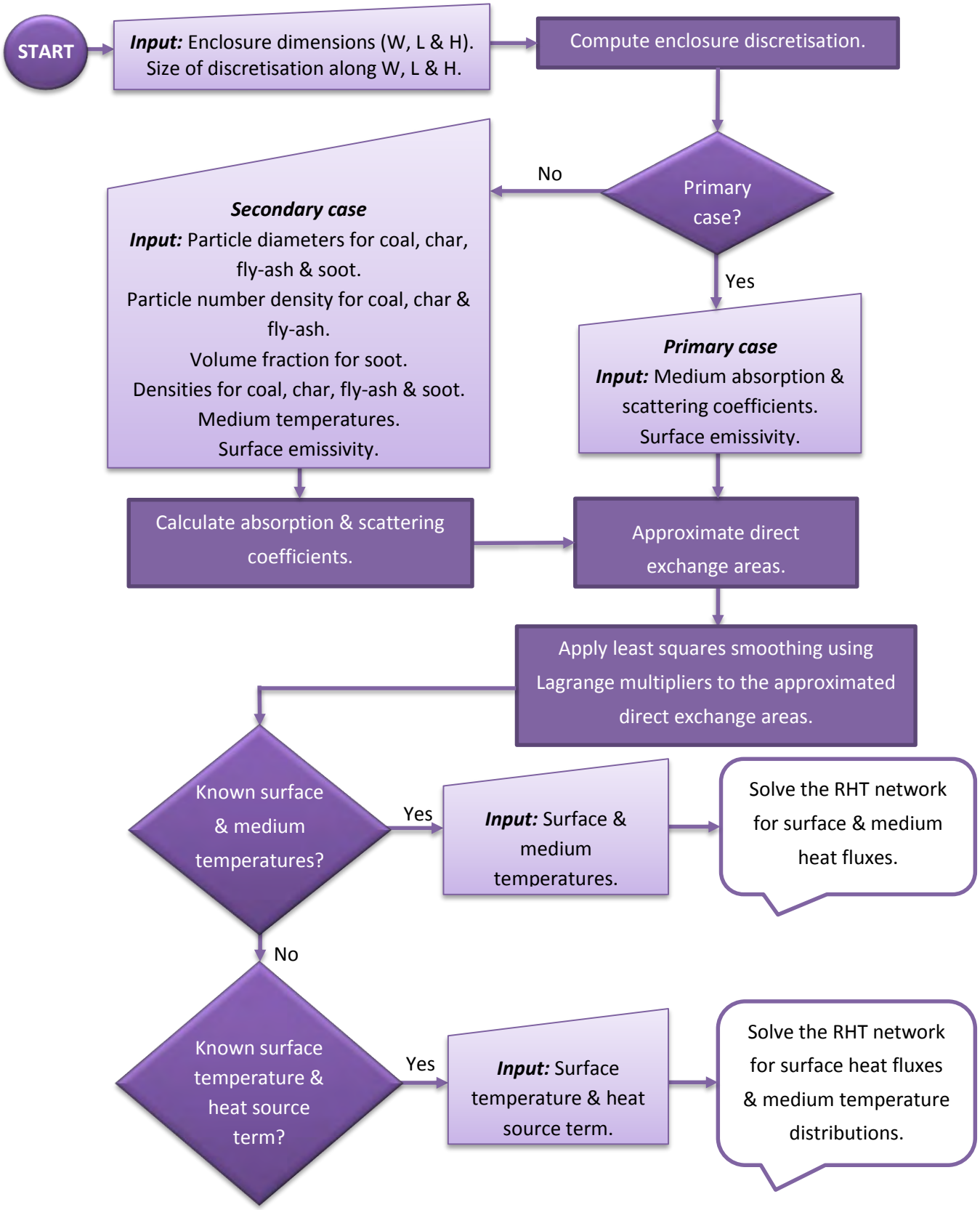

Figure 4.16. Primary model program algorithm (RHT = Radiation heat transfer).

5. Results and discussion

5.1 Introduction

The last secondary objective formulated in Chapter 1 was to conduct case studies using the radiation heat transfer network model to illustrate its applicability to boiler furnace modelling. The case studies are presented in this chapter. These case studies include the effect of slagging, flame length, a faulty burner and changes in medium radiative properties on the furnace wall heat flux distributions and furnace flue gas exit temperature distributions. These are all factors that can have a direct influence on the efficiency of coal-fired boiler furnaces. However, before moving onto the case studies, a grid independence study is conducted. A grid independence study is known to be a good indicator for establishing the reliability of numerical results (Shi & Khodadadi, 2003).

5.2 Grid independence study

The zonal method is a numerical method that requires enclosure discretisation for evaluating radiation heat transfer problems. The degree of discretisation plays an important role in the accuracy of the numerical results. Conducting a grid independence study aids in the assurance of reliable numerical results in that it enables the establishment of results that are independent of the grid size.

In this study, a grid independence study was conducted for a three-dimensional rectangular enclosure. The dimensions of the enclosure are 40 m, 20 m and 16 m along its height, length and width, respectively. The enclosure has a surface emissivity of 0.8, a surface temperature of 200 ^{o}C. It contains an absorbing participating medium with an absorption coefficient of 0.31 m^{-1} and a uniform internal heat source of 5 kW/m^3. The enclosure was discretised into different grid sizes and the grid independence study was conducted for two cases using the radiation heat transfer network model developed in this study. The first case was to study the dependence of the medium average temperature on the grid size. The second case was to study the dependence of the net radiation heat transfer rates on each surface making up the enclosure, that is, the front, rear, bottom, top, left and the right surface of the three-dimensional rectangular enclosure.

Figure 5.1 shows the first case which is the dependence of medium average temperature on grid size:

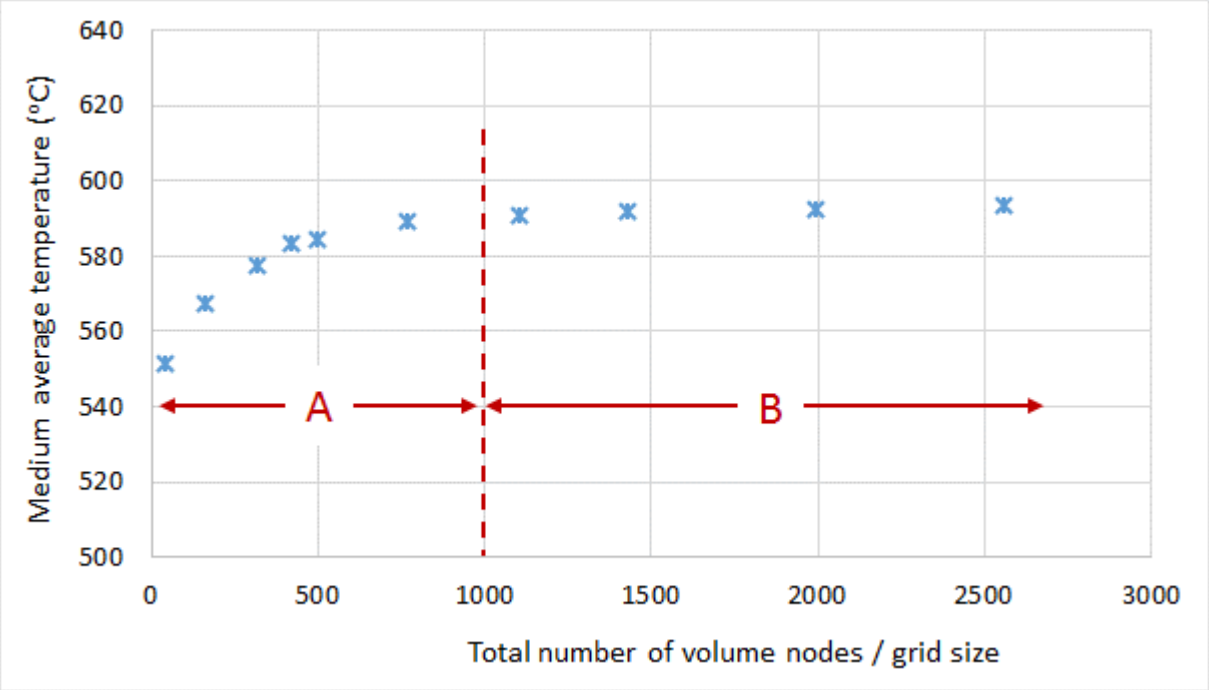

Figure 5.1. Medium average temperature at difference grid sizes.

As illustrated in Figure 5.1, the medium average temperature results vary greatly with grid size up to a total of 1000 volume nodes (stage A). At stage B, the medium average temperature results tends towards a constant value, so at stage B, the medium average temperature results are grid independent. Hence, grid independence is deemed to be achieved when the grid size exceeds 1000 nodes.

The dependence of the net radiation heat transfer rates on each surface making up the enclosure on grid size was also studied. Here, four different grid sizes were studied and they are: $(5\times2\times4)$, $(10\times4\times8)$, $(15\times6\times12)$ and $(20\times8\times16)$ along the (height$\times$length$\times$width) of the enclosure, which resulted in a total of 40, 320, 1080 and 2560 nodes, respectively. These grid sizes were chosen in order to keep a constant ratio of the number of nodes on each of the sides while rapidly increasing the total number of nodes. Figure 5.2 shows the dependence of the net radiation heat transfer rates for each surface on grid size:

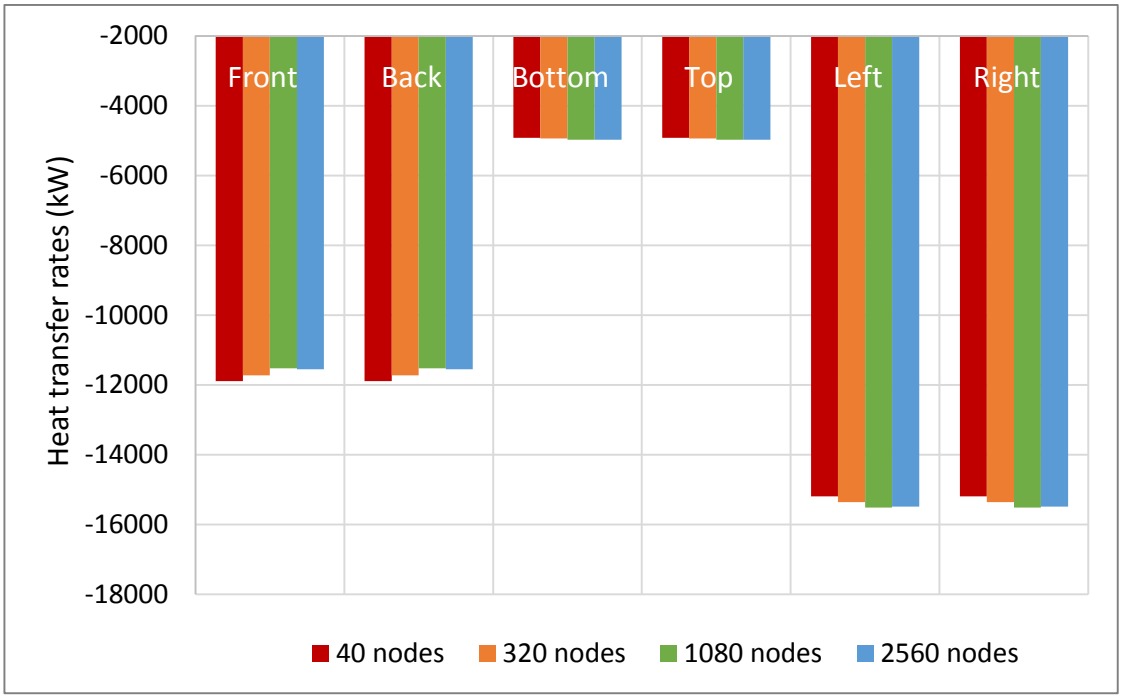

Figure 5.2. Heat transfer rates for surfaces at difference grid sizes.

Figure 5.2 again emphasise grid independence when the grid size exceeds 1000 nodes. In this case, the net radiation heat transfer rates for the surfaces are shown. The green blocks representing a grid size of 1080 nodes are identical to the blue blocks representing the 2560 nodes. This shows that grid independence is achieved.

Based on the grid independence studies conducted for medium average temperatures and net radiation heat transfer rates, great confidence was gained in using an enclosure with a grid size that exceeds 1000 nodes. As a result, the case studies that follow are conducted for an enclosure with similar dimensions, discretised into $(20\times8\times16)$ nodes along the height, width and length of the enclosure as indicated by the blue dots in Figure 5.2. However, it is worth mentioning that grid independence should be investigated for each independent case in future application of the code for other enclosure dimensions.

5.3 Case studies

The case studies conducted in this study are based on a pulverised coal-fired boiler that has a total height of 59 m, a length of 20 m and a width of 16 m. The boiler has a capacity of 400 MW. Sixteen burners are arranged in an array of four burners along the length of the boiler at four different levels along the height of the boiler on the front and rear walls of the boiler.

In other words, there are sixteen burners on the front wall and another sixteen on the rear wall of the boiler. The boiler furnace is adopted from Xu et al. (2001). An illustration of the boiler furnace is shown in Figure 5.3:

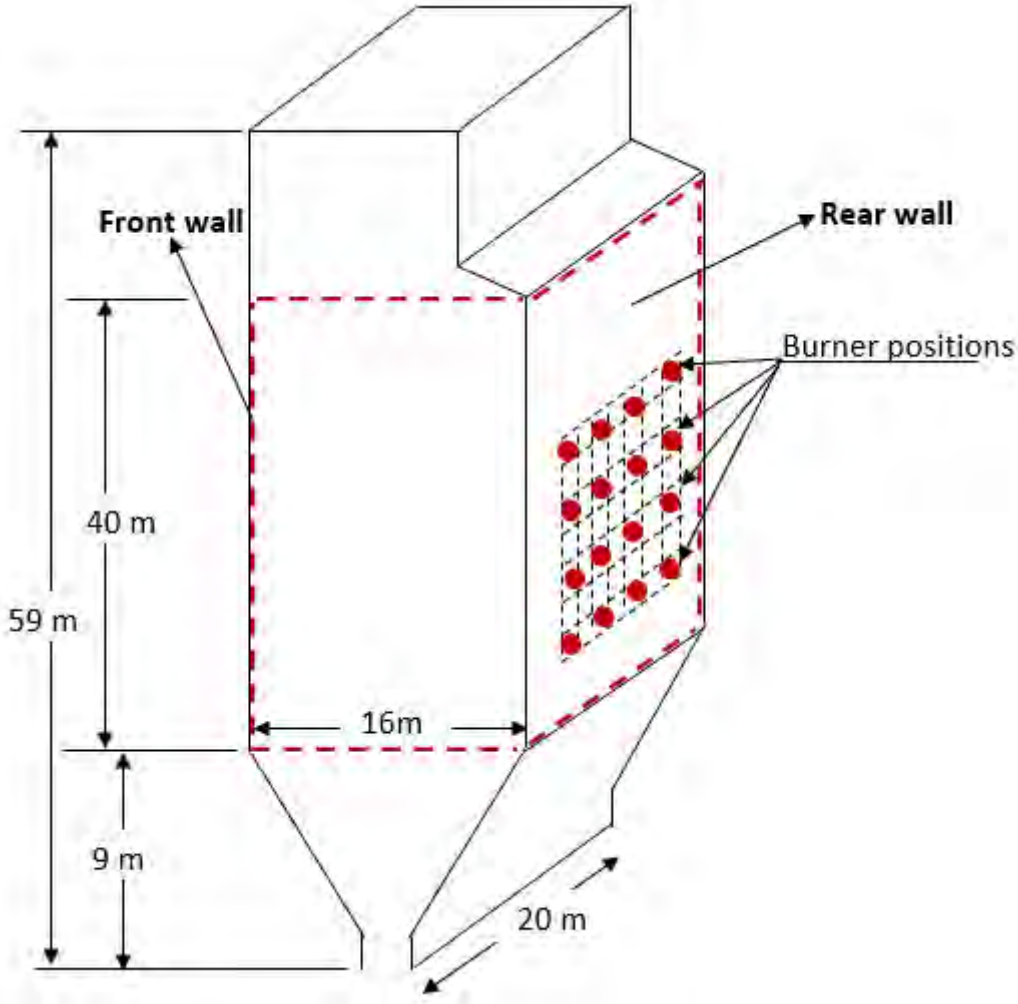

Figure 5.3. Boiler furnace geometry.

The dashed line in Figure 5.3 shows the control volume of the boiler furnace that is under consideration for the radiation heat transfer analysis. Figure 5.4 shows the boiler furnace along its length and height. It represents the front and rear walls of the boiler furnace where the burners are located.

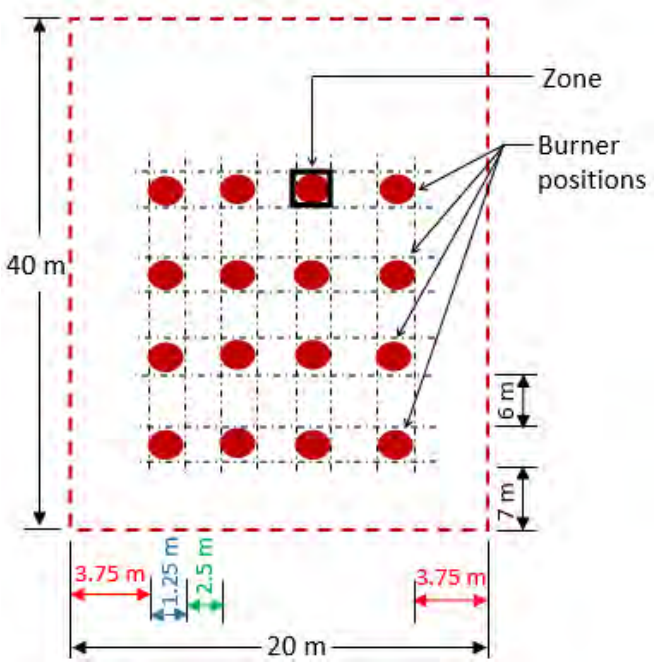

Figure 5.4. Burner positions on front and rear walls.

Each burner is specified with a heat source term of 1250 kW/m^3 and the wall temperature of the surface zones where the burners are located is 1527 ^{o}C. In other words, the heat source terms are specified inside the volume zones where the burners were located and the surface zones next to them were specified with the temperature mentioned. Each burner flame inside the boiler furnace covers a length of 4 m. The flame length is shown in Figure 5.5:

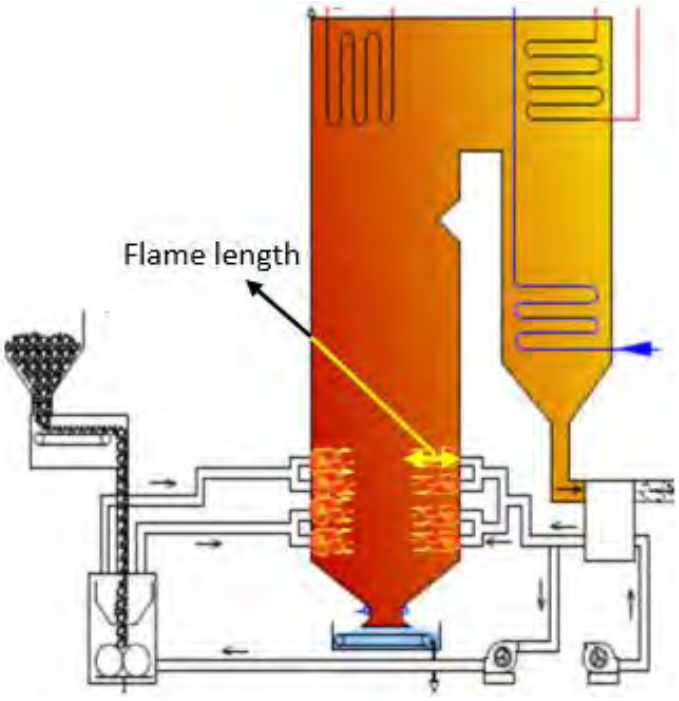

Figure 5.5: Flame length in the boiler furnace.

Additional boiler furnace wall boundary conditions are tabulated in Table 5.1:

Table 5.1. Boiler furnace wall boundary conditions (Xu, et al., 2001).

Wall	**Side walls**	**Furnace bottom wall**	**Furnace exit wall**
Emissivity	0.6	1	1
Temperature (°C)	347	77	727

The radiative properties of the coal combustion participating medium are tabulated in Table 5.2:

Table 5.2. Medium radiative properties (Fang, et al., 2010).

Absorption coefficient (m^{-1})	0.31
Scattering coefficient (m^{-1})	0.15

The information presented in Figure 5.3, Figure 5.4, Table 5.1 and Table 5.2 serve as inputs to the network model developed in this study. Furthermore, an additional input to the model is the discretisation of the boiler furnace. Based on the results of the grid independence study shown earlier, the boiler furnace was discretised into $20 \times 8 \times 16$ nodes along the height, width and length of the enclosure for all the case studies discussed below.

5.4 Case study 1: Base case conditions

The first case study was directed towards solving and showing the wall heat flux and furnace flue gas exit temperature distributions of the boiler furnace under base case conditions for the input parameters discussed in the previous section. This case study will serve as the benchmark for the case studies to follow.

Figure 5.6 shows the heat flux distributions on the left and front walls of the furnace as well as the furnace flue gas exit temperature distributions.

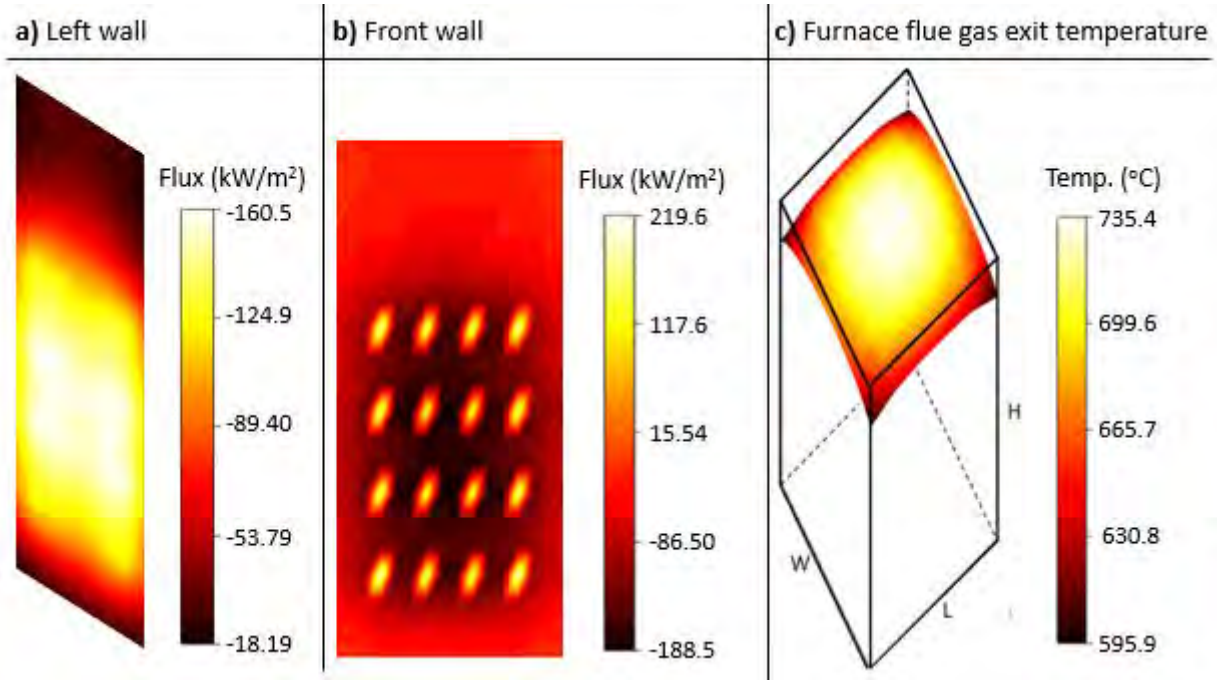

Figure 5.6. a) Left wall flux, b) Front wall flux and c) Furnace exit temperature under base case conditions.

Because of symmetry, the same heat flux distributions can be expected on the right and rear walls of the boiler furnace. Figure 5.6b shows the front wall heat flux distributions; here, the highest heat fluxes are observed where the burners are located.

The positive valued heat fluxes are due to the heat source terms of the burners and the negative valued heat fluxes are due to the heat absorption of the low temperature walls. This trend correlates with the findings of Moghari et al. (2012). Moghari et al. (2012) used the zonal method to predict thermal behaviour in a D-type water cooled steam boiler. They found a reduction in the heat flux intensity near the corners of the walls, and that the maximum heat flux was in the front and rear walls of the furnace where the burners were located (Moghari, et al., 2012).

Furthermore, Moghari et al. (2012) also reported that the heat flux is highest at the centre of the walls because the central region is positioned best to receive the most radiation from the other walls as well as the furnace medium. This is essentially also the place where the highest temperatures will be observed. A similar trend is also seen in Figure 5.6a. This figure shows the heat flux distribution on the left wall of the furnace. It is clear that the highest heat fluxes are at the centre zone of the left wall in alignment with the burner positions on the front and rear walls of the furnace.

Figure 5.6c on the other hand shows the furnace flue gas exit temperature distribution. Note that this is the medium temperature and not the furnace exit wall temperature specified as 727 ^{o}C in the wall boundary conditions (Table 5.1). Here, the highest medium temperatures are found at the centre and gradually decreases as it approaches the walls of the boiler furnace because the wall boundaries are set to fixed temperatures. The reason why the medium temperature does not decrease linearly as it approaches the walls is mainly due to the radiation heat transfer that is proportional to the fourth power of the temperatures. Furthermore, it can be seen that there is a steep decrease in temperature near the corners. This is due to the effect of the neighbouring low temperature walls enclosing the furnace (Lei, et al., 1989). Here, the highest furnace flue gas exit temperature is 735.4 ^{o}C. The temperature distribution in Figure 5.6c agrees with the findings of Hottel and Sarofim (1965). Hottel and Sarofim (1965) studied the effect of plug flow and parabolic flow patterns on gas temperature and wall heat flux distributions in cylindrical furnaces. Gas temperature distributions were found to decrease more rapidly near the walls of the furnace compared to the centre of the furnace. They also reported maximum wall heat fluxes near the burners that decreased along the height of the furnace as the gas temperature decreased (Hottel & Sarofim, 1965). Hence, highest wall heat fluxes are found at the height furnace gas temperatures.

5.5 Case study 2: The effect of slagging

Slagging is defined as the deposition of ash on the boiler walls in the radiation zone of the furnace (Borio & Levasseur, 1984) and is commonly found around the burner regions which are called eyebrows. The effect of slagging on heat flux and medium temperature distributions is investigated using the radiation heat transfer network model developed in this study. This is done by reducing the surface emissivity on a part of the front and rear walls from 0.6 (as stipulated in Table 5.1) to 0.2 at a height of 21 m just above the burners on the third level. The slagging area is shown with a white dashed area in Figure 5.7b. Figure 5.7 shows the left and front wall heat fluxes and medium temperature distributions due to slagging:

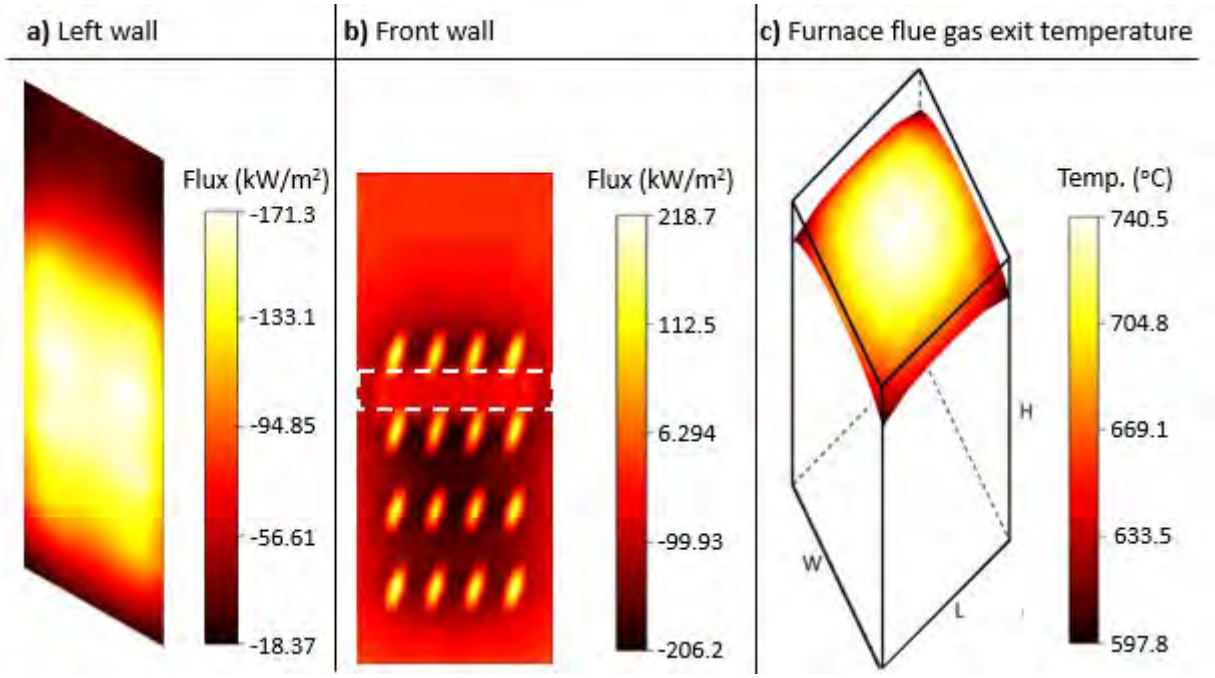

Figure 5.7. a) Left wall flux, b) Front wall flux and c) Furnace exit temperature due to slagging.

In Figure 5.7b, it can be seen that less heat was being absorbed at the area where slagging was occurring. This is a clear indication that slagging restricts wall heat absorption which in turn results in disturbed medium temperature distributions. Because less heat is being absorbed by the front and rear walls, higher furnace flue gas exit temperatures can also be expected. The slagging on the front and rear walls resulted in the increase of heat flux distributions on the left and right walls. In the base case (Figure 5.6a), the left wall had a maximum heat flux of 160.5 kW/m^2 and after slagging, the left wall heat flux increased to 171.3 kW/m^2.

As for the furnace flue gas exit temperature, there was indeed an increase in temperature. In the base case (Figure 5.6c), the highest observed exit temperature was 735.4 ^{o}C and with slagging it increased to 740.5 ^{o}C. An increase in medium temperature due to slagging can have a negative impact on the heat exchangers downstream of the furnace, which may eventually lead to unplanned downtime when an early detection is not made. Unplanned downtime is one of the factors that hinders the expectation that power plants must reliably and efficiently generate electricity. An increased furnace flue gas exit temperature also implies that more heat is carried away via the flue gas rather than being used to produce steam and can therefore imply a lower overall thermal efficiency.

Case study 3: The effect of flame length

Here, the effect of flame length is studied by spreading the burner heat source over a larger volume at the burner positions. Instead of the flame covering a length of 4 meters as stipulated for the base case, it now covers a length of 8 meters. Furthermore, because the flame length covers a larger volume, each volume zone covering the burner locations is specified with a heat source term of 625 kW/m^3 instead of 1250 kW/m^3 (as for the base case) to maintain a boiler capacity of 400 MW. Figure 5.8 shows the left and front wall heat fluxes and medium temperature distributions as a result of increased flame length:

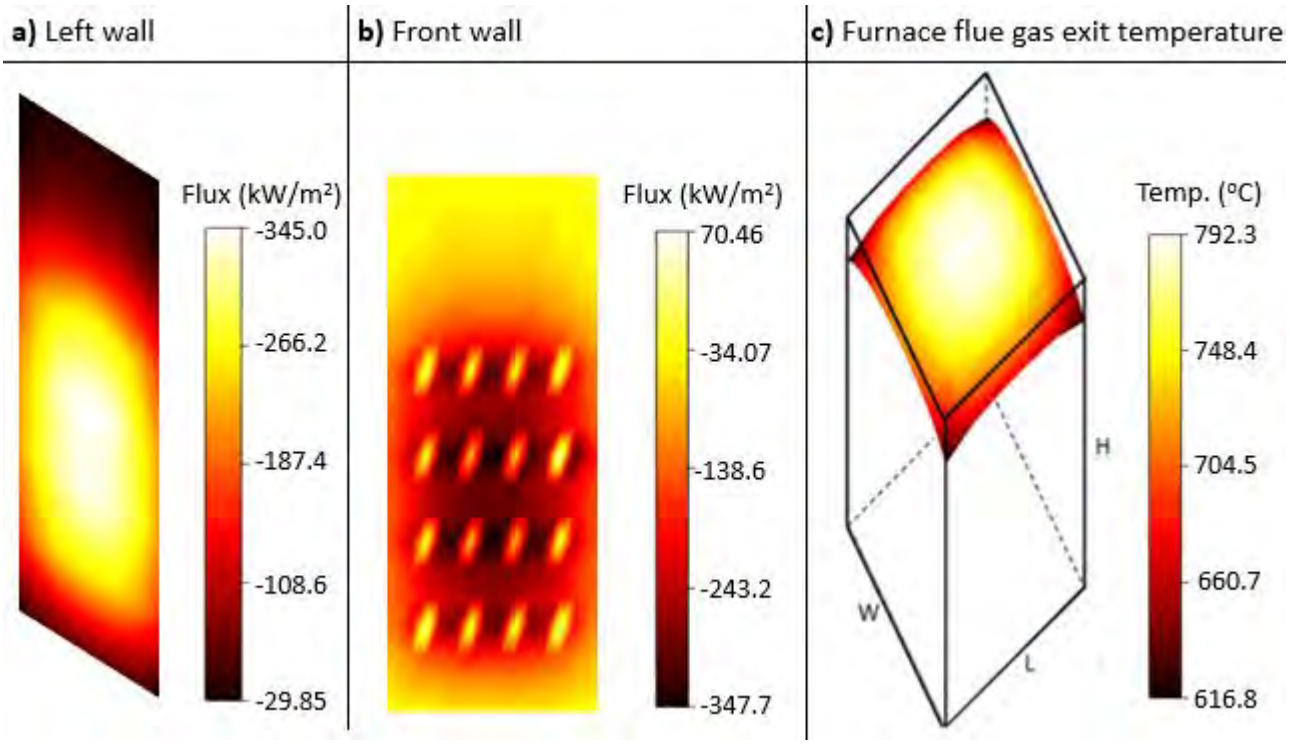

Figure 5.8. a) Left wall flux, b) Front wall flux and c) Furnace exit temperature due flame length.

Figure 5.8a and Figure 5.8b shows the left and front wall heat flux distributions, respectively. These distributions also hold for the respective opposing walls, that is, the right and rear walls. Comparing these heat flux distributions to the base case (Figure 5.6a and Figure 5.6b) it is clear that increased flame length resulted in increased heat flux distributions on the walls. In the base case (Figure 5.6a), the left wall had a maximum absorbed heat flux of 160.5 kW/m^2 and after an increased flame length, the left wall heat flux increased to 345.0 kW/m^2. Figure 5.8c shows the furnace flue gas exit temperature distribution. Comparing the flue gas exit temperature distribution to that of the base case it can be seen that a higher flame length results in a higher flue gas exit temperature

distribution. The negative effects of increased furnace flue gas exit temperatures are discussed in case study 2. It is interesting to see how lower heat source terms specified over a larger volume result in higher heat flux and furnace flue gas exit temperature distributions. This shows the importance of well-established flame lengths which are a result of burner firing configurations and combustion rates (Khan & Khan, 2014).

5.6 Case study 4: The effect of a faulty burner

All coal-fired power plants suffer component wear at some point in their lifetime. This case study aims to investigate the effect of a faulty burner on the heat flux and temperature distributions on the walls and at the exit of the boiler furnace, respectively. The fourth burner at the fourth level on the front wall is faulty and its absence can be seen in Figure 5.9b.

The left, front, right and rear wall heat flux distributions are shown in Figure 5.9:

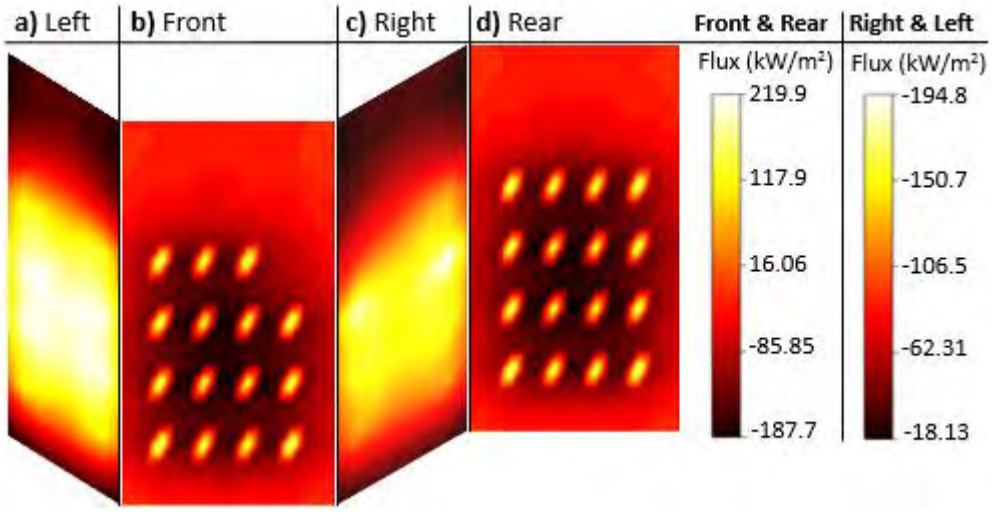

Figure 5.9. Left, front, right & rear wall fluxes.

From Figure 5.9b, it is clear that the faulty burner creates a change in the heat flux distributions of the right wall in Figure 5.9c. For base case conditions, the heat flux distributions on both the left and right walls are identical and similar to that of the left wall shown in Figure 5.9a.

The faulty burner brings about change in the wall heat flux distributions which propagates into changed furnace exit temperature distributions. Figure 5.10 shows the furnace flue gas exit temperature distribution:

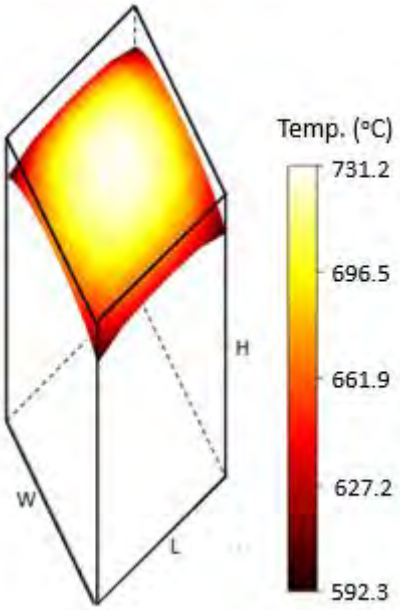

Figure 5.10. Furnace exit temperature considering a faulty burner.

Comparing the furnace flue gas exit temperature distribution in Figure 5.10 to that of the base case in Figure 5.6c, it can be seen that the faulty burner introduced reduced furnace flue gas exit temperatures. A reduction in furnace medium temperature due to the faulty burners could result in incomplete combustion. Baukal (2000) studied heat transfer in industrial combustion and reported that incomplete combustion leads to increased carbon monoxide concentrations which in turn results in reduced combustion efficiency.

5.7 Case study 5: Changes in medium radiative properties

Both medium temperature distributions and radiative properties play a vital role in any combustion process. Changes in medium radiative properties are due to changes in particle size distributions, densities, volume fractions etc. These changes are brought about by the type of coal used and the fuel/oxidiser ratio when fed to the boiler furnace. The effect of a change in medium radiative properties on furnace flue gas exit temperature and wall heat flux distributions are studied here.

This is done by increasing the absorption coefficient of the coal combustion participating medium from $0.31\ m^{-1}$ (as stipulated in Table 5.2 for the base case condition) to $1.5\ m^{-1}$, while keeping the scattering coefficient constant at $0.15\ m^{-1}$. An increase in medium absorption coefficient inherently means an increase in medium extinction coefficient because the extinction coefficient is the sum of absorption coefficient and scattering coefficient. The extinction coefficient is a measure of how easily a beam of radiation penetrates a given medium without being absorbed (Zamaniyan, et al., 2008).

Figure 5.11 illustrates the furnace exit temperature distributions at different extinction coefficients:

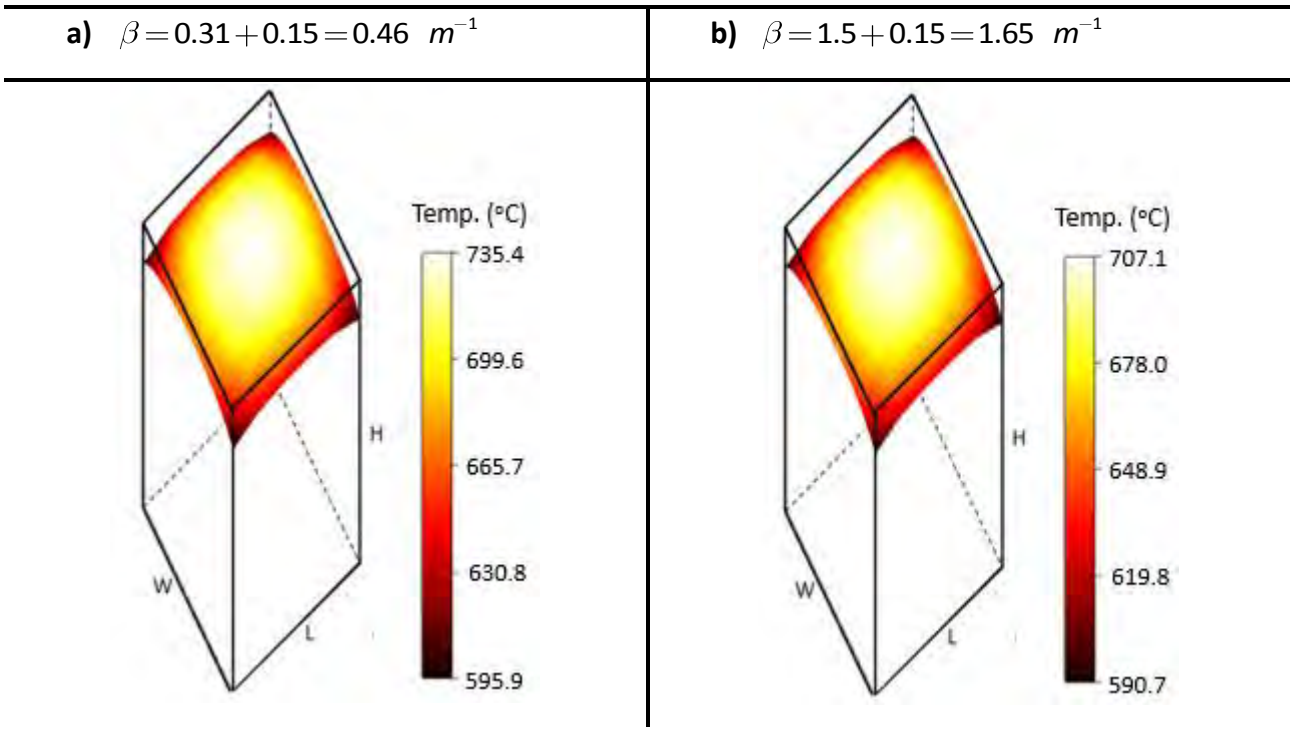

Figure 5.11. Furnace exit temperature considering changes in medium radiative properties.

Figure 5.11 shows that an increase in medium extinction coefficient results in a decrease of furnace flue gas exit temperature. This result agrees with that of Lin et al. (1998). Lin et al. (1998) modelled the radiation heat transfer of an emitting, absorbing and scattering medium using the discrete ordinate method. They studied the effect of medium extinction coefficient on medium temperature. From the study, they concluded that an increase in extinction coefficient resulted in a decrease of medium temperature (Lin, et al., 1998).

The heat flux distributions on the left and front walls are shown Figure 5.12:

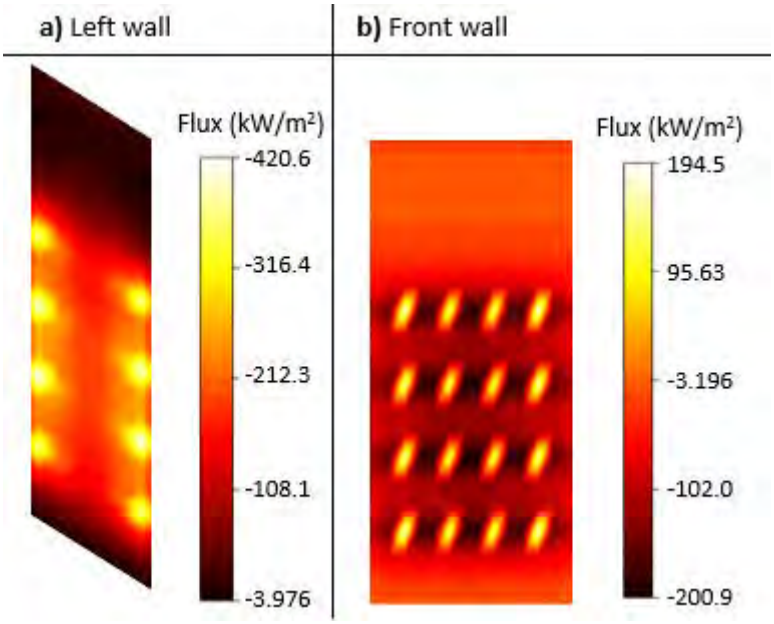

Figure 5.12. Left & rear wall fluxes.

The radiation intensity on the walls is influenced mostly by the emission of the medium near the enclosing walls as a result of the increased extinction coefficient of the medium. In other words, the volume zones around the burners absorb most of the energy which is then transfer to the neighbouring walls. This leaves less energy to be absorbed further along the length and height of the boiler away from the burners as shown in Figure 5.12. A reduction in energy absorption by the medium also means a reduction in medium temperature. Hence, there will be a decrease in medium temperature as it propagates along the height of the furnace and eventually leaves the furnace at lower temperatures.

A decrease in medium temperature due to an increase in extinction coefficient is further emphasised by Zamaniyan et al. (2008) in the figure below:

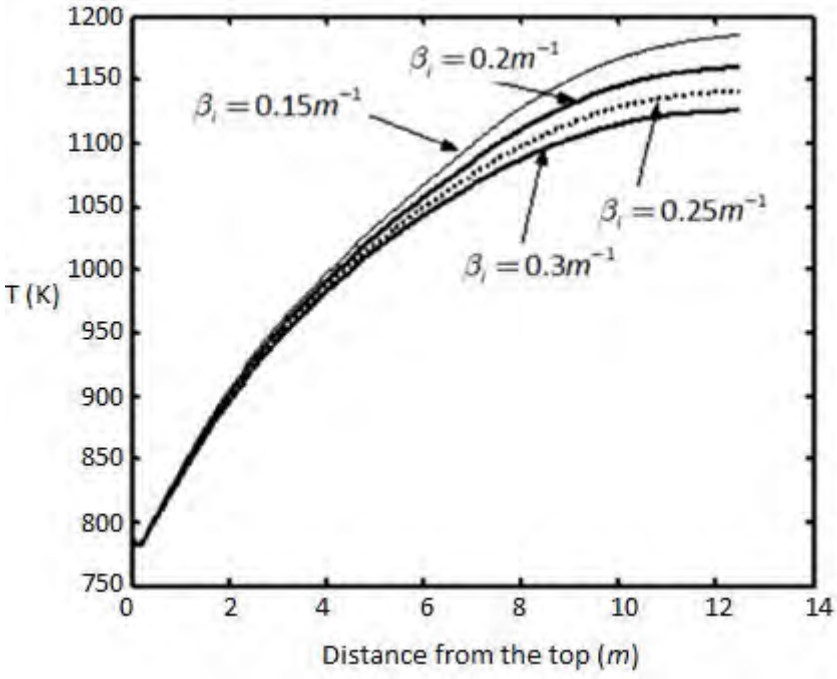

Figure 5.13. Effect of extinction coefficient on gas temperature (Zamaniyan, et al., 2008).

5.8 Closing remark

The results of all the case studies conducted above qualitatively compare well with trends available for furnace case studies reported in literature. Therefore, it can be concluded that the radiation heat transfer network solution methodology developed in this study is applicable to boiler furnace modelling.

6. Conclusions and recommendations

6.1 Conclusions

The primary objective of this study was to develop and implement a radiation heat transfer network solution methodology based on the zonal method that may be applied in boiler furnace modelling. In order to meet this objective, the study entailed:

- Doing a detailed review of literature and theoretical study of radiation heat transfer modelling using the zonal method.
- Applying discrete numerical integration for approximating direct exchange areas.
- Applying two smoothing techniques to approximated direct exchange areas (DEAs) to ensure that the DEAs satisfied reciprocity rules and energy conservation principles.
- Solving the radiation heat transfer network using the zonal method.
- Applying simplified approximations of the Mie theory and the weighted sum of gray gases model for estimating the radiative properties of coal combustion products.
- Verifying and validating the direct exchange areas and radiation heat transfer network model by means of correlations and other numerical techniques available in literature. Good agreements were found between the results of the model and the results available in literature.
- Finally, conducting case studies using the radiation network model developed to illustrate its applicability to boiler furnace modelling.

The network model in this study was developed for two input parameter cases, a primary and a secondary case. The input parameters of the radiative properties for the two cases are tabulated in Table 6.1:

Table 6.1. Table of radiative properties input parameters.

Primary case input parameters	**Secondary case input parameters**	
> Medium absorption and scattering coefficients.	> Particle diameters for coal, char, fly-ash and soot. > Particle number density for coal, char and fly-ash.	> Volume fraction for soot. > Densities for coal, char, fly-ash and soot. > medium temperatures

Furthermore, the solution of the radiation heat transfer network was implemented for an emitting-absorbing-scattering participating medium for two different scenarios, namely (*i*) solving surface and volume heat fluxes for known surface and medium temperatures, and (*ii*) solving surface heat fluxes and medium temperature distributions for known surface temperatures and volume heat source terms.

The primary case was used together with the second scenario of known surface temperatures and volume heat source terms to conduct the case studies in Chapter 5 and it was found that:

- Highest heat fluxes were observed at burner locations. Hottel and Sarofim (1965) and Moghari et al. (2012) also reported maximum heat flux on walls of the furnace where the burners were located.
- Highest heat fluxes were seen at the centre zones of the left and right walls in alignment with the burner positions on the front and rear walls of the furnace. Moghari et al. (2012) also reported maximum heat fluxes at the centre of the walls because the central region is positioned best to receive most of the radiation from the other walls as well as the furnace medium.
- Slagging restrict wall heat absorption which in turn results into higher furnace flue gas exit temperatures.
- A reduction in furnace medium temperature due to the faulty burners could result in incomplete combustion, which could lead to increased carbon monoxide concentrations, hence, reduced combustion efficiency.
- Finally, an increase in medium extinction coefficient resulted in a decrease of furnace exit temperature. This result agrees with that of Lin et al. (1998) and Zamaniyan et al. (2008).

The trends presented from the case studies correlate well with what is published in literature. This demonstrates that the zonal method gives satisfactory predictions and that the radiation heat transfer network solution model developed in this study is applicable to boiler furnace modelling.

6.2 Recommendations

It is recommended that the radiation heat transfer calculations be coupled with combustion models that will enable the prediction the volume fraction and particle size distributions of the particulate media in the coal combustion flame for the evaluation of radiative properties.

Another recommendation is that the furnace model be connected to a water wall heat exchanger model to solve for steam and wall temperatures rather than just specifying them and to integrate the model with a convective pass model that contains the superheaters.

A final recommendation is that a technique be developed whereby the size of the matrix that represents in the radiation heat transfer network can be reduced. At present the complete network contains connections between all the surfaces and all the volumes, irrespective of whether all these are actually visible to one another in terms of thermal radiation. By rearranging the matrix in a suitable way, its size could potentially be reduced significantly, thereby reducing the computational time and resources required.

7. List of References

Ameri, M. & Shamshirgaran, S., 2008. A case study: The effects of the design factors on the thermal profile of Shahid Rajaiee boiler. *Applied Thermal Engineering,* Volume 28, p. 955–961.

Bahador, M. & Sundén, B., 2008. Investigation on the effects of fly ash particles on the thermal radiation in biomass fired boilers. *International Journal of Heat and Mass Transfer,* Volume 51, pp. 2411-2417.

Batu, A. & Selcuk, N., 2002. Modeling of Radiative Heat Transfer in the Freeboard of a Fluidized Bed Combustor Using the Zone Method of Analysis. *Turkish Journal of Engineering & Environmental Science,* Volume 26, pp. 49- 58.

Baukal, C. E., 2000. *Heat transfer in industrial combustion.* New York: CRC Press.

Blokh, A. G., 1988. *Heat transfer in steam boiler furnaces.* Washington: Hemisphere publishing corporation.

Bordbar, M. H. & Hyppänen, T., 2007. Modeling of Radiation Heat Transfer in a Boiler Furnace. *Advanced Studies of Theoretical Physics,* 12(1), pp. 571-584.

Borio, R. & Levasseur, A., 1984. Overview of coal ash depositionin boilers. *Combustion engineering,* pp. 193-203.

Borjini, M. N., Farhat, H. & Radhouani, M., 2003. Analysis of radiative heat transfer in a partitioned idealized furnace. *Numerical Heat Transfer,* Volume 44, pp. 199-218.

Boutoub, A., Benticha, H. & Sassi, M., 2006. Non-gray Radiation Analysis in Participating Media with the Finite Volume Method. *Turkish Journal of Engineering and Environmental Science,* Volume 30, p. 183–192.

Caliot, C., Eymet, V., Eihafi, M., Le Maoult, Y. & Flamant, G., 2008. Parametric study of radiative heat transfer in participating gas–solid flows. *International Journal of Thermal Sciences,* Volume 47, pp. 1413-1421.

Carvalho, M. G. & Farias, T. L., 1998. Modelling of Heat Transfer in Radiating and Combusting Systems. *Institution of Chemical Engineers,* Volume 76, pp. 175-184.

Chai, J. C., Lee, H. S. & Patankar, S. V., 1994. Finite Volume Method for radiation heat transfer. *Journal of thermophysics and heat transfer,* 8(3), pp. 419-425.

Clark, J. A. & Korybalski, M. E., 1974. Algebraic methods for the calculation of radiation exchange in an enclosure. *Journal of heat and mass transfer,* Volume 7, pp. 3-44.

Coelho, P. J., 2002. Numerical simulation of radiative heat transfer from non-gray gases in three-dimensional enclosures, *Journal of Quantitative Spectroscopy and Radiative Transfer*, Volume 74, pp. 307–328.

Coppalle, A. & Venisch, P., 1983. The total emissivities of high temperature flames. *Combustion and Flame ,* Volume 49, pp. 101-108.

Crnomarkovic, N., Siljercic, M., Belosevic, S., Tucakovic, D. & Zivanovic, T., 2008. Modelling of radiative heat transfer inside the pulverized coal fired furnace of power plant. *Conference paper,* pp. 1-10.

Crnomarkovic, N., Siljercic, M., Belosevic, S., Stankovic, B., Tucakovic, D., & Zivanovic, T., 2012. Influence of forward scattering on prediction of temperature and radiation fields inside the pulverized coal furnace. *Energy,* Volume 45, pp. 160-168.

Crnomarkovic, N., Siljercic, M., Belosevic, S., Tucakovic, D. & Zivanovic, T., 2013. Numerical investigation of processes in the lignite-fired furnace when simple grey gas and weighted gas models are used. *International Journal of Heat and Mass Transfer,* Volume 56, pp. 197-205.

Cui, M., Chen, H. & Gao, X., 2010. Mathematical model developed by zone method considering non-gray radiation properties of gas in combustion chamber. *Journal of iron and steel ,* 17(11), pp. 13-18.

de Groot, R. A. F., van der Veen, V.G. & Sebitosi, A.B., 2013. Comparing solar PV (photovoltaic) with coal-fired electricity production in the centralized network of South Africa. *Energy*, Volume 55, pp 823-837.

Ebrahimi, H., Zamaniyan, A., Mohammadzadeh, J. S. S. & Khalili, A. A., 2013. Zonal modelling of radiative heat transfer in industrial furnaces using simplified model for exchange area calculation. *Applied Mathematical Modelling,* pp. 1-12.

Ebrahimi, H., Zamaniyan, A. & Zadeh, J. S. M., 2004. Three Dimensional Modeling of Radiative Heat Transfer in Furnaces. *9th Iranian Chemical Engineering Congress,* pp. 2609-2619.

Fang, Q., Wang, H., Wei, Y., Lei, L., Duan, X. & Zhou, H., 2010. Numerical simulations of the slagging characteristics in a down-fired, pulverized-coal boiler furnace. *Fuel Processing Technology,* Volume 91, p. 88–96.

Farias, T. L. & Carvalho, M., 1998. Radiative heat transfer in soot-containing combustion systems with aggregation. *International Journal of Heat Transfer,* 41(17), pp. 2581-2587.

Gharehkhani, S., Nouri-Borujerdi, A., Kazi, S. & Yarmand, H., 2014. Extension of Weighted Sum of Gray Gas Data to Mathematical Simulation of Radiative Heat Transferin a Boiler with Gas-Soot Media. *The Scientific World Journal,* pp. 1-9.

Gray, W. A. & Müller, R., 1974. *Engineering calculations in radiative heat transfer.* 13th ed. New York: Pergamon Press.

Holkar, R. & Hebbal, O., 2013. CFD Anlysis of Pulverised-Coal Combustion of Burner Used In Furnace with Different Radiation Models. *Journal of Mechanical and Civil Engineering,* 5(2), pp. 25-34.

Hottel, H. C. & Cohen, E. S., 1958. Radiant heat ex-change in a gas-filled enclosure: allowance for non-uniformity of gas temperature. *AIChE Journal,* Volume 4, pp. 3-14.

Hottel, H. C. & Sarofim, A. F., 1965. The effect of gas flow patterns on radiative transfer in cylindrical furnaces. *International journal of heat and mass transfer,* Volume 8, pp. 1153-1169.

Hottel, H. & Sarofim, A., 1967. *Radiative transfer.* New York: McGraw-Hill.

Hua, Y., Flamant, G., Lu, J. & Gauthier, D., 2005. 3D modelling of radiative heat transfer in circulating fluidized bed combustors: influence of the particulate composition. *International Journal of Heat and Mass Transfer,* Volume 48, p. 1145–1154.

IEA, 2014. International Energy Agency. [Online] Available at: *http://www.iea.org/publications/freepublications/publication/keyworld2014.pdf*.

Incropera, F., DeWitt, D. P., Bergman, T. L. & Lavine, A. S., 2007. *Fundamentals of Heat and Mass Transfer.* 6th ed. USA: John Wiley & Sons.

Jones, H., 2000. *Radiation heat transfer.* New York: Oxford university press Inc.

Khan, S. & Khan, S. 2014. Boiler and Its Tangential Fuel Firing System. *International Journal of Automation and Control Engineering*, 3(3), pp 71-84.

Khan, Y. U., Lawson, D. A. & Tucker, R. J., 1997. Banded radiative heat transfer analysis.. *Communications in numerical methods in engineering,* Volume 13, pp. 803-813.

Kim, C. & Lior, N., 1995. Easily computable good approximations for spectral radiative properties of particle-gas components and mixture in pulverized coal combustors. *Fuel,* 74(12), pp. 1891-1902.

Kim, C. & Lior, N., 1998. A numerical analysis of NOx formation and control in radiatively/conductively-stabilized pulverized coal combustors. *Chemical Engineering Journal,* Volume 71, pp. 221-231.

Kitto, J.B & Stultz, S.C. 2005. *Steam its generation and use*. 41ed. United stated of America: The Babcock & Wilcox Company.

Kumar, S. 2011. Analysis of radiative heat transfer in an absorbing-emitting-scattering medium using fluent. *National Institute of Technology*, pp 1-90.

Lallemant, N., Sayret, A. & Weber, R., 1996. Evaluation of emissivity correlations for H_2O-CO_2-N_2/air mixtures and coupling with solution methods of the radiative transfer equation. *Progress in Energy and Combustion Science,* Volume 22, pp. 543-574.

Lari, K. & Nassab, S. A., 2011. Analysis of combined radiative and conductive heat transfer in three-dimensional complex geometries using blocked-off method. *Transactions of Mechanical Engineering,* Volume 35, pp. 107-119.

Larsen, M. E. & Howell, J. R., 1986. Least-squares smoothing of direct exchange areas in zonal analysis. *Journal of Heat Transfer,* Volume 108, pp. 239-242.

Lawson, D., 1995. An improved method for smoothing approximate exchange areas. *International Journal of Heat Transfer,* 38(16), pp. 3109-3110.

Lawson, D. A., 1995. An improved method for smoothing approximate exchange areas. *International Journal of Heat Transfer,* 38(16), pp. 3109-3110.

Lawson, D. A., 1996. An accurate program for radiation modelling in the design of high-temperature furnaces. *Journal of Mathematics Applied in Business & Industry,* Volume 7, pp. 109-116.

Lei, Y., Zhongyuan, Y., Ming, L., Pengfei, L.U. & Junjie, L., 1989. Numerical simulation of radiative heat transfer in cylindrical enclosure. *Chinese scientific papers online,* pp. 1-9.

Lin, W., Mo, X. & En, H., 1998. Three dimensional radiation in absorbing-emitting-scattering medium using the discrete ordinates medium. *Journal of thermal science,* 7(4), pp. 255-263.

Liu, F., Becker, H. A. & Bindar, Y., 1998. A comparative study of radiative heat transfer modelling in Gas-fired furnaces using the simple gray gas and the weighted Sum of gray gases models. *International Journal of Heat and Mass Transfer,* Volume 41, pp. 3357-3371.

Liu, H., Liu, Y., Yi, G., Nie, L. & Che, D., 2013. Effects of Air Staging Conditions on the Combustion and NOx Emission Characteristics in a 600 MW Wall Fired Utility Boiler Using Lean Coal. *Energy & Fuels,* Volume 27, pp. 5831-5840.

Li, W., Lou, C., Sun, Y. & Zhou, H., 2011. Estimation of radiative properties and temperature distributions in coal-fired boiler furnaces by a portable image processing system. *Experimental Thermal and Fluid Science,* Volume 35, pp. 416-421.

Lou, C., Zhou, H., Yu, P. & Jiang, Z., 2007. Measurements of the flame emissivity and radiative properties of particulate medium in pulverized-coal-fired boiler furnaces by image processing of visible radiation. *Proceedings of the Combustion Institute,* Volume 31, pp. 2771-2778.

Mahamud, R., Khan, M., Rasul, M. & Leinster, M., 2013. Exergy Analysis and Efficiency Improvement of a coal Fired Thermal Power Plant in Queensland. In: *Thermal Power Plants - Advanced Applications.* Queensland: Intech.

Martins, G., Hernandez, O. & Bandarra, E., 2012. Zonal method implementation to determine the thermal radiation heat transfer in bi-dimensional furnaces. *14th Brazilian Congress of Thermal Sciences and Engineering,* pp. 18-22.

Méchi, R., Farhat, H., Guedri, K., Halouani, K. & Said, R., 2010. Extension of the zonal method to inhomogeneous non-grey semi-transparent medium. *Energy,* Volume 36, pp. 1-15.

Méchi, R., Farhat, H. & Saïd, R., 2007. Improved Zonal Method Predictions in a Rectangular Furnace by Smoothing the Exchange Areas. *Turkish Journal of Engineering & Environmental Science,* Volume 31, pp. 333-343.

Mengüc, M. P. & Viskanta, R., 1985. Radiative transfer in three-dimensional rectangular enclosures containing inhomogeneous, anisotropically scattering media. *Journal of Quantum Spectroscopy and Radiative Transfer,* 33(6), pp. 533-549.

Modest, M. F., 2013. *Radiative heat transfer.* 3rd ed. New York: Elsevier.

Moghari, M., Hosseini, S., Shokouhmand, H., Sharifi, H. & Izadpanah, S., 2012. A numerical study on thermal behavior of a D-type water-cooled steam boiler. *Applied Thermal Engineering,* Volume 37, pp. 360-372.

Palmqvist, O., 2012. *Dynamic modelling of heat transfer processes in a supercritical steam power plant- Master's Thesis.* Sweden: Chalmers University of Technology.

Perry, R. H., Green, D. W. & Maloney, J. O., 1997. *Perry's Chemical Engineers' Handbook.* 7th ed. New York: McGraw-Hill.

Shi, X. & Khodadadi, J., 2003. Laminar Natural Convection Heat Transfer in a Differentially Heated Square Cavity Due to a Thin Fin on the Hot Wall. *Journal of Heat Transfer,* Volume 125, pp. 624-634.

Siegel, R. & Howell, J. R., 1972. *Thermal radiation heat transfer.* New York: McGraw Hill.

Smith, T., Shen, Z. & Friedman, J., 1982. Evaluation of Coefficients for the Weighted Sum of Gray Gases Model. *Journal of Heat Transfer,* Volume 104, pp. 602-608.

Smoot, L. & Pratt, D., 1979. *Pulverized-coal combustion and gasification: Theory and applications for continuous flow processes.* New York: Plenum Press.

Teir, S. & Jokivuori, A., 2002. Heat Exchangers in Boilers. *Energy Engineering and Environmental Protection Publications,* pp. 1-14.

Tian, W. & Chiu, W. K., 2003. Calculation of Direct Exchange Areas for Non-uniform Zones Using a Reduced Integration Scheme. *Journal of Heat Transfer,* Volume 125, pp. 839-844.

Trivic, D., 2014. 3-D radiation modeling of nongray gases–particles mixture by two different numerical methods. *International Journal of Heat and Mass Transfer,* Volume 70, p. 298–312.

Tucker, R. J., 1986. Direct Exchange Areas for Calculating Radiation Transfer in Rectangular Furnaces. *Journal of Heat Transfer,* Volume 108, pp. 707-710.

Van de Hulst, H., 1957. *Light scattering by small particles.* New york: John Wiley & Sons, Inc.

Viskanta, R. & Mengüc, M. P., 1987. Radiation Heat Transfer in Combustion Systems.. *Program in Energy Combustion Science,* Volume 13, pp. 97-160.

Wahlberg, T., 2011. *Modeling of Heat Transfer- Master Thesis Project,* Sweden: Mälardalen university of Sweden.

WCA, 2014. *World Coal Association.* [Online] Available at: http://www.worldcoal.org/resources/coal-statistics/

WNA, 2015. *World Nuclear Association.* [Online] Available at: http://www.world-nuclear.org/info/Energy-and-Environment/-Clean-Coal--Technologies/

Xu, M., Azevedo, J. & Carvalho, M., 2001. Modeling a front wall fired utility boiler for different operating conditions. *Computerl methods in applied mechanics and engineering,* Volume 190, pp. 3581-3590.

Yin, Z. & Jaluria, Y., 1997. Zonal method to Model Radiative Transport in an Optical Fiber Drawing Furnace. *Journal of Heat transfer,* Volume 119, pp. 597-603.

Yoon, K., H., C. & Kim, T., 2010. Study on the radiative transfer through non-grey gas mixtures within an irregular 3-D enclosure by using the modified weighted sum of grey gas method. *Journal of Mechanical Science and Technology,* 24(7), pp. 1531-1536.

Yu, M., Baek, S. & Park, J., 2000. An extension of the weighted sum of gray gases non-gray gas radiation model to a two phase mixture of non-gray gas with particles. *International Journal of Heat and Mass Transfer,* Volume 43, pp. 1699-1713.

Zamaniyan, A., Ebrahimi, H., S, J. & Mohammadzadeh, J. S. S., 2008. A unified model for top fired methane steam reformers using three-dimensional zonal analysis. *Chemical Engineering and Processing,* Volume 47, p. 946–956.

Appendix A. Basic terms and definitions

Absorption coefficient	The amount of absorption of thermal radiation per unit path length within the medium (Siegel & Howell, 1972).
Absorption efficiency factor, Q_{abs}	The ratio of energy absorbed by the particle to the total energy in the incident beam (Farias & Carvalho, 1998).
Blackbody	An idealised object in that it absorbs all radiation that is incident upon it and emits the maximum possible amount of thermal radiation (Incropera, et al., 2007).
Complex index for refraction, m	It characterises the interaction of electromagnetic radiation with the medium (Kitto & Stultz, 2005).
Diffuse surface	Reflection of radiation is in all directions (Gray & Müller, 1974).
Direct exchange areas	They give a measure of the amount of radiation emitted by one zone which is directly intercepted by another, taking into account the radiative properties of the medium between the zones (Hottel & Sarofim, 1967).
Extinction coefficient, m^{-1}	A measure of how easily a ray of radiation penetrates a given medium without being absorbed, in other words, it represents energy loss due to the medium (Zamaniyan, et al., 2008).
Gray medium	Medium with radiative properties that are independent of wavelength (Crnomarkovic, et al., 2012).
Irradiation, H	The rate at which radiation is incident on an object from all directions per unit area (Incropera, et al., 2007).
Isotropically scattering	Scattering that is equal in all directions (Siegel & Howell, 1972).
Non-gray medium	Medium with radiative properties that are dependent on wavelength (Crnomarkovic, et al., 2012).
Opaque	No transmission through the surface (Siegel & Howell, 1972).
Participating media	Medium that is not transparent to radiation but rather absorbs some of the radiation passing through it.
Radiation heat transfer	Also referred to as thermal radiation, is the transport of energy by electromagnetic waves, and electromagnetic waves are characterised by their wavelength (Incropera, et al., 2007).
Radiosity, J_{si}	The rate at which radiation leaves the surface zone per unit area (Incropera, et al., 2007).
Scattering albedo, ω	The fraction of energy in the total extinction, β which is scattered after the interaction with the particle (Kitto & Stultz, 2005).

Scattering coefficient	Describes the amount of scattering of thermal radiation per unit path length for propagation in the medium (Siegel & Howell, 1972).
Scattering efficiency factor, Q_{sca}	The ratio of energy scattered by the particle to the total energy in the incident beam (Farias & Carvalho, 1998).
Total exchange areas	They give a measure of the amount of radiation emitted by one zone which is absorbed by another, taking into account the direct exchange areas and surface emissivities (Hottel & Sarofim, 1967).
View factor, F_{ij}	The fraction of the radiation leaving surface *i* that is intercepted by surface *j* (Incropera, et al., 2007).

Appendix B. Model and mathematical derivations

B. 1 Enclosure discretisation

An enclosure consisting of six sides (FRONT, BACK, BOTTOM, TOP, LEFT and RIGHT) is shown below:

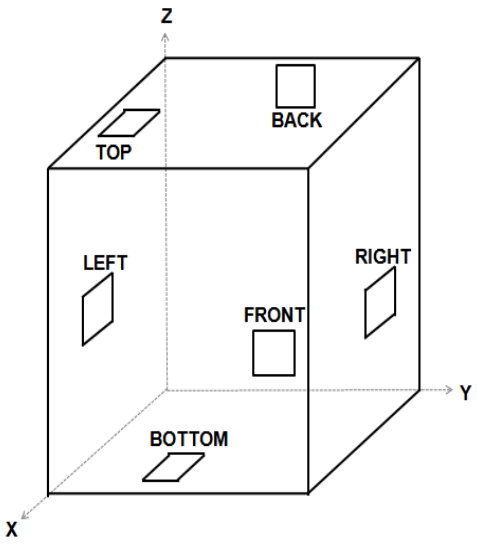

Figure 7.1. Furnace enclosure sides.

Each of these sides can be divided into a finite number of increments which result in a finite number of surface areas. Along the length, width and height of the enclosure, the number of increments are represented by *m*, *n* and *o* respectively. This also leads to the volume of the enclosure being divided into a finite number of volume zones. The table below summarises the parameters used in the direct exchange area calculations:

Table 7.1. Surface parameters.

SURFACES	AREA (Large)	AREA (Small)	NODES	NORMALS	DIMENSIONS
FRONT	$L \cdot H$	$[(L/m)\cdot(H/o)]$	$m \cdot o$	$[1 \quad 0 \quad 0]$	$W = W$
BACK	$L \cdot H$	$[(L/m)\cdot(H/o)]$	$m \cdot o$	$[-1 \quad 0 \quad 0]$	$W = 0$
BOTTOM	$W \cdot L$	$[(W/n)\cdot(L/m)]$	$n \cdot m$	$[0 \quad 0 \quad -1]$	$H = 0$
TOP	$W \cdot L$	$[(W/n)\cdot(L/m)]$	$n \cdot m$	$[0 \quad 0 \quad 1]$	$H = H$
LEFT	$W \cdot H$	$[(W/n)\cdot(H/o)]$	$n \cdot o$	$[0 \quad -1 \quad 0]$	$L = 0$
RIGHT	$W \cdot H$	$[(W/n)\cdot(H/o)]$	$n \cdot o$	$[0 \quad 1 \quad 0]$	$L = L$

B. 2 Direct exchange area approximations

The surface-to-volume and volume-to-volume direct exchange areas were approximated using Equation (7.1) and (7.2) as elaborated in Chapter 4.4 for the surface-to-surface direct exchange areas. The surface-to-volume direct exchange areas are obtained from:

$$\overline{s_i g_j} = \sum_{i=1}^{N_s}\sum_{j=1}^{N_g} \exp(-\beta|R|) \frac{\beta \cdot \dfrac{n_j \cdot R}{|n_j||R|} \Delta A_i \Delta V_j}{\pi |R|^2} \tag{7.1}$$

The volume-to-volume direct exchange areas are obtained from:

$$\overline{g_i g_j} = \sum_{i=1}^{N_g}\sum_{j=1}^{N_g} \exp(-\beta|R|) \frac{\beta \cdot \beta \cdot \Delta V_i \Delta V_j}{\pi |R|^2} \tag{7.2}$$

B. 3 Zonal method

In the presence of an emitting-absorbing-scattering medium, the net heat flux leaving a surface and volume zone is calculated from the difference between the emitted radiation and the absorbed irradiation as:

$$q_{si} = \frac{1}{A_i}(\varepsilon_i A_i E_{bsi} - h_{si}) = \frac{1}{A_i}(\varepsilon_i A_i E_{bsi} - \varepsilon_i A_i H_{si}) \tag{7.3}$$

and

$$q_{gi} = \frac{1}{A_i}(4\kappa_i V_i E_{bgi} - h_{gi}) = \frac{1}{A_i}(4\kappa_i V_i E_{bgi} - \kappa_i V_i H_{gi}) \tag{7.4}$$

As a result, the radiation heat transfer on a surface and volume zone respectively is:

$$Q_{si} = \varepsilon_i A_i E_{bsi} - h_{si} \tag{7.5}$$

and

$$Q_{gi} = 4\kappa_i V_i E_{bgi} - h_{gi} \tag{7.6}$$

<u>Radiation heat transfer in emitting-absorbing media with or without isotropic scattering</u>

An energy balance in terms of radiation heat flux on a surface zone is given as:

$$\begin{aligned} q_i &= q_{out} - q_{in} \\ &= (q_{emission} + q_{reflection}) - q_{irradiation} \\ &= (\varepsilon E_{bsi} + \rho_s H_{si}) - H_{si} \qquad for \quad J_{si} = \varepsilon E_{bsi} + \rho_s H_{si} \\ &= J_{si} - H_{si} \end{aligned} \tag{7.7}$$

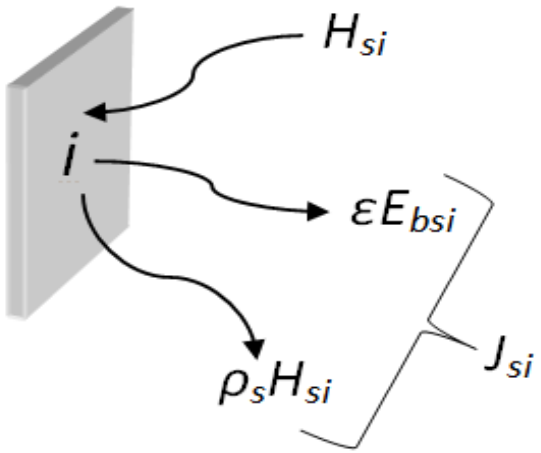

Figure 7.2. Energy balance on surface zone.

By multiplying the radiation heat flux with area, the radiation heat transfer can be calculated as seen in Equation (7.8):

$$\begin{aligned} Q_{si} &= A_i q_i = A_i (J_{si} - H_{si}) \\ &= A_i \varepsilon_i (E_{bsi} - H_{si}) \quad with \quad A_i = \sum_{j=1}^{N} \overline{s_i s_j} + \sum_{k=1}^{K} \overline{s_i g_k} \\ &= \sum_{j=1}^{N} \overline{s_i s_j} (J_{si} - J_{sj}) + \sum_{k=1}^{K} \overline{s_i g_k} (J_{si} - J_{gk}) \\ &= \varepsilon_i \left(A_i E_{bsi} - \sum_{j=1}^{N} \overline{s_i s_j} J_{sj} - \sum_{k=1}^{K} \overline{s_i g_k} J_{gk} \right), i = 1,2,\ldots,N \end{aligned} \tag{7.8}$$

Energy balance in terms of radiation heat flux on a volume zone:

$$\begin{aligned} q_i &= q_{out} - q_{in} \\ &= (q_{emission} + q_{scattering}) - q_{irradiation} \\ &= \left(4\frac{\kappa}{\beta} E_{bgi} + \frac{\sigma_s}{\beta} H_{gi} \right) - H_{gi} \quad for \quad J_{gi} = 4\frac{\kappa}{\beta} E_{bgi} + \frac{\sigma_s}{\beta} H_{gi} = 4(1-\omega) E_{bgi} + \omega H_{gi} \\ &= J_{gi} - H_{gi} \end{aligned} \tag{7.9}$$

Here, $\frac{\sigma_s}{\beta}$ is the scattering albedo also denoted by ω and $\frac{\kappa}{\beta} = 1 - \omega$.

It can be seen that an energy balance on a volume zone consist of the incident energy, H_{gi} called irradiation as well as the outgoing energy which is due to isotropic emission, $4\frac{\kappa}{\beta} E_{bgk}$ and isotropic out-scattering, $\frac{\sigma_s}{\beta} H_{gk}$. Equation (7.9) is illustrated in Figure 7.3 as:

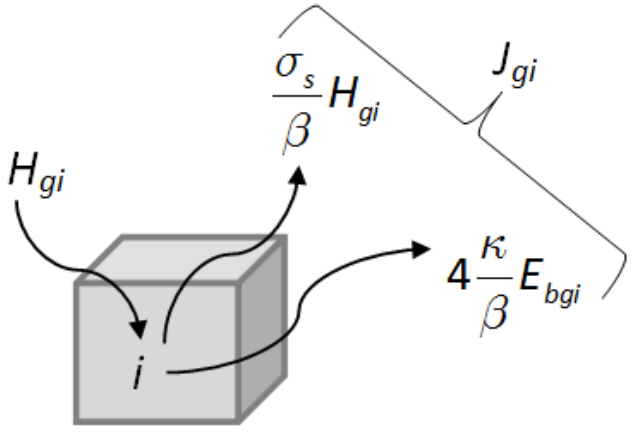

Figure 7.3. Energy balance on volume zone.

By multiplying the radiation heat flux with βV , the radiation heat transfer can be calculated as seen in Equation (7.9):

$$\begin{aligned} Q_{gi} &= \beta_i V_i \, \mathrm{q}_i = \beta_i V_i (J_{gi} - H_{gi}) \\ &= \beta_i V_i J_{gi} - \beta_i V H_{gi} \qquad with \quad \beta_i V_i = \sum_{j=1}^{N} \overline{g_i s_j} + \sum_{k=1}^{K} \overline{g_i g_k} \\ &= \sum_{j=1}^{N} \overline{g_i s_j} (J_{gi} - J_{sj}) + \sum_{k=1}^{K} \overline{g_i g_k} (J_{gi} - J_{gk}) \\ &= 4\kappa_i V_i E_{bgi} - (1-\omega_i) \left(\sum_{j=1}^{N} \overline{g_i s_j} J_{sj} - \sum_{k=1}^{K} \overline{g_i g_k} J_{gk} \right), i = 1,2,\ldots,\mathrm{K} \end{aligned} \tag{7.10}$$

A detailed derivative of Equation (7.10) is as follow:

$$Q_{gi} = \beta_i V_i \;\; J_{gi} - H_{gi} \qquad with \quad \beta_i V_i = \sum_{j=1}^{N} \overline{g_i s_j} + \sum_{k=1}^{K} \overline{g_i g_k}$$

$$= \left(\sum_{j=1}^{N} \overline{g_i s_j} + \sum_{k=1}^{K} \overline{g_i g_k} \right) J_{gi} - H_{gi}$$

Set $\quad H_{gi} = \sum_{j=1}^{N} J_{sj} + \sum_{k=1}^{K} J_{gk}$

$$Q_{gi} = \left(\sum_{j=1}^{N} \overline{g_i s_j} + \sum_{k=1}^{K} \overline{g_i g_k} \right) \left(J_{gi} - \sum_{j=1}^{N} J_{sj} - \sum_{k=1}^{K} J_{gk} \right)$$

$$= \sum_{j=1}^{N} \overline{g_i s_j} \left(J_{gi} - \sum_{j=1}^{N} J_{sj} - \sum_{k=1}^{K} J_{gk} \right) + \sum_{k=1}^{K} \overline{g_i g_k} \left(J_{gi} - \sum_{j=1}^{N} J_{sj} - \sum_{k=1}^{K} J_{gk} \right)$$

Here $= \begin{cases} \sum_{j=1}^{N} \overline{g_i s_j} \left(\sum_{k=1}^{K} J_{gk} \right) = 0 \\ \sum_{k=1}^{K} \overline{g_i g_k} \left(\sum_{j=1}^{N} J_{sj} \right) = 0 \end{cases}$

$$\therefore Q_{gi} = \sum_{j=1}^{N} \overline{g_i s_j} (J_{gi} - J_{sj}) + \sum_{k=1}^{K} \overline{g_i g_k} (J_{gi} - J_{gk})$$

Rearranging $\quad Q_{gi} = \left(\sum_{j=1}^{N} \overline{g_i s_j} + \sum_{k=1}^{K} \overline{g_i g_k} \right) J_{gi} - \sum_{j=1}^{N} \overline{g_i s_j} J_{sj} - \sum_{k=1}^{K} \overline{g_i g_k} J_{gk}$

$$= \left(\sum_{j=1}^{N} \overline{g_i s_j} + \sum_{k=1}^{K} \overline{g_i g_k} \right) J_{gi} - \left(\sum_{j=1}^{N} \overline{g_i s_j} J_{sj} + \sum_{k=1}^{K} \overline{g_i g_k} J_{gk} \right)$$

with $4\beta_i V_i = \left(\sum_{j=1}^{N} \overline{g_i s_j} + \sum_{k=1}^{K} \overline{g_i g_k} \right)$

$$Q_{gi} = 4\beta_i V \times J_{gi} - \left(\sum_{j=1}^{N} \overline{g_i s_j} J_{sj} + \sum_{k=1}^{K} \overline{g_i g_k} J_{gk} \right)$$

Here $J_{gi} = 4(1-\omega_i) E_{bgi} + \omega_i H_{gi}$ & $H_{gi} = \left(\sum_{j=1}^{N} J_{sj} + \sum_{k=1}^{K} J_{gk} \right)$

$$Q_{gi} = \beta_i V_i \ 4(1-\omega) E_{bgi} + \omega_i H_{gi} \ - \left(\sum_{j=1}^{N} \overline{g_i s_j} J_{sj} + \sum_{k=1}^{K} \overline{g_i g_k} J_{gk} \right)$$

$$= \beta_i V_i \ \left(4(1-\omega_i) E_{bgi} \right) \beta_i V_i \ \left(\omega_i H_{gi} \right) \left(\sum_{j=1}^{N} \overline{g_i s_j} J_{sj} + \sum_{k=1}^{K} \overline{g_i g_k} J_{gk} \right)$$

Substitute $\beta_i V_i H_{gi} = \left(\sum_{j=1}^{N} \overline{g_i s_j} J_{sj} + \sum_{k=1}^{K} \overline{g_i g_k} J_{gk} \right)$

$$Q_{gi} = \beta_i V_i \ 4(1-\omega_i) E_{bgi} \ + \omega_i \left(\sum_{j=1}^{N} \overline{g_i s_j} J_{sj} + \sum_{k=1}^{K} \overline{g_i g_k} J_{gk} \right) - \left(\sum_{j=1}^{N} \overline{g_i s_j} J_{sj} + \sum_{k=1}^{K} \overline{g_i g_k} J_{gk} \right)$$

$$\beta = \sigma_s + \kappa_i, \quad \omega_i = {}^{\sigma_s}\!/_{\beta_i} \quad \& \quad (1-\omega_i) = {}^{\kappa_i}\!/_{\beta_i}$$

$$Q_{gi} = \beta_i V_i \left(4 \left({}^{\kappa_i}\!/_{\beta_i} \right) E_{bgi} \right) + \ \omega_i - 1 \ \left(\sum_{j=1}^{N} \overline{g_i s_j} J_{sj} + \sum_{k=1}^{K} \overline{g_i g_k} J_{gk} \right) \qquad (7.11)$$

$$\therefore Q_{gi} = 4\kappa_i V_i E_{bgi} - (1-\omega_i) \left(\sum_{j=1}^{N} \overline{g_i s_j} J_{sj} + \sum_{k=1}^{K} \overline{g_i g_k} J_{gk} \right), i = 1,2,\ldots,\mathrm{K}$$

The radiosities in Equations (7.8) and (7.10) are eliminated by replacing it with the Equation (7.12) below:

$$\begin{aligned} J_{si} &= \varepsilon E_{bsi} + \rho_s H_{si} \\ J_{gk} &= 4(1-\omega) E_{bgk} + \omega H_{gi} \end{aligned} \qquad (7.12)$$

The substitution and simplification leads to:

$$\sum_{j=1}^{N} \left(\frac{\delta_{ij}}{\varepsilon_j} - \frac{\rho_j}{\varepsilon_j} \frac{\overline{s_i s_j}}{A_j} \right) h_{sj} - \sum_{k=1}^{K} \left(\frac{\overline{s_i g_k} \omega_k}{4\kappa_k V_k} \right) h_{gk} = \sum_{j=1}^{N} \ \overline{s_i s_j} \varepsilon_j \ E_{bsj} + \sum_{k=1}^{K} \ \overline{s_i g_k} (1-\omega_k) \ E_{bgk}, i = 1,2,\ldots,N \qquad (7.13)$$

$$-\sum_{j=1}^{N}\frac{\overline{g_i s_j}}{A_j}\frac{\rho_j}{\varepsilon_j}h_{sj}+\sum_{k=1}^{K}\left(\frac{\delta_{ik}}{1-\omega_k}-\frac{\overline{g_i g_k}\omega_k}{4\kappa_k V_k}\right)h_{gk} = \sum_{j=1}^{N}\overline{g_i g_j}\,\varepsilon_j E_{bsj}+\sum_{k=1}^{K}\overline{g_i g_k}(1-\omega_k)E_{bgk}, i=1,2,\ldots,K \quad (7.14)$$

where $h_{sj}=\varepsilon_j A_j H_{sj}$ and $h_{gk}=\kappa_k V_k H_{gk}$ are the irradiation on the surface and volume zones.

For simplicity, the substitutes shown in Table 7.2 are used to rewrite Equations (7.13) and (7.14) as:

$$T\cdot h_{sj}-U\cdot h_{gk}=S\cdot E_{bsj}+V\cdot E_{bgk} \quad (7.15)$$

and

$$-Q\cdot h_{sj}+W\cdot h_{gk}=R\cdot E_{bsj}+X\cdot E_{bgk} \quad (7.16)$$

Table 7.2. Equations (7.13) and (7.14) substitutes.

Equation (7.13)		**Equation (7.14)**	
$\sum_{j=1}^{N}\left(\frac{\delta_{ij}}{\varepsilon_j}-\frac{\rho_j}{\varepsilon_j}\frac{\overline{s_i s_j}}{A_j}\right)$	T	$\sum_{j=1}^{N}\frac{\overline{g_i s_j}}{A_j}\frac{\rho_j}{\varepsilon_j}$	Q
$\sum_{k=1}^{K}\left(\frac{\overline{s_i g_k}\omega_k}{4\kappa_k V_k}\right)$	U	$\sum_{k=1}^{K}\left(\frac{\delta_{ik}}{1-\omega_k}-\frac{\overline{g_i g_k}\omega_k}{4\kappa_k V_k}\right)$	W
$\sum_{j=1}^{N}\overline{s_i s_j}\varepsilon_j$	S	$\sum_{j=1}^{N}\overline{g_i g_j}\varepsilon_j$	R
$\sum_{k=1}^{K}\overline{s_i g_k}(1-\omega_k)$	V	$\sum_{k=1}^{K}\overline{g_i g_k}(1-\omega_k)$	X

These substitutes are in essence matrices of the forms shows as:

$$\sum_{j=1}^{N}\left(\frac{\delta_{ij}}{\varepsilon_j}-\frac{\rho_j}{\varepsilon_j}\frac{\overline{s_i s_j}}{A_j}\right)=T=\begin{pmatrix}\frac{1}{\varepsilon_1}-\frac{\rho_1}{\varepsilon_1}\frac{\overline{s_1 s_1}}{A_1} & -\frac{\rho_2}{\varepsilon_2}\frac{\overline{s_2 s_1}}{A_2} & \cdots & -\frac{\rho_N}{\varepsilon_N}\frac{\overline{s_1 s_N}}{A_N}\\ -\frac{\rho_1}{\varepsilon_1}\frac{\overline{s_2 s_1}}{A_1} & \frac{1}{\varepsilon_2}-\frac{\rho_2}{\varepsilon_2}\frac{\overline{s_2 s_2}}{A_2} & \cdots & -\frac{\rho_N}{\varepsilon_N}\frac{\overline{s_2 s_N}}{A_N}\\ \vdots & \vdots & \ddots & \vdots\\ -\frac{\rho_1}{\varepsilon_1}\frac{\overline{s_N s_1}}{A_1} & -\frac{\rho_2}{\varepsilon_2}\frac{\overline{s_N s_2}}{A_2} & \cdots & \frac{1}{\varepsilon_N}-\frac{\rho_N}{\varepsilon_N}\frac{\overline{s_N s_N}}{A_N}\end{pmatrix} \tag{7.17}$$

δ_{ij} is the Kronecker's delta function defined as:

$$\delta_{ij}=\begin{cases}0 & for \quad i\neq j\\ 1 & for \quad i=j\end{cases} \tag{7.18}$$

$$\sum_{k=1}^{K}\frac{\overline{s_i g_k}\omega_k}{4\kappa_k V_k}=U=\begin{pmatrix}\frac{\overline{s_1 g_1}\omega_1}{4\kappa_1 V_1} & \frac{\overline{s_1 g_2}\omega_2}{4\kappa_2 V_2} & \cdots & \frac{\overline{s_1 g_k}\omega_k}{4\kappa_k V_k}\\ \frac{\overline{s_2 g_1}\omega_1}{4\kappa_1 V_1} & \frac{\overline{s_2 g_2}\omega_2}{4\kappa_2 V_2} & \cdots & \frac{\overline{s_2 g_k}\omega_k}{4\kappa_k V_k}\\ \vdots & \vdots & \ddots & \vdots\\ \frac{\overline{s_N g_1}\omega_1}{4\kappa_1 V_1} & \frac{\overline{s_N g_2}\omega_2}{4\kappa_2 V_2} & \cdots & \frac{\overline{s_N g_k}\omega_k}{4\kappa_k V_k}\end{pmatrix} \tag{7.19}$$

$$\sum_{j=1}^{N}\frac{\overline{g_i s_j}}{A_j}\frac{\rho_j}{\varepsilon_j}=Q=\begin{pmatrix}\frac{\overline{g_1 s_1}}{A_1}\frac{\rho_1}{\varepsilon_1} & \frac{\overline{g_1 s_2}}{A_2}\frac{\rho_2}{\varepsilon_2} & \cdots & \frac{\overline{g_1 s_N}}{A_N}\frac{\rho_N}{\varepsilon_N}\\ \frac{\overline{g_2 s_1}}{A_1}\frac{\rho_1}{\varepsilon_1} & \frac{\overline{g_2 s_2}}{A_2}\frac{\rho_2}{\varepsilon_2} & \cdots & \frac{\overline{g_2 s_N}}{A_N}\frac{\rho_N}{\varepsilon_N}\\ \vdots & \vdots & \ddots & \vdots\\ \frac{\overline{g_k s_1}}{A_1}\frac{\rho_1}{\varepsilon_1} & \frac{\overline{g_k s_2}}{A_2}\frac{\rho_2}{\varepsilon_2} & \cdots & \frac{\overline{g_k s_N}}{A_N}\frac{\rho_N}{\varepsilon_N}\end{pmatrix} \tag{7.20}$$

$$\sum_{k=1}^{K}\overline{s_i g_k}(1-\omega_k)=V=\begin{pmatrix}\overline{s_1 g_1}(1-\omega_1) & \overline{s_1 g_2}(1-\omega_2) & \cdots & \overline{s_1 g_k}(1-\omega_k)\\ \overline{s_2 g_1}(1-\omega_1) & \overline{s_2 g_2}(1-\omega_2) & \cdots & \overline{s_2 g_k}(1-\omega_k)\\ \vdots & \vdots & \ddots & \vdots\\ \overline{s_N g_1}(1-\omega_1) & \overline{s_N g_2}(1-\omega_2) & \cdots & \overline{s_N g_k}(1-\omega_k)\end{pmatrix} \tag{7.21}$$

$$\sum_{j=1}^{N}\overline{s_i s_j}\varepsilon_j = S = \begin{pmatrix} \overline{s_1 s_1}\varepsilon_1 & \overline{s_1 s_2}\varepsilon_2 & \cdots & \overline{s_1 s_N}\varepsilon_N \\ \overline{s_2 s_1}\varepsilon_1 & \overline{s_2 s_2}\varepsilon_2 & \cdots & \overline{s_2 s_N}\varepsilon_N \\ \vdots & \vdots & \ddots & \vdots \\ \overline{s_N s_1}\varepsilon_1 & \overline{s_N s_2}\varepsilon_2 & \cdots & \overline{s_N s_N}\varepsilon_N \end{pmatrix} \tag{7.22}$$

$$\sum_{k=1}^{K}\left(\frac{\delta_{ik}}{1-\omega_k} - \frac{\overline{g_i g_k}\omega_k}{4\kappa_k V_k}\right) = W = \begin{pmatrix} \frac{1}{1-\omega_1} - \frac{\overline{g_1 g_1}\omega_1}{4\kappa_1 V_1} & -\frac{\overline{g_1 g_2}\omega_2}{4\kappa_2 V_2} & \cdots & -\frac{\overline{g_1 g_k}\omega_k}{4\kappa_k V_k} \\ -\frac{\overline{g_2 g_1}\omega_1}{4\kappa_1 V_1} & \frac{1}{1-\omega_2} - \frac{\overline{g_2 g_2}\omega_2}{4\kappa_2 V_2} & \cdots & -\frac{\overline{g_2 g_k}\omega_k}{4\kappa_k V_k} \\ \vdots & \vdots & \ddots & \vdots \\ -\frac{\overline{g_k g_1}\omega_1}{4\kappa_1 V_1} & -\frac{\overline{g_k g_2}\omega_2}{4\kappa_2 V_2} & \cdots & \frac{1}{1-\omega_k} - \frac{\overline{g_k g_k}\omega_k}{4\kappa_k V_k} \end{pmatrix} \tag{7.23}$$

$$\sum_{j=1}^{N}\overline{g_i g_j}\varepsilon_j = R = \begin{pmatrix} \overline{g_1 s_1}\varepsilon_1 & \overline{g_1 s_2}\varepsilon_2 & \cdots & \overline{g_1 s_N}\varepsilon_N \\ \overline{g_2 s_1}\varepsilon_1 & \overline{g_2 s_2}\varepsilon_2 & \cdots & \overline{g_2 s_N}\varepsilon_N \\ \vdots & \vdots & \ddots & \vdots \\ \overline{g_k s_1}\varepsilon_1 & \overline{g_k s_2}\varepsilon_2 & \cdots & \overline{g_k s_N}\varepsilon_N \end{pmatrix} \tag{7.24}$$

and

$$\sum_{k=1}^{K}\overline{g_i g_k}(1-\omega_k) = \mathrm{X} = \begin{pmatrix} \overline{g_1 g_1}(1-\omega_1) & \overline{g_1 g_2}(1-\omega_2) & \cdots & \overline{g_1 g_k}(1-\omega_k) \\ \overline{g_2 g_1}(1-\omega_1) & \overline{g_2 g_2}(1-\omega_2) & \cdots & \overline{g_2 g_k}(1-\omega_k) \\ \vdots & \vdots & \ddots & \vdots \\ \overline{g_k g_1}(1-\omega_1) & \overline{g_k g_2}(1-\omega_2) & \cdots & \overline{g_k g_k}(1-\omega_k) \end{pmatrix} \tag{7.25}$$

1) Known surface and medium temperatures (with isotropic scattering)

For known surface and gas temperatures, the irradiation fluxes in Equations (7.15) and (7.16) for surface and volumes zones are calculated using matrix inversion as:

$$h_s = P^{-1}\left[C \cdot E_{bs} + D \cdot E_{bg}\right] \tag{7.26}$$

and

$$h_g = W^{-1}\left[(\mathrm{Q} \cdot P^{-1} \cdot C + \mathrm{R}) \cdot E_{bs} + (\mathrm{Q} \cdot P^{-1} \cdot D + \mathrm{X}) \cdot E_{bg}\right] \tag{7.27}$$

where,

$$\begin{aligned} P &= T - U \cdot W^{-1} Q \\ C &= S + U \cdot W^{-1} R \\ D &= V + U \cdot W^{-1} X \end{aligned} \tag{7.28}$$

Equations (7.26) and (7.27) are then substituted into Equations (7.3) and (7.4) to calculate unknown surface and volume heat fluxes.

A detailed derivative of Equations (7.26) and (7.27) is given as:

$$T \cdot h_s - U \cdot h_g = S \cdot E_{bs} + V \cdot E_{bg} \qquad (1)$$
$$-Q \cdot h_s + W \cdot h_g = R \cdot E_{bs} + X \cdot E_{bg} \qquad (2)$$

$(2) \rightarrow \mathrm{h}_g$

$$h_g = W^{-1}\left[Q \cdot h_s + R \cdot E_{bs} + X \cdot E_{bg}\right] \qquad (3)$$

$(3) \rightarrow (1)$

$$T \cdot h_s - U \cdot W^{-1}\left[Q \cdot h_s + R \cdot E_{bs} + X \cdot E_{bg}\right] = S \cdot E_{bs} + V \cdot E_{bg}$$
$$T \cdot h_s - U \cdot W^{-1} \cdot Q \cdot h_s - U \cdot W^{-1} \cdot R \cdot E_{bs} - U \cdot W^{-1} \cdot X \cdot E_{bg} = S \cdot E_{bs} + V \cdot E_{bg}$$
$$\left[T - U \cdot W^{-1} \cdot Q\right] h_s = U \cdot W^{-1} \cdot R \cdot E_{bs} + U \cdot W^{-1} \cdot X \cdot E_{bg} + S \cdot E_{bs} + V \cdot E_{bg}$$
$$\left[T - U \cdot W^{-1} \cdot Q\right] h_s = \left[S + U \cdot W^{-1} \cdot R\right] E_{bs} + \left[V + U \cdot W^{-1} \cdot X\right] E_{bg}$$

with $\begin{cases} P = \left[T - U \cdot W^{-1} \cdot Q\right] \\ C = \left[S + U \cdot W^{-1} \cdot R\right] \qquad (4) \\ D = \left[V + U \cdot W^{-1} \cdot X\right] \end{cases}$ (7.29)

$$P \cdot h_s = C \cdot E_{bs} + D \cdot E_{bg} \qquad (5)$$
$$\therefore h_s = P^{-1}\left[C \cdot E_{bs} + D \cdot E_{bg}\right] \qquad (6)$$

$(6) \rightarrow (3)$

$$h_g = W^{-1}\left[Q \cdot P^{-1}\left[C \cdot E_{bs} + D \cdot E_{bg}\right] + R \cdot E_{bs} + X \cdot E_{bg}\right]$$
$$h_g = W^{-1}\left[Q \cdot P^{-1} C \cdot E_{bs} + Q \cdot P^{-1} D \cdot E_{bg} + R \cdot E_{bs} + X \cdot E_{bg}\right]$$
$$h_g = W^{-1}\left[\left[Q \cdot P^{-1} C + R\right] E_{bs} + \left[Q \cdot P^{-1} D + X\right] E_{bg}\right]$$
$$h_g = W^{-1}\left[\left[Q \cdot P^{-1} C + R\right] E_{bs} + \left[Q \cdot P^{-1} D + X\right] E_{bg}\right]$$
$$h_g = W^{-1}\left[Q \cdot P^{-1} C + R\right] E_{bs} + W^{-1}\left[Q \cdot P^{-1} D + X\right] E_{bg}$$

2) Known surface temperatures and heat source (with isotropic scattering)

For this case a heat source term is introduced as:

$$Q_g = 4\kappa V E_{bg} - h_g \tag{7.30}$$

The medium emissive power (E_{bg}) is obtained from Equations (7.27) and (7.30) as:

$$E_{bg} = \left[4\kappa V - W^{-1}\cdot\ \mathrm{Q}\cdot P^{-1}\cdot D + \mathrm{X}\right]^{-1}\left[W^{-1}\cdot\ \mathrm{Q}\cdot P^{-1}\cdot C + \mathrm{R}\ \cdot E_{bs} + Q_g\right] \tag{7.31}$$

The gas temperature distributions can then be calculated from Equation (7.31). Equation (7.31) can also be substituted into Equations (7.32) and (7.33) which are identical to Equations (7.27) and (7.30) to obtain the surface and gas irradiations, respectively.

$$h_s = P^{-1}\ C\cdot E_{bs}\ + P^{-1}\left[D\cdot E_{bg}\right] \tag{7.32}$$

and

$$h_g = W^{-1}\left[(\mathrm{Q}\cdot P^{-1}\cdot C + \mathrm{R})\cdot E_{bs} + (\mathrm{Q}\cdot P^{-1}\cdot D + \mathrm{X})\cdot E_{bg}\right] \tag{7.33}$$

In this case, gas temperature distribution and surface heat fluxes are calculated.

A detailed derivative of the gas emissive power (E_{bg}) in Equation (7.31) is given as:

$$\begin{aligned}
&h_g = W^{-1}\left[(\mathrm{Q}\cdot P^{-1}\cdot C + \mathrm{R})\cdot E_{bs} + (\mathrm{Q}\cdot P^{-1}\cdot D + \mathrm{X})\cdot E_{bg}\right] \quad (1)\\
&Q_g = 4\kappa V\cdot E_{bg} - h_g \quad (2)\\
&(2)\rightarrow h_g\\
&h_g = 4\kappa V\cdot E_{bg} - Q_g \quad (3)\\
&(3)\quad \mathrm{into}\quad (1)\\
&4\kappa V\cdot E_{bg} - Q_g = W^{-1}\left[(\mathrm{Q}\cdot P^{-1}\cdot C + \mathrm{R})\cdot E_{bs} + (\mathrm{Q}\cdot P^{-1}\cdot D + \mathrm{X})\cdot E_{bg}\right]\\
&4\kappa V\cdot E_{bg} - Q_g = W^{-1}\cdot(\mathrm{Q}\cdot P^{-1}\cdot C + \mathrm{R})\cdot E_{bs} + W^{-1}\cdot(\mathrm{Q}\cdot P^{-1}\cdot D + \mathrm{X})\cdot E_{bg}\\
&\left[4\kappa V - W^{-1}\cdot(\mathrm{Q}\cdot P^{-1}\cdot D + \mathrm{X})\right]\cdot E_{bg} = W^{-1}\cdot(\mathrm{Q}\cdot P^{-1}\cdot C + \mathrm{R})\cdot E_{bs} + Q_g\\
&\therefore E_{bg} = \left[4\kappa V - W^{-1}\cdot(\mathrm{Q}\cdot P^{-1}\cdot D + \mathrm{X})\right]^{-1}\left[W^{-1}\cdot(\mathrm{Q}\cdot P^{-1}\cdot C + \mathrm{R})\cdot E_{bs} + Q_g\right]
\end{aligned} \tag{7.34}$$

Radiation heat transfer in emitting-absorbing media without scattering

When dealing with emitting-absorbing media in the absence of scattering, the scattering albedo $\omega = 0$ become zero. In this case, the U-matrix in Equation (7.19) becomes a zero-matrix and the W-matrix in Equation (7.23) becomes an identity matrix, Z which brings about changes in Equations (7.15) and (7.16). As a result, Equations (7.15) and (7.16) reduce to:

$$T \cdot h_s = S \cdot E_{bs} + DEA\_sg \cdot E_{bg} \tag{7.35}$$

and

$$-Q \cdot h_s + Z \cdot h_g = R \cdot E_{bs} + DEA\_gg \cdot E_{bg} \tag{7.36}$$

where Z is an identity matrix replacing W in Equation (7.23) and DEA_sg as well as DEA_gg are the surface-to-volume and volume-to-volume direct exchange areas matrices, respectively replacing the V-matrix and X-matrix. This is all influenced by the absence of a scattering albedo $\omega = 0$. Two cases for radiation heat transfer are derived below:

1) Known surface and gas temperatures (without scattering)

For known surface and gas temperatures, the irradiation flux in Equations (7.13) and (7.14) is this calculated through the use of matrix inversion results on surface and volumes zones are obtained respectively from For known surface and gas temperatures, the irradiation flux in Equations (7.13) and (7.14) is this calculated through the use of matrix inversion results on surface and volumes zones are obtained respectively from:

$$h_s = T^{-1}\left[S \cdot E_{bs} + DEA\_sg \cdot E_{bg}\right] \tag{7.37}$$

and

$$h_g = Z^{-1}\left[Q \cdot h_s + R \cdot E_{bs} + DEA\_gg \cdot E_{bg}\right] \tag{7.38}$$

Equations (7.37) and (7.38) are then substituted into Equations (7.3) and (7.4) to calculate unknown surface and volume heat fluxes.

A detailed derivative of Equations (7.37) and (7.38) is given as:

$$
\begin{aligned}
&T \cdot h_s - U \cdot h_g = S \cdot E_{bs} + V \cdot E_{bg} \qquad (1)\\
&-Q \cdot h_s + W \cdot h_g = R \cdot E_{bs} + X \cdot E_{bg} \qquad (2)\\
&(1) \rightarrow \begin{cases} U = 0 \\ V = DEA\_sg \end{cases}\\
&T \cdot h_s = S \cdot E_{bs} + DEA\_sg \cdot E_{bg} \qquad (3)\\
&\therefore h_s = T^{-1}\left[S \cdot E_{bs} + DEA\_sg \cdot E_{bg}\right]\\
&(2) \rightarrow \begin{cases} W = Z \\ X = DEA\_gg \end{cases}\\
&-Q \cdot h_s + Z \cdot h_g = R \cdot E_{bs} + DEA\_gg \cdot E_{bg} \qquad (4)\\
&\therefore h_g = Z^{-1}\left[Q \cdot h_s + R \cdot E_{bs} + DEA\_gg \cdot E_{bg}\right]
\end{aligned}
\tag{7.39}
$$

2) Known surface temperatures and heat source (without scattering)

For this case heat source term is introduced as:

$$Q_g = 4\beta V E_{bg} - h_g \tag{7.40}$$

The gas emissive power (E_{bg}) is calculated from Equations (7.27) and (7.30) as:

$$E_{bg} = \left[4\beta V - Z^{-1} \cdot \ \mathrm{Q} \cdot T^{-1} \cdot DEA\_sg + DEA\_gg \ \right]^{-1}\left[Z^{-1} \cdot \ \mathrm{Q} \cdot T^{-1} \cdot S + \mathrm{R} \ \cdot E_{bs} + Q_g\right] \tag{7.41}$$

The gas temperature distributions can then be calculated from Equation (7.41). Equation (7.41) can also be substituted into Equations (7.42) and (7.43) which are identical to Equations (7.37) and (7.38) to obtain the surface and gas irradiations, respectively.

$$h_s = T^{-1}\left[S \cdot E_{bs} + DEA\_sg \cdot E_{bg}\right] \tag{7.42}$$

and

$$h_g = Z^{-1}\left[Q \cdot h_s + R \cdot E_{bs} + DEA\_gg \cdot E_{bg}\right] \tag{7.43}$$

In this case, gas temperature distribution and surface heat fluxes are calculated.

A detailed derivative of the gas emissive power (E_{bg}) in (7.41) is given as:

$$\begin{aligned}
&h_g = Z^{-1}\left[Q \cdot h_s + R \cdot E_{bs} + DEA_gg \cdot E_{bg}\right] && (1)\\
&Q_g = 4\beta V \cdot E_{bg} - h_g && (2)\\
&(2) \rightarrow h_g\\
&h_g = 4\beta V \cdot E_{bg} - Q_g && (3)\\
&(3) \quad into \quad (1)\\
&4\beta V \cdot E_{bg} - Q_g = Z^{-1}\left[Q \cdot h_s + R \cdot E_{bs} + DEA_gg \cdot E_{bg}\right] && (4)\\
&h_s = T^{-1}\left[S \cdot E_{bs} + DEA_sg \cdot E_{bg}\right] && (5)\\
&(5) \rightarrow (4)\\
&4\beta V \cdot E_{bg} - Q_g = Z^{-1} \cdot \left[\mathrm{Q} \cdot T^{-1} \cdot DEA_sg + DEA_gg\right] \cdot E_{bg} + Z^{-1} \cdot \left[\mathrm{Q} \cdot T^{-1} \cdot S + \mathrm{R}\right] \cdot E_{bs}\\
&\left[4\beta V - W^{-1} \cdot \left[\mathrm{Q} \cdot T^{-1} \cdot DEA_sg + DEA_gg\right]\right] \cdot E_{bg} = W^{-1} \cdot \left[\mathrm{Q} \cdot T^{-1} \cdot S + \mathrm{R}\right] \cdot E_{bs} + Q_g\\
&\therefore E_{bg} = \left[4\beta V - Z^{-1} \cdot \left[\mathrm{Q} \cdot T^{-1} \cdot DEA_sg + DEA_gg\right]\right]^{-1} \left[Z^{-1} \cdot \left[\mathrm{Q} \cdot T^{-1} \cdot S + \mathrm{R}\right] \cdot E_{bs} + Q_g\right]
\end{aligned} \tag{7.44}$$

where Q_g is the medium heat source in kW.

Appendix C. Verification study approaches

C. 1 Direct exchange area approximations according to Hottel and Sarofim (1967):

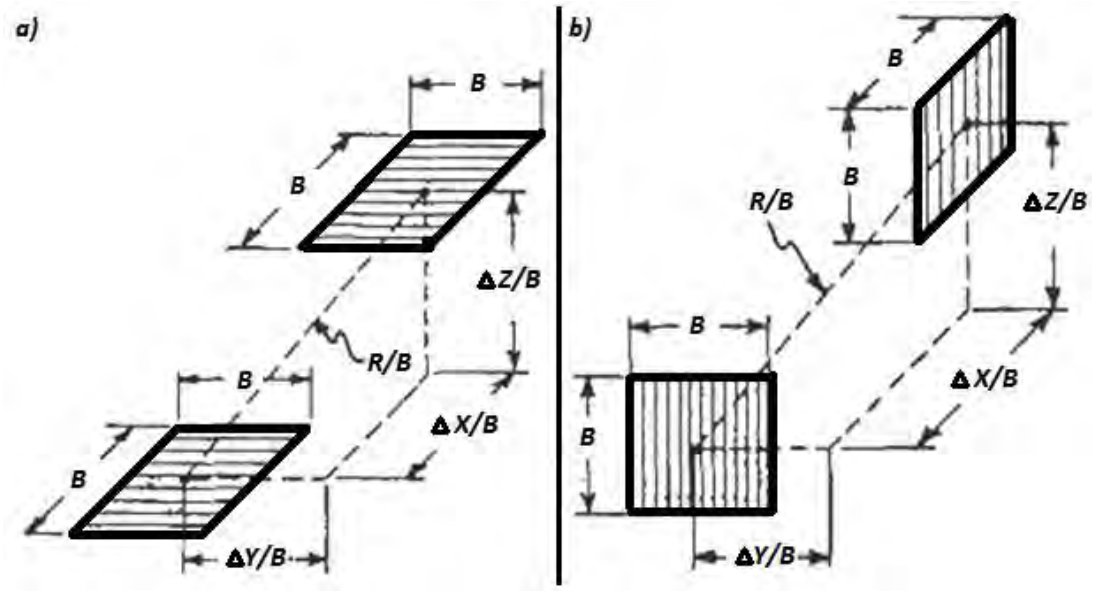

Figure 7.4. Geometry of direct exchange between parallel and perpendicular squares (Hottel & Cohen, 1958).

C. 1.1 Surface-to-surface (Opposite):

$$\overline{s_j s_i}(\|) = B^2 \cdot \frac{\exp(-\beta R)\cdot\left(\frac{\Delta x}{B}\right)^2}{\pi\cdot\left(\frac{R}{B}\right)^4} \qquad \text{Front} \Leftrightarrow \text{Back} \tag{7.45}$$

$$\overline{s_j s_i}(\|) = B^2 \cdot \frac{\exp(-\beta R)\cdot\left(\frac{\Delta y}{B}\right)^2}{\pi\cdot\left(\frac{R}{B}\right)^4} \qquad \text{Left} \Leftrightarrow \text{Right} \tag{7.46}$$

$$\overline{s_j s_i}(\|) = B^2 \cdot \frac{\exp(-\beta R)\cdot\left(\frac{\Delta z}{B}\right)^2}{\pi\cdot\left(\frac{R}{B}\right)^4} \qquad \text{Bottom} \Leftrightarrow \text{Top} \tag{7.47}$$

C. 1.2 Surface-to-surface (perpendicular):

$$\overline{s_j s_i}(\perp) = B^2 \cdot \frac{\exp(-\beta R)\cdot(\frac{\triangle x}{B})\cdot(\frac{\triangle z}{B})}{\pi\cdot(\frac{R}{B})^4} \quad \text{Bottom/Top} \Leftrightarrow \text{Front/Back} \tag{7.48}$$

$$\overline{s_j s_i}(\perp) = B^2 \cdot \frac{\exp(-\beta R)\cdot(\frac{\triangle y}{B})\cdot(\frac{\triangle z}{B})}{\pi\cdot(\frac{R}{B})^4} \quad \text{Left/Right} \Leftrightarrow \text{Bottom/Top} \tag{7.49}$$

$$\overline{s_j s_i}(\perp) = B^2 \cdot \frac{\exp(-\beta R)\cdot(\frac{\triangle x}{B})\cdot(\frac{\triangle y}{B})}{\pi\cdot(\frac{R}{B})^4} \quad \text{Front/Back} \Leftrightarrow \text{Left/Right} \tag{7.50}$$

B. 1.3 Volume-to-volume

$$\overline{g_j g_i} = B^2 \cdot (\beta B)^2 \cdot \frac{\exp(-\beta R)}{\pi\cdot(\frac{R}{B})^2} \tag{7.51}$$

C. 1.4 Volume-to-surface

$$\overline{g_j s_i} = B^2 \cdot \beta B \cdot \frac{\exp(-\beta R)\cdot(\frac{\triangle x}{B})}{\pi\cdot(\frac{R}{B})^3} \quad \text{Volume} \Leftrightarrow \text{Front/Back} \tag{7.52}$$

$$\overline{g_j s_i} = B^2 \cdot \beta B \cdot \frac{\exp(-\beta R)\cdot(\frac{\triangle y}{B})}{\pi\cdot(\frac{R}{B})^3} \quad \text{Volume} \Leftrightarrow \text{Left/Right} \tag{7.53}$$

$$\overline{g_j s_i} = B^2 \cdot \beta B \cdot \frac{\exp(-\beta R)\cdot(\frac{\triangle z}{B})}{\pi\cdot(\frac{R}{B})^3} \quad \text{Volume} \Leftrightarrow \text{Bottom/Top} \tag{7.54}$$

C. 2 View factors functions in Mathcad

C. 2.1 Parallel

$$
\begin{aligned}
VF(X, Y, LL) := \;& XX \leftarrow \frac{X}{LL} \\
& YY \leftarrow \frac{Y}{LL} \\
& A \leftarrow \frac{2}{\pi \cdot XX \cdot YY} \\
& B \leftarrow \ln\left[\sqrt{\frac{\left(1+XX^2\right)\cdot\left(1+YY^2\right)}{1+XX^2+YY^2}}\right] \\
& C \leftarrow XX\cdot\left(1+YY^2\right)^{\frac{1}{2}}\cdot \operatorname{atan}\left[\frac{XX}{\left(1+YY^2\right)^{\frac{1}{2}}}\right] \\
& D \leftarrow YY\cdot\left(1+XX^2\right)^{\frac{1}{2}}\cdot \operatorname{atan}\left[\frac{YY}{\left(1+XX^2\right)^{\frac{1}{2}}}\right] \\
& E \leftarrow XX\cdot \operatorname{atan}(XX) \\
& F \leftarrow YY\cdot \operatorname{atan}(YY) \\
& F_{12} \leftarrow A\cdot(B+C+D-E-F)
\end{aligned}
\tag{7.55}
$$

C. 2.2 Perpendicular

$$
\begin{aligned}
VFF(X, Y, Z) := \;& H \leftarrow \frac{Z}{X} \\
& W \leftarrow \frac{Y}{X} \\
& A \leftarrow \frac{1}{\pi \cdot W} \\
& B \leftarrow W \cdot \operatorname{atan}\left(\frac{1}{W}\right) \\
& C \leftarrow H \cdot \operatorname{atan}\left(\frac{1}{H}\right) \\
& D \leftarrow \left(H^2 + W^2\right)^{\frac{1}{2}} \cdot \operatorname{atan}\left[\frac{1}{\left(H^2 + W^2\right)^{\frac{1}{2}}}\right] \\
& E \leftarrow \ln\left[\frac{\left(1 + W^2\right)\cdot\left(1 + H^2\right)}{1 + H^2 + W^2} \cdot \left[\frac{W^2 \cdot \left(1 + H^2 + W^2\right)}{\left(1 + W^2\right)\cdot\left(H^2 + W^2\right)}\right]^{W^2} \cdot \left[\frac{H^2 \cdot \left(1 + W^2 + H^2\right)}{\left(1 + H^2\right)\cdot\left(H^2 + W^2\right)}\right]^{H^2}\right] \\
& F_{12} \leftarrow A \cdot \left(B + C - D + \frac{1}{4} \cdot E\right)
\end{aligned}
\tag{7.56}
$$

C. 3 Tucker's coefficients

Table 7.3. Tucker's coefficients (Tucker, 1986).

	Bottom-Back	**Bottom-Top**	**Bottom- Volume**	**Volume-Volume**
	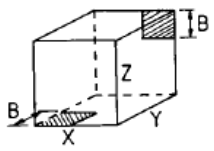	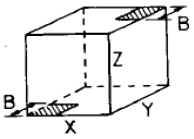	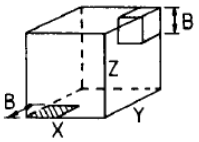	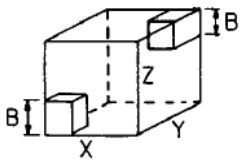
C	0.023	0.0351	0.0135	0.0283
A	$a_0 + a_1 \cdot \beta B + \ldots + a_4 \cdot \beta B^4$			
a_0	2.245	2.4015	1.514	1.147
a_1				-0.062
a_2				0.00132

Appendix D. Mathcad sample calculation

D. Mathcad sample calculation

Input parameters

The dimensions of the enclosure:
[lx = width, ly = length & lz = height]

$l_x := 2m \qquad l_y := 2m \qquad l_z := 4m$

Number of increments/nodes in the x, y and z direction:

$n_x := 2 \qquad n_y := 2 \qquad n_z := 2$

Extinction coefficient:

$Beta := 0.4m^{-1}$

Surface emissivity:

$\varepsilon_s := 0.7$

Heat source:

$Heat_s := 5\frac{kW}{m^3}$

Surface temperature:

$Temp_s := 300K$

Stephan Boltzmann constant:

$\sigma_s := 5.67 \cdot 10^{-8}\frac{W}{m^2 K^4}$

Enclosure discretisation

Total number of SURFACE zones/nodes:

$n_s := 2 \cdot (n_x \cdot n_y) + 2 \cdot (n_x \cdot n_z) + 2(n_y \cdot n_z)$

Total number of VOLUME zones/nodes:

$n_v := n_x \cdot n_y \cdot n_z$

TOTAL number of zones/nodes:

$n_t := n_s + n_v$

Discretisation of the enclosure
SURFACE NODES:
[The enclosure is divided into 6 planes, they are; Front, Back, Bottom, Top, Left & Right].
Each node holds information of its position in terms of the x, y & z co-ordinates of the node centre, the surface normal vector, the area of the small node as well as the large area from of the place without discretisation.

Direct exchange area functions

The DEA calculation from SURFACE to SURFACE:
Equation 4.12

$$\text{Front} := \left| \begin{array}{l} \text{for } i \in 0 .. n_y - 1 \\ \quad \text{for } j \in 0 .. n_z - 1 \\ \quad\quad P_{j,i} \leftarrow \begin{bmatrix} \frac{l_x}{m} \\ (0.5 + i) \cdot \frac{\frac{l_y}{m}}{n_y} \\ (0.5 + j) \cdot \frac{\frac{l_z}{m}}{n_z} \\ 1 \\ 0 \\ 0 \\ \left(\frac{\frac{l_z}{m}}{n_z}\right) \cdot \left(\frac{\frac{l_y}{m}}{n_y}\right) \\ \left(\frac{l_z}{m}\right) \cdot \left(\frac{l_y}{m}\right) \end{bmatrix}^T \\ P \end{array} \right.$$

$$
\begin{aligned}
SS(A, B) := \;& R_{AB} \leftarrow \left[(A_0 - B_0)m \quad (A_1 - B_1)m \quad (A_2 - B_2)m \right]^T \\
& R \leftarrow \sqrt{\left(R_{AB_0}\right)^2 + \left(R_{AB_1}\right)^2 + \left(R_{AB_2}\right)^2} \\
& n_A \leftarrow \sqrt{(A_3)^2 + (A_4)^2 + (A_5)^2} \\
& n_B \leftarrow \sqrt{(B_3)^2 + (B_4)^2 + (B_5)^2} \\
& cos_A \leftarrow \frac{\left| \left[\sqrt{\left(R_{AB_0}\right)^2} \quad \sqrt{\left(R_{AB_1}\right)^2} \quad \sqrt{\left(R_{AB_2}\right)^2} \right]^T \cdot \left(A_3 \quad A_4 \quad A_5 \right)^T \right|}{n_A \cdot R} \\
& cos_B \leftarrow \frac{\left| \left[\sqrt{\left(R_{AB_0}\right)^2} \quad \sqrt{\left(R_{AB_1}\right)^2} \quad \sqrt{\left(R_{AB_2}\right)^2} \right]^T \cdot \left(B_3 \quad B_4 \quad B_5 \right)^T \right|}{n_B \cdot R} \\
& F_{AB} \leftarrow \frac{\exp(-Beta \cdot R) \cdot \left(cos_A \cdot cos_B\right) \cdot \left(A_6 m^2\right) \cdot \left(B_6 m^2\right)}{R^2 \cdot \pi \, m^2} m^2
\end{aligned}
$$

Application of the direct exchange area functions

DEAs from the Front surface to the Back surface:

$$
\begin{aligned}
FB := \;& \text{for} \quad j \in 0 .. n_y - 1 \\
& \quad \text{for} \quad k \in 0 .. n_z - 1 \\
& \quad\quad FB1_{k,j} \leftarrow SS\left(Front_{0,0}^T, Back_{k,j}^T\right) \\
& \quad\quad FB2_{k,j} \leftarrow SS\left(Front_{1,0}^T, Back_{k,j}^T\right) \\
& \quad\quad FB3_{k,j} \leftarrow SS\left(Front_{0,1}^T, Back_{k,j}^T\right) \\
& \quad\quad FB4_{k,j} \leftarrow SS\left(Front_{1,1}^T, Back_{k,j}^T\right) \\
& (FB1 \quad FB2 \quad FB3 \quad FB4)
\end{aligned}
$$

Here are the DEAs from the 4 Front surfaces to the 4 Back surfaces:

$$P = \begin{pmatrix} 0.143 & 0.026 & 0.083 & 0.019 \\ 0.026 & 0.143 & 0.019 & 0.083 \\ 0.083 & 0.019 & 0.143 & 0.026 \\ 0.019 & 0.083 & 0.026 & 0.143 \end{pmatrix} m^2$$

Smoothing direct exchange areas

Weighting factors:
Equation 4.15
[The weighting factors are set equal to the square of the direct exchange areas]

$$\begin{aligned} &Weight := \left| \begin{array}{l} \text{for } i \in 0 .. n_t - 1 \\ \quad \text{for } j \in 0 .. n_t - 1 \\ \quad\quad RR_{i,j} \leftarrow DEAs_{i,j} \cdot DEAs_{i,j} \\ RR \end{array} \right. \end{aligned}$$

Equation 7.13

$$LL := RR^{-1} \cdot \left(Cc^T \right)$$

Lagrange multipliers:
From Equation 3.43 for Equation 4.22 / 3.41

$$\begin{aligned} &L1 := \left| \begin{array}{l} \text{for } i \in 0 .. n_t - 1 \\ \quad \text{for } j \in 0 .. n_t - 1 \\ \quad\quad l_{i,j} \leftarrow (LL)_{j,0} \\ l \end{array} \right. \end{aligned}$$

Smoothed DEAs:

Equation 4.22 / 3.41

$$\begin{aligned} &XXX := DEAs + \left| \begin{array}{l} \text{for } i \in 0 .. n_t - 1 \\ \quad \text{for } j \in 0 .. n_t - 1 \\ \quad\quad l_{i,j} \leftarrow Weight_{i,j} \cdot lam_{i,j} \\ l \end{array} \right. \end{aligned}$$

Radiation heat transfer network based on the zonal method

The T-matrix:
Equation 7.30

$$T_{mat} := \left| \begin{array}{l} \text{for } i \in 0..n_s - 1 \\ \quad \text{for } j \in 0..n_s - 1 \\ \quad\quad \left| \begin{array}{l} k_{i,j} \leftarrow \dfrac{1}{\varepsilon mat_{i,j}} - \dfrac{\left[\left(1-\varepsilon mat\right)_{i,j}\right]}{\varepsilon mat_{i,j}} \cdot pp_{i,j} \quad \text{if } i = j \\ k_{i,j} \leftarrow \dfrac{-\left[\left(1-\varepsilon mat\right)_{i,j}\right]}{\varepsilon mat_{i,j}} \cdot pp_{i,j} \quad \text{otherwise} \end{array} \right. \\ k \end{array} \right.$$

The Q-matrix:
Equation 7.17

$$Q_{mat} := \left| \begin{array}{l} \text{for } i \in 0..n_v - 1 \\ \quad \text{for } j \in 0..n_s - 1 \\ \quad\quad l_{i,j} \leftarrow \dfrac{DEA\_gs_{i,j}}{Area_{i,j}} \cdot \dfrac{\left(1-\varepsilon mat_{i,j}\right)}{\varepsilon mat_{i,j}} \\ l \end{array} \right.$$

The sg-matrix:
Equation 7.34 for ω =0

$$sg := DEA\_sg$$

The S-matrix:
Equation 7.22

$$S_{mat} := \left| \begin{array}{l} \text{for } i \in 0..n_s - 1 \\ \quad \text{for } j \in 0..n_s - 1 \\ \quad\quad l_{i,j} \leftarrow DEA\_ss_{i,j} \cdot \varepsilon mat_{i,j} \\ l \end{array} \right.$$

Surface heat rate:

$$Q\_s := \left| \begin{array}{l} \text{for} \quad i \in 0 .. n_s - 1 \\ \quad l_{i,0} \leftarrow \varepsilon_s \cdot \left(b_{t_{0,0}}{}^{T} \right)_{i,0} \cdot E_{bs_{i,0}} - h_{s_{i,0}} \\ l \end{array} \right.$$

Volume heat rate:

$$Q\_g := \left| \begin{array}{l} \text{for} \quad i \in 0 .. n_v - 1 \\ \quad l_{i,0} \leftarrow \left(b_{t_{0,1}}{}^{T} \right)_{i,0} \cdot E_{bg_{i,0}} - h_{g_{i,0}} \\ l \end{array} \right.$$

Surface heat flux:
Equation 7.3

$$q\_s := \frac{Q\_s}{\left(b_{t_{0,0}} \right)_{0,0}}$$

Volume heat flux:
Equation 7.4

$$q\_g := \frac{Q\_g}{\left(b_{t_{0,0}} \right)_{0,0}}$$

Energy balance:

$$\sum Q\_s = -80\,m^2 \cdot \frac{kW}{m^2}$$

$$\sum Q\_g = 80\,m^2 \cdot \frac{kW}{m^2}$$

Network results

Surface heat fluxes

$q\_s =$

	0
0	-2.086
1	-2.086
2	-2.086
3	-2.086
4	-2.086
5	-2.086
6	-2.086
7	-2.086
8	-0.828
9	-0.828
10	-0.828
11	-0.828
12	-0.828
13	-0.828
14	-0.828
15	-0.828
16	-2.086
17	-2.086
18	-2.086
19	-2.086
20	-2.086
21	-2.086
22	-2.086
23	-2.086

$\cdot \frac{kW}{m^2}$

Medium temperature distribution

$$Temp_g = \begin{pmatrix} 542.703 \\ 542.703 \\ 542.703 \\ 542.703 \\ 542.703 \\ 542.703 \\ 542.703 \\ 542.703 \end{pmatrix} K$$

Appendix E. Program codes

E. 1 Primary case

```
clc
clear
stacksize('max')
currentStackSize = stacksize();
tic()
//INPUTS//////////////////////////////////////////////////////////////////////
// The Dimensions of the enclosure: W,L and H:
W = 2 // Width in the x  direction
L = 2 // Length in the y direction
H = 4 // Height in the direction
// Number of Increments in the W, L and H direction:
n = 5 // Increments in the W (x) direction
m = 5 // Increments in the L (y) direction
o = 10 // Increments in the H (z) direction
n_t=n*m*o+2*(n*o)+2*(m*o)+2*(n*m)  //Total nr of nodes
n_s=2*(n*o)+2*(m*o)+2*(n*m)  // Total nr of surface nodes
n_v=n*m*o  // Total nr of volume nodes
////Surface nodes////
F_n=1:m*o
B_n=m*o+1:2*(m*o)
Bo_n=2*(m*o)+1:2*(m*o)+n*m
T_n=2*(m*o)+(n*m)+1:2*(m*o)+2*(n*m)
L_n=2*(m*o)+2*(n*m)+1:2*(m*o)+2*(n*m)+n*o
R_n=2*(m*o)+2*(n*m)+n*o+1:2*(m*o)+2*(n*m)+2*(n*o)

// PARTICIPATING MEDIA PROPERTIES
abso=0.15 // Absorption coefficient (m^-1)
scat=0.35 // Scattering coefficient (m^-1)
Beta = abso+scat // Extinction coefficient (m^-1)
wi=scat/Beta //scattering/Beta - Scattering albedo
// SURFACE PROPERTIES
emissivity=0.7
eps=emissivity*ones(1,n_s)  // Emissivities
eps(1,T_n)=0.85
//////////////////////////////////////////////////////////////////////////
// Case 1: Known surface and gas temperatures
//Temp_s=900*ones(n_s,1) // Surface Temperatures (K)
//Temp_g=1000*ones(n_v,1) // Medium  Temperatures (K)

// Case 2: Known surface temperatures and heat source
HeatSource=5  // Heat source (kW/m^3)
Temp_s=900*ones(n_s,1)  //  Surface Temperatures  (K)
Temp_s(T_n,1)=1200
Temp_s(Bo_n,1)=400
//////////////////////////////////////////////////////////////////////////
//MODEL DEVELOPMENT
// (1)  DISCRETISATION OF THE ENCLOSURE
```

```
// SURFACE NODES: The enclosure is divided into 6 planes, they are; Front, Back, Bottom, Top, Left & Right].Each node holds information of its position in terms of the x,y & z co-ordinates of the node, the surface normal vector, the area of the small node as well as the large area of the plane without discretisation
function [Front]=S1(jj, kk)
   node = 0;
for j = 1:jj
   for k = 1:kk
         node = node + 1;
         Front(node,1) = W  // Front Surface
         Front(node,2) = L/m*(j-0.5)
         Front(node,3) = H/o*(k-0.5)
         Front(node,4) = 1
         Front(node,5) = 0
         Front(node,6) = 0
         Front(node,7) = (L/m)*(H/o)
         Front(node,8) = (L)*(H)
   end
end
endfunction
Front=S1(m,o)

function [Back]=S2(jj, kk)
   node = 0;
for j = 1:jj
   for k = 1:kk
         node = node + 1;
         Back(node,1) = W/n*0  // Back Surface
         Back(node,2) = L/m*(j-0.5)
         Back(node,3) = H/o*(k-0.5)
         Back(node,4) = 1
         Back(node,5) = 0
         Back(node,6) = 0
         Back(node,7) = (L/m)*(H/o)
         Back(node,8) = (L)*(H)
   end
end
endfunction
Back=S2(m,o)

function [Bottom]=S3(ii, jj)
   node = 0;
for j = 1:jj
   for i = 1:ii
         node = node + 1;
         Bottom(node,1) = W/n*(i-0.5)  // Bottom surface
         Bottom(node,2) = L/m*(j-0.5)
         Bottom(node,3) = H/o*0
         Bottom(node,4) = 0
         Bottom(node,5) = 0
         Bottom(node,6) = 1
         Bottom(node,7) =(W/n)*(L/m)
         Bottom(node,8) = (W)*(L)
   end
end
endfunction
Bottom=S3(n,m)
```

```
function [Top]=S4(ii, jj)
   node = 0;
for j = 1:jj
   for i = 1:ii
         node = node + 1;
         Top(node,1) = W/n*(i-0.5)  // Top surface
         Top(node,2) = L/m*(j-0.5)
         Top(node,3) = H
         Top(node,4) = 0
         Top(node,5) = 0
         Top(node,6) = 1
         Top(node,7) = (W/n)*(L/m)
         Top(node,8) = (W)*(L)
   end
end
endfunction
Top=S4(n,m)

function [Left]=S5(ii, kk)
   node = 0;
for i = 1:ii
   for k = 1:kk
         node = node + 1;
         Left(node,1) = W/n*(i-0.5)  // Left surface
         Left(node,2) = L/m*0
         Left(node,3) = H/o*(k-0.5)
         Left(node,4) = 0
         Left(node,5) = 1
         Left(node,6) = 0
         Left(node,7) = (W/n)*(H/o)
         Left(node,8) = (W)*(H)
   end
end
endfunction
Left=S5(n,o)

function [Right]=S6(ii, kk)
   node = 0;
for i = 1:ii
   for k = 1:kk
         node = node + 1;
         Right(node,1) = W/n*(i-0.5)  // Right surface
         Right(node,2) = L
         Right(node,3) = H/o*(k-0.5)
         Right(node,4) = 0
         Right(node,5) = 1
         Right(node,6) = 0
         Right(node,7) = (W/n)*(H/o)
         Right(node,8) = (W)*(H)
   end
end
endfunction
Right=S6(n,o)
//VOLUME NODES: Each node holds information of its position in terms of the x,y & z co-ordinates of the node, the volume of the small node as well as the large volume without discretisation.
```

```
node = 0;
for k = 1:o
   for j = 1:m
      for i = 1:n
         node = node + 1;
         Vol(node,1) = W/n*(i-0.5)
         Vol(node,2) = L/m*(j-0.5)
         Vol(node,3) = H/o*(k-0.5)
         Vol(node,4) = (W/n)*(L/m)*(H/o)
         Vol(node,5) = (W)*(L)*(H)
      end
   end
end
//Display all the SURFACE nodes in a matrix:
p=[S1(m,o);S2(m,o);S3(n,m);S4(n,m);S5(n,o);S6(n,o)] //Surface nodes information
//Display all the VOLUME nodes in a matrix:
vp=[Vol] //Volume nodes information

// (2) DIRECT EXCHANGE AEREAS
// The DEA calculation from Surface to Surface:
function [SS_DEA_12]=DEA_1(AA, BB, ii, jj)
node = 0
   for p2=1:jj
      for p1=1:ii
   node = node + 1
         R= sqrt((AA(p1,1)-BB(p2,1)).^2 + (AA(p1,2)-BB(p2,2)).^2 + (AA(p1,3)-BB(p2,3)).^2)
         cos1=(AA(p1,4)*sqrt((AA(p1,1)-BB(p2,1)).^2)+AA(p1,5)*sqrt((AA(p1,2)-BB(p2,2)).^2)+AA(p1,6)*sqrt((AA(p1,3)-
BB(p2,3)).^2))./R
         cos2=(BB(p2,4)*sqrt((AA(p1,1)-BB(p2,1)).^2)+BB(p2,5)*sqrt((AA(p1,2)-BB(p2,2)).^2)+BB(p2,6)*sqrt((AA(p1,3)-
BB(p2,3)).^2))./R
         SS_DEA_12(p1,p2)=((exp(-(Beta).*R)).*((cos1.*cos2.*(AA(p1,7)).*(BB(p2,7))))./((R.^2).*(%pi))
   end
end
endfunction
FF=zeros(m*o,m*o)
FB=DEA_1(Front,Back,m*o,m*o)
FBo=DEA_1(Front,Bottom,m*o,n*m)
FT=DEA_1(Front,Top,m*o,n*m)
FL=DEA_1(Front,Left,m*o,n*o)
FR=DEA_1(Front,Right,m*o,n*o)

BF=DEA_1(Back,Front,m*o,m*o)
BB=zeros(m*o,m*o)
BBo=DEA_1(Back,Bottom,m*o,n*m)
BT=DEA_1(Back,Top,m*o,n*m)
BL=DEA_1(Back,Left,m*o,n*o)
BR=DEA_1(Back,Right,m*o,n*o)

BoF=DEA_1(Bottom,Front,n*m,m*o)
BoB=DEA_1(Bottom,Back,n*m,m*o)
BoBo=zeros(n*m,n*m)
BoT=DEA_1(Bottom,Top,n*m,n*m)
BoL=DEA_1(Bottom,Left,n*m,n*o)
BoR=DEA_1(Bottom,Right,n*m,n*o)

TF=DEA_1(Top,Front,n*m,m*o)
```

```
TB=DEA_1(Top,Back,n*m,m*o)
TBo=DEA_1(Top,Bottom,n*m,n*m)
TT=zeros(n*m,n*m)
TL=DEA_1(Top,Left,n*m,n*o)
TR=DEA_1(Top,Right,n*m,n*o)

LF=DEA_1(Left,Front,n*o,m*o)
LB=DEA_1(Left,Back,n*o,m*o)
LBo=DEA_1(Left,Bottom,n*o,n*m)
LT=DEA_1(Left,Top,n*o,n*m)
LL=zeros(n*o,n*o)
LR=DEA_1(Left,Right,n*o,n*o)

RF=DEA_1(Right,Front,n*o,m*o)
RB=DEA_1(Right,Back,n*o,m*o)
RBo=DEA_1(Right,Bottom,n*o,n*m)
RT=DEA_1(Right,Top,n*o,n*m)
RL=DEA_1(Right,Left,n*o,n*o)
RR=zeros(n*o,n*o)

SS=[FF FB FBo FT FL FR;
    FB BB BBo BT BL BR;
    BoF BoB BoBo BoT BoL BoR;
    TF TB TBo TT TL TR;
    LF LB LBo LT LL LR;
    RF RB RBo RT RL RR]

//Volume-Volume DEAs:
node = 0
   for vp2=1:(n*m*o)
      for vp1=1:(n*m*o)
   node = node + 1
         if ((vp2<>vp1)) then
         R= sqrt((vp(vp1,1)-vp(vp2,1)).^2 + (vp(vp1,2)-vp(vp2,2)).^2 + (vp(vp1,3)-vp(vp2,3)).^2)

         VV(vp2,vp1)=(exp(-(Beta).*R).*(Beta.^2).*((vp(vp1,4)*vp(vp2,4)))./((R.^2).*(%pi))
      else
         VV(vp2,vp1)=0
      end
   end
end

// Volume to Surface DEAs:
function [VS]=DEA_3(SS, s_nodes)
node = 0
   for p1=1:s_nodes  // Number of nodes on the surface
      for vp1=1:n*m*o // Number of nodes in the enclosed volume
   node = node + 1
         R= sqrt((vp(vp1,1)-SS(p1,1)).^2 + (vp(vp1,2)-SS(p1,2)).^2 + (vp(vp1,3)-SS(p1,3)).^2)
         cos1=(SS(p1,4)*sqrt((SS(p1,1)-vp(vp1,1)).^2)+SS(p1,5)*sqrt((SS(p1,2)-vp(vp1,2)).^2)+SS(p1,6)*sqrt((SS(p1,3)-
vp(vp1,3)).^2))./R
         VS(vp1,p1)=((exp(-(Beta).*R)).*((cos1.*Beta.*(SS(p1,7)).*(vp(vp1,4))))./((R.^2).*(%pi))
   end
end
   endfunction
```

```
// DEAs from RIGHT to all the other surfaces;
VF=DEA_3(Front,m*o)
VB=DEA_3(Back,m*o)
VBo=DEA_3(Bottom,n*m)
VT=DEA_3(Top,n*m)
VL=DEA_3(Left,n*o)
VR=DEA_3(Right,n*o)
VS=[VF VB VBo VT VL VR]

// (3) LEAST SQUARES SMOOTHING USING LAGRANGE
XX=[SS VS';VS VV] //All the DEAs assembled into one matrix

//The weights that allow for DEAs to be adjusted proportionally
W=XX.^2
//Totals along rows and columns
for i=1:n_t
   for j=1:n_t
      //Sum of the rows of every column of the DEAs matrix
         AA(1,j)=sum(XX(:,j))
      //Sum of the rows of every column of the weights matrix
         WW(1,j)=sum(W(:,j))
   end
end

//The conservation constraints that must be satisfied
b=[p(:,7)' (4*Beta*vp(:,4))']
C=b-AA

//Weights used to calculate the Lagrange multipliers
R=W+(ones(n_t,1)*WW).*eye(n_t,n_t)

//Lagrange multipliers
L=lsq(R,C')
//Lagrangian transpose for every DEA (rows)
L1=ones(n_t,1)*L'
//Lagrangian for every DEA (columns)
L2=L*(ones(1,n_t))
//Lagrange multipliers for every DEA
lam=L1+L2

//Least squares smoothing using Lagrange multipliers (Smoothed DEAs)
XXX=XX+W.*lam
//Sum of DEAs per surface and Volume
X1=sum(XXX(:,F_n))
X2=sum(XXX(:,B_n))
X3=sum(XXX(:,Bo_n))
X4=sum(XXX(:,T_n))
X5=sum(XXX(:,L_n))
X6=sum(XXX(:,R_n))
X7=sum(XXX(:,n_s+1:n_s+n_v))
SSS=[X1 X2 X3 X4 X5 X6 X7]

//DEAs that can be compared to Tucker
Bo_T_corner=XXX(2*(m*o)+(n*m)+1,2*(m*o)+(n*m))
//disp(Bo_T_corner, 'Bottom to Top corner SS DEA')
Bo_B_corner=XXX(m*o+1,2*(m*o)+(n*m))
```

```
//disp(Bo_B_corner, 'Bottom to Back corner SS DEA')
Bo_V_corner=XXX(2*(m*o)+2*(n*m)+2*(n*o)+1,2*(m*o)+(n*m))
//disp(Bo_V_corner, 'Bottom to corner Volume SV DEA')
V_V_corner=XXX(2*(m*o)+2*(n*m)+2*(n*o)+n*m*o,2*(m*o)+2*(n*m)+2*(n*o)+1)
//disp(V_V_corner, 'Volume to corner Volume VV DEA')

//DEAs extracted from the entire DEAs system
DEA_ss=XXX(1:n_s,1:n_s)  //Surface to surface
DEA_sg=XXX(1:n_s,n_s+1:n_t)
DEA_gs=XXX(n_s+1:n_t,1:n_s)  //Volume to surface
DEA_gg=XXX(n_s+1:n_t,n_s+1:n_t)  //Volume to volume

// Intermediate calculations
bb=[p(:,7)']  // Small areas of the surfaces of the discretised enclosure
Area=ones(n_s,1)*bb  //Areas as a vector
dd=[4*Beta*vp(:,4)']   // 4* extinction coef.*small volume
ddd=[4*abso*vp(:,4)'] // 4* absorption coef.*small volume
B=ones(n_v,1)*ddd    // 4* extinction coef.*small volume as a vector
//Emissivities of the surfaces
e=ones(n_s,1)*eps  // Emissivities as matrix
ee=ones(n_v,1)*eps
//Scattering albedos
ww=wi*ones(1,n_v)
wii=ones(n_v,1)*ww
www=ones(n_s,1)*ww
//Converting the Direct exchange areas to view factors
VF_ss=DEA_ss./Area
VF_gg=DEA_gg./B

//  (4) RADIATION HEAT TRANSFER NETWORK - Zonal method
//Developing the T matrix
for i=1:n_s
   for j=1:n_s
      if j==i then
         T(i,j)=(1/e(i,j))-(VF_ss(i,j).*((1-e(i,j))./e(i,j)))
      else
         T(i,j)=(-1)*VF_ss(i,j).*((1-e(i,j))./e(i,j))
      end
   end
end

// S matrix
S=DEA_ss.*e
// sg matrix
sg=DEA_sg

R=DEA_gs.*ee
Q=(DEA_gs./(ones(n_v,1)*bb)).*((1-ee)./ee)
U=(DEA_sg./(ones(n_s,1)*ddd)).*www

for i=1:n_v
   for j=1:n_v
      if j==i then
         WWW(i,j)=(1/(1-wii(i,j)))-VF_gg(i,j).*wii(i,j)
      else
         WWW(i,j)=(-1)*VF_gg(i,j).*wii(i,j)
```

```
      end
    end
end

V=DEA_sg.*(1-www)
X=DEA_gg.*(1-wii)

C=S+U*lsq(WWW,R)
D=V+U*lsq(WWW,X)
P=T-U*lsq(WWW,Q)

// Emissive powers  [W/m2]
Eb_s=(5.67*(10^-8))*(Temp_s^4)  //Surface Emissive powers  [W/m2]
////////////////////////////////////////////////////////////////
// CASE(1) SPECIFIED SURFACE AND GAS TEMPERAURES
//Eb_g=(5.67*(10^-8))*(Temp_g^4)  //Gas Emissive powers  [W/m2]
//hs=(lsq(P,C)*Eb_s+lsq(P,D)*Eb_g)/1000
//hg=(lsq(WWW,(Q*lsq(P,C)+R))*Eb_s+lsq(WWW,(Q*lsq(P,D)+X))*Eb_g)/1000
//disp(hs, 'Surface irradiation')
////////////////////////////////////////////////////////////////
// CASE (2) SPECIFIED SURFACE TEMPERAURES AND VOLUME HEAT SOURCE (in kW/m3,unknown Tg)
Qgg=HeatSource*vp(:,4)'
Eb_g=(lsq((((eye(n_v,n_v)).*((ones(n_v,1))*ddd))-
lsq(WWW,(Q*lsq(P,D)+X))),(lsq(WWW,(Q*lsq(P,C)+R))*Eb_s+1000*Qgg')))
hg=(lsq(WWW,(Q*lsq(P,C)+R))*Eb_s+lsq(WWW,(Q*lsq(P,D)+X))*Eb_g)/1000
hs=(lsq(P,C)*Eb_s+lsq(P,D)*Eb_g)/1000
Temp_g=abs((Eb_g/(5.67*(10^-8)))^0.25)
////////////////////////////////////////////////////////////////
// Common results
// Surface and gas radiation heat transfer [kW]
Q_s=(((eps.*bb)'.*Eb_s)/1000-hs)
Q_g=(ddd'.*Eb_g)/1000-hg

// Surface and gas radiation heat flux [kW/m2]
q_s=Q_s/bb(1,1)
disp(sum(Q_s), 'Total Q_s transferred in kW')
q_g=Q_g/bb(1,1)
disp(sum(Q_g), 'Total Q_g transferred in kW')
//disp(sum(q_g), 'Total q_g transferred in kW/m2')

Q_overall=sum(Q_s)+sum(Q_g)
//disp(Q_overall, 'Overall Q in kW')

//PLOTS
TempBot=Temp_g(1:n*m,:)
TempExit=Temp_g((o-1)*(n*m)+1:n*m*o,:)
scf(0)  //Bottom Gas Temperature
zm=min(matrix(TempBot,n,m)); zM=max(matrix(TempBot,n,m))
xset("colormap",hotcolormap(32))
colorbar(zm,zM)
surf(matrix(TempBot,n,m),'facecol','interp')

scf(1)  //Exit Gas Temperature
zm=min(matrix(TempExit,n,m)); zM=max(matrix(TempExit,n,m))
xset("colormap",hotcolormap(32))
colorbar(zm,zM)
```

```
surf(matrix(TempExit,n,m),'facecol','interp')

//Surface Radiation Heat Fluxes [W/m2] for each surface
F_flux=q_s(F_n,1)  // FRONT Heat flux in kW/m2
B_flux=q_s(B_n,1)
Bo_flux=q_s(Bo_n,1)
T_flux=q_s(T_n,1)
L_flux=q_s(L_n,1)
R_flux=q_s(R_n,1)
//Plotting the heat flux distributions for each surface
scf(2)  //FRONT surface
zm=min(-matrix(F_flux,o,m)); zM=max(-matrix(F_flux,o,m))
xset("colormap",hotcolormap(32))
colorbar(zm,zM)
surf(-matrix(F_flux,o,m),'facecol','interp')

scf(3)  //BACK surface
zm=min(-matrix(B_flux,o,m)); zM=max(-matrix(B_flux,o,m))
xset("colormap",hotcolormap(32))
colorbar(zm,zM)
surf(-matrix(B_flux,o,m),'facecol','interp')

scf(4)  //BOTTOM surface
zm=min(-matrix(Bo_flux,n,m)); zM=max(-matrix(Bo_flux,n,m))
xset("colormap",hotcolormap(32))
colorbar(zm,zM)
surf(-matrix(Bo_flux,n,m),'facecol','interp')

scf(5)  //TOP surface
zm=min(-matrix(T_flux,n,m)); zM=max(-matrix(T_flux,n,m))
xset("colormap",hotcolormap(32))
colorbar(zm,zM)
surf(-matrix(T_flux,n,m),'facecol','interp')

scf(6)  //LEFT surface
zm=min(-matrix(L_flux,o,n)); zM=max(-matrix(L_flux,o,n))
xset("colormap",hotcolormap(32))
colorbar(zm,zM)
surf(-matrix(L_flux,o,n),'facecol','interp')

scf(7)  //RIGHT surface
zm=min(-matrix(R_flux,o,n)); zM=max(-matrix(R_flux,o,n))
xset("colormap",hotcolormap(32))
colorbar(zm,zM)
surf(-matrix(R_flux,o,n),'facecol','interp')

toc()
disp(toc(), 'time in seconds')
```

E. 2 Secondary case

```
clc
clear
stacksize('max')
currentStackSize = stacksize();
tic()
//INPUTS//////////////////////////////////////////////////////////////////////
// The Dimensions of the enclosure: W,L and H:
W = 1  // Width in the x  direction
L = 1  // Length in the y direction
H = 1  // Height in the direction
// Number of Increments in the W, L and H direction:
n = 4  // Increments in the W (x) direction
m = 4  // Increments in the L (y) direction
o = 4  // Increments in the H (z) direction
n_t=n*m*o+2*(n*o)+2*(m*o)+2*(n*m)  //Total nr of nodes
n_s=2*(n*o)+2*(m*o)+2*(n*m)  // Total nr of surface nodes
n_v=n*m*o  // Total nr of volume nodes
////Surface nodes////
F_n=1:m*o
B_n=m*o+1:2*(m*o)
Bo_n=2*(m*o)+1:2*(m*o)+n*m
T_n=2*(m*o)+(n*m)+1:2*(m*o)+2*(n*m)
L_n=2*(m*o)+2*(n*m)+1:2*(m*o)+2*(n*m)+n*o
R_n=2*(m*o)+2*(n*m)+n*o+1:2*(m*o)+2*(n*m)+2*(n*o)

// SURFACE PROPERTIES
emissivity=0.23  //Surface emissivity
eps=emissivity*ones(1,n_s)  // Emissivities
eps(1,Bo_n)=0.27 //Bottom

// Case 1: Known surface and gas temperatures
Temp_s=1400*ones(n_s,1) //  Surface Temperatures (K)
Temp_s(Bo_n,1)=573
Temp_g=1000*ones(n_v,1) // Medium temperatures (K)

//COAL
coal_density=1346  //kg/m3
coal_D=50*10^(-6)  //m
N_coal=1*10^8 //m^-3
//CHAR
char_density=2200  //kg/m3
char_D=50*10^(-6)  //m
N_char=1*10^8 //m^-3
//FLY-ASH
ash_density=2162  //kg/m3
ash_D=50*10^(-6)  //m
N_ash=1*10^8 //m^-3
//SOOT
soot_density=1999  //kg/m3
soot_D=50*10^(-6)  //m
soot_conc=0.004  //kg/m3
////////////////////////////////////////////////////////////////////
//MODEL DEVELOPMENT
```

```
// (1)  DISCRETISATION OF THE ENCLOSURE
// SURFACE NODES: The enclosure is divided into 6 planes, they are; Front, Back, Bottom, Top, Left & Right].Each node holds information of its position in terms of the x,y & z co-ordinates of the node, the surface normal vector, the area of the small node as well as the large area of the plane without discretisation
function [Front]=S1(jj, kk)
   node = 0;
for j = 1:jj
   for k = 1:kk
         node = node + 1;
         Front(node,1) = W  // Front Surface
         Front(node,2) = L/m*(j-0.5)
         Front(node,3) = H/o*(k-0.5)
         Front(node,4) = 1
         Front(node,5) = 0
         Front(node,6) = 0
         Front(node,7) = (L/m)*(H/o)
         Front(node,8) = (L)*(H)
   end
end
endfunction
Front=S1(m,o)

function [Back]=S2(jj, kk)
   node = 0;
for j = 1:jj
   for k = 1:kk
         node = node + 1;
         Back(node,1) = W/n*0  // Back Surface
         Back(node,2) = L/m*(j-0.5)
         Back(node,3) = H/o*(k-0.5)
         Back(node,4) = 1
         Back(node,5) = 0
         Back(node,6) = 0
         Back(node,7) = (L/m)*(H/o)
         Back(node,8) = (L)*(H)
   end
end
endfunction
Back=S2(m,o)

function [Bottom]=S3(ii, jj)
   node = 0;
for j = 1:jj
   for i = 1:ii
         node = node + 1;
         Bottom(node,1) = W/n*(i-0.5)  // Bottom surface
         Bottom(node,2) = L/m*(j-0.5)
         Bottom(node,3) = H/o*0
         Bottom(node,4) = 0
         Bottom(node,5) = 0
         Bottom(node,6) = 1
         Bottom(node,7) =(W/n)*(L/m)
         Bottom(node,8) = (W)*(L)
   end
end
endfunction
```

```
Bottom=S3(n,m)

function [Top]=S4(ii, jj)
   node = 0;
for j = 1:jj
   for i = 1:ii
         node = node + 1;
         Top(node,1) = W/n*(i-0.5)  // Top surface
         Top(node,2) = L/m*(j-0.5)
         Top(node,3) = H
         Top(node,4) = 0
         Top(node,5) = 0
         Top(node,6) = 1
         Top(node,7) = (W/n)*(L/m)
         Top(node,8) = (W)*(L)
   end
end
endfunction
Top=S4(n,m)

function [Left]=S5(ii, kk)
   node = 0;
for i = 1:ii
   for k = 1:kk
         node = node + 1;
         Left(node,1) = W/n*(i-0.5)  // Left surface
         Left(node,2) = L/m*0
         Left(node,3) = H/o*(k-0.5)
         Left(node,4) = 0
         Left(node,5) = 1
         Left(node,6) = 0
         Left(node,7) = (W/n)*(H/o)
         Left(node,8) = (W)*(H)
   end
end
endfunction
Left=S5(n,o)

function [Right]=S6(ii, kk)
   node = 0;
for i = 1:ii
   for k = 1:kk
         node = node + 1;
         Right(node,1) = W/n*(i-0.5)  // Right surface
         Right(node,2) = L
         Right(node,3) = H/o*(k-0.5)
         Right(node,4) = 0
         Right(node,5) = 1
         Right(node,6) = 0
         Right(node,7) = (W/n)*(H/o)
         Right(node,8) = (W)*(H)
   end
end
endfunction
Right=S6(n,o)
```

```
//disp("The x y & z coordinates of the nodes inside the volume of the  enclosure")
node = 0;
for k = 1:o
   for j = 1:m
      for i = 1:n
         node = node + 1;
         Vol(node,1) = W/n*(i-0.5)
         Vol(node,2) = L/m*(j-0.5)
         Vol(node,3) = H/o*(k-0.5)
         Vol(node,4) = (W/n)*(L/m)*(H/o)
         Vol(node,5) = (W)*(L)*(H)
      end
   end
end

p=[S1(m,o);S2(m,o);S3(n,m);S4(n,m);S5(n,o);S6(n,o)] //Surface nodes information
vp=[Vol] //Volume nodes information
////////////////////////////////////////////////////////////////////
// (2) WEIGHTED SUM OF GRAY GASES MODEL
// Mean beam length
Lm=3.6*(vp(1,5)/p(1,8))
//Truelove's absorption coefficients
abso0=0
abso1=0.267
abso2=4.65
abso3=72
//Truelove weighting factors for WSGG model
a_g0=0.423+(0.0433*10^-3)*Temp_g(1,1)
a_g1=0.285+(0.0513*10^-3)*Temp_g(1,1)
a_g2=0.227+(-0.0676*10^-3)*Temp_g(1,1)
a_g3=0.065+(-0.027*10^-3)*Temp_g(1,1)
// WSGG model total gas emissivity
eps_g=a_g0*(1-exp(-abso0*Lm))+a_g1*(1-exp(-abso1*Lm))+a_g2*(1-exp(-abso2*Lm))+a_g3*(1-exp(-abso3*Lm))
// Effective gas absorption coefficient
abso_g=(1/Lm)*log(1/(1-eps_g))
////////////////////////////////////////////////////////////////////
// APPROXIMATION SPECIFICATIONS
//COAL
n_index_coal=1.85
k_index_coal=0.22
for i=10*%pi:100*%pi
   x_coal(i)=i
end

//CHAR
n_index_char=2.20
k_index_char=1.12
for i=10*%pi:100*%pi
   x_char(i)=i
end

//FLY-ASH
n_index_ash=1.5
k_index_ash=0.02
x_ash=10
```

```
//SOOT
n_index_soot=2.29
k_index_soot=1.49
////////////////////////////////////////////////////////////////////
//EFFICIENCY FACTOR APPROXIMATIONS
//FLY-ASH
rho=2*x_ash*(n_index_ash-1)
phi=atan(k_index_ash/(n_index_ash-1))
Qabs_ash=1+exp(-4*x_ash*k_index_ash)./(2*x_ash*k_index_ash)+(exp(-4*x_ash*k_index_ash)-
1)./(8*x_ash^2*k_index_ash^2)
Qext_1_ash=4*exp(-rho.*tan(phi)).*(cos(phi)./rho).*sin(rho-phi)
Qext_2_ash=4*exp(-rho.*tan(phi)).*((cos(phi)./rho)^2).*cos(rho-2*phi)
Qext_3_ash=4*((cos(phi)./rho)^2).*cos(2*phi)
Qext_ash=2-Qext_1_ash-Qext_2_ash+Qext_3_ash
Qsca_ash=Qext_ash-Qabs_ash
//COAL
Qext_coal=2
q_1=(n_index_coal*k_index_coal)^(-0.5)
q_2=2/q_1
f_1=(8/q_1^2)*(q_1-log(1+q_1+0.5*q_1^2))
f_2=(8/q_2^2)*(q_2-log(1+q_2+0.5*q_2^2))
Qabs_coal=0.5*(f_1+f_2)
Qsca_coal=Qext_coal-Qabs_coal
//CHAR
Qext_char=2
q_1_char=(n_index_char*k_index_char)^(-0.5)
q_2_char=2/q_1
f_1_char=(8/q_1_char^2)*(q_1_char-log(1+q_1_char+0.5*q_1_char^2))
f_2_char=(8/q_2_char^2)*(q_2_char-log(1+q_2_char+0.5*q_2_char^2))
Qabs_char=0.5*(f_1_char+f_2_char)
Qsca_char=Qext_char-Qabs_char
//SOOT
C_0_d=(n_index_soot^2-k_index_soot^2+2)^2+4*n_index_soot^2*k_index_soot^2
C_0=(36*%pi*n_index_soot*k_index_soot)/(C_0_d)
C_2=1.4388*10^(-2)
fv_soot=10^(-8)  //soot_conc/soot_density
Qabs_soot=(3.72*fv_soot*C_0*Temp_g)/C_2
Qsca_soot=0 //Qext_soot-Qabs_soot
////////////////////////////////////////////////////////////////////
//ABSORPTION & SCATTERING COEFFICIENTS
coal_abs=N_coal*%pi*coal_D^2*Qabs_coal/4
coal_sca=N_coal*%pi*coal_D^2*Qsca_coal/4

char_abs=N_char*%pi*char_D^2*Qabs_char/4
char_sca=N_char*%pi*char_D^2*Qsca_char/4

ash_abs=N_ash*%pi*ash_D^2*Qabs_ash/4
ash_sca=N_ash*%pi*ash_D^2*Qsca_ash/4

soot_abs=(3.72*fv_soot*C_0*mean(Temp_g))/C_2
soot_sca=0

coef=[coal_abs coal_sca;
char_abs ash_sca;
ash_abs coal_sca;
soot_abs soot_sca]
```

```
disp(coef)
////////////////////////////////////////////////////////////////
//ABSORPTION & SCATTERING COEFFICIENTS OF PARTICULATE MEDIUM
abso_p=coal_abs+char_abs+ash_abs+soot_abs
scat_p=coal_sca+char_sca+ash_sca+soot_sca
particle=[abso_p scat_p]
disp(particle, 'Abs & Sca coefficients for particles')
////////////////////////////////////////////////////////////////
//Radiative properties of the participating medium
abso=abso_g+abso_p
Beta = abso+scat_p // Extinction coefficient
wi=scat_p/Beta //scattering/Beta - Scattering albedo =0

//(3) DIRECT EXCHANGE AEREAS
// The DEA calculation from Surface to Surface:
function [SS_DEA_12]=DEA_1(AA, BB, ii, jj)
node = 0
  for p2=1:jj
    for p1=1:ii
  node = node + 1
      R= sqrt((AA(p1,1)-BB(p2,1)).^2 + (AA(p1,2)-BB(p2,2)).^2 + (AA(p1,3)-BB(p2,3)).^2)
      cos1=(AA(p1,4)*sqrt((AA(p1,1)-BB(p2,1)).^2)+AA(p1,5)*sqrt((AA(p1,2)-BB(p2,2)).^2)+AA(p1,6)*sqrt((AA(p1,3)-
BB(p2,3)).^2))./R
      cos2=(BB(p2,4)*sqrt((AA(p1,1)-BB(p2,1)).^2)+BB(p2,5)*sqrt((AA(p1,2)-BB(p2,2)).^2)+BB(p2,6)*sqrt((AA(p1,3)-
BB(p2,3)).^2))./R
      SS_DEA_12(p1,p2)=((exp(-(Beta).*R)).*((cos1.*cos2.*(AA(p1,7)).*(BB(p2,7))))./((R.^2).*(%pi))
  end
end
endfunction
FF=zeros(m*o,m*o)
FB=DEA_1(Front,Back,m*o,m*o)
FBo=DEA_1(Front,Bottom,m*o,n*m)
FT=DEA_1(Front,Top,m*o,n*m)
FL=DEA_1(Front,Left,m*o,n*o)
FR=DEA_1(Front,Right,m*o,n*o)

BF=DEA_1(Back,Front,m*o,m*o)
BB=zeros(m*o,m*o)
BBo=DEA_1(Back,Bottom,m*o,n*m)
BT=DEA_1(Back,Top,m*o,n*m)
BL=DEA_1(Back,Left,m*o,n*o)
BR=DEA_1(Back,Right,m*o,n*o)

BoF=DEA_1(Bottom,Front,n*m,m*o)
BoB=DEA_1(Bottom,Back,n*m,m*o)
BoBo=zeros(n*m,n*m)
BoT=DEA_1(Bottom,Top,n*m,n*m)
BoL=DEA_1(Bottom,Left,n*m,n*o)
BoR=DEA_1(Bottom,Right,n*m,n*o)

TF=DEA_1(Top,Front,n*m,m*o)
TB=DEA_1(Top,Back,n*m,m*o)
TBo=DEA_1(Top,Bottom,n*m,n*m)
TT=zeros(n*m,n*m)
TL=DEA_1(Top,Left,n*m,n*o)
TR=DEA_1(Top,Right,n*m,n*o)
```

```
LF=DEA_1(Left,Front,n*o,m*o)
LB=DEA_1(Left,Back,n*o,m*o)
LBo=DEA_1(Left,Bottom,n*o,n*m)
LT=DEA_1(Left,Top,n*o,n*m)
LL=zeros(n*o,n*o)
LR=DEA_1(Left,Right,n*o,n*o)

RF=DEA_1(Right,Front,n*o,m*o)
RB=DEA_1(Right,Back,n*o,m*o)
RBo=DEA_1(Right,Bottom,n*o,n*m)
RT=DEA_1(Right,Top,n*o,n*m)
RL=DEA_1(Right,Left,n*o,n*o)
RR=zeros(n*o,n*o)

SS=[FF FB FBo FT FL FR;
    FB BB BBo BT BL BR;
    BoF BoB BoBo BoT BoL BoR;
    TF TB TBo TT TL TR;
    LF LB LBo LT LL LR;
    RF RB RBo RT RL RR]

//Volume-Volume DEAs:
node = 0
   for vp2=1:(n*m*o)
      for vp1=1:(n*m*o)
   node = node + 1
         if ((vp2<>vp1)) then
         R= sqrt((vp(vp1,1)-vp(vp2,1)).^2 + (vp(vp1,2)-vp(vp2,2)).^2 + (vp(vp1,3)-vp(vp2,3)).^2)

         VV(vp2,vp1)=(exp(-(Beta).*R).*(Beta.^2).*((vp(vp1,4)*vp(vp2,4)))./((R.^2).*(%pi))
      else
         VV(vp2,vp1)=0
      end
   end
end

// Volume to Surface DEAs:
function [VS]=DEA_3(SS, s_nodes)
node = 0
   for p1=1:s_nodes  // Number of nodes on the surface
      for vp1=1:n*m*o // Number of nodes in the enclosed volume
   node = node + 1
         R= sqrt((vp(vp1,1)-SS(p1,1)).^2 + (vp(vp1,2)-SS(p1,2)).^2 + (vp(vp1,3)-SS(p1,3)).^2)
         cos1=(SS(p1,4)*sqrt((SS(p1,1)-vp(vp1,1)).^2)+SS(p1,5)*sqrt((SS(p1,2)-vp(vp1,2)).^2)+SS(p1,6)*sqrt((SS(p1,3)-
vp(vp1,3)).^2))./R
         VS(vp1,p1)=((exp(-(Beta).*R)).*((cos1.*Beta.*(SS(p1,7)).*(vp(vp1,4)))))./((R.^2).*(%pi))
   end
end
   endfunction

// DEAs from RIGHT to all the other surfaces;
VF=DEA_3(Front,m*o)
VB=DEA_3(Back,m*o)
VBo=DEA_3(Bottom,n*m)
VT=DEA_3(Top,n*m)
```

```
VL=DEA_3(Left,n*o)
VR=DEA_3(Right,n*o)
VS=[VF VB VBo VT VL VR]

// (4) LEAST SQUARES SMOOTHING USING LAGRANGE
XX=[SS VS';VS VV] //All the DEAs assembled into one matrix

//The weights that allow for DEAs to be adjusted proportionally
W=XX.^2
//Totals along rows and columns
for i=1:n_t
   for j=1:n_t
      //Sum of the rows of every column of the DEAs matrix
         AA(1,j)=sum(XX(:,j))
      //Sum of the rows of every column of the weights matrix
         WW(1,j)=sum(W(:,j))
   end
end

//The conservation constraints that must be satisfied
b=[p(:,7)' (4*Beta*vp(:,4))']
C=b-AA

//Weights used to calculate the Lagrange multipliers
R=W+(ones(n_t,1)*WW).*eye(n_t,n_t)

//Lagrange multipliers
L=lsq(R,C')
//Lagrangian transpose for every DEA (rows)
L1=ones(n_t,1)*L'
//Lagrangian for every DEA (columns)
L2=L*(ones(1,n_t))
//Lagrange multipliers for every DEA
lam=L1+L2

//Least squares smoothing using Lagrange multipliers (Smoothed DEAs)
XXX=XX+W.*lam
//Sum of DEAs per surface and Volume
X1=sum(XXX(:,F_n))
X2=sum(XXX(:,B_n))
X3=sum(XXX(:,Bo_n))
X4=sum(XXX(:,T_n))
X5=sum(XXX(:,L_n))
X6=sum(XXX(:,R_n))
X7=sum(XXX(:,n_s+1:n_s+n_v))
SSS=[X1 X2 X3 X4 X5 X6 X7]

//DEAs that can be compared to Tucker
Bo_T_corner=XXX(2*(m*o)+(n*m)+1,2*(m*o)+(n*m))
//disp(Bo_T_corner, 'Bottom to Top corner SS DEA')
Bo_B_corner=XXX(m*o+1,2*(m*o)+(n*m))
//disp(Bo_B_corner, 'Bottom to Back corner SS DEA')
Bo_V_corner=XXX(2*(m*o)+2*(n*m)+2*(n*o)+1,2*(m*o)+(n*m))
//disp(Bo_V_corner, 'Bottom to corner Volume SV DEA')
V_V_corner=XXX(2*(m*o)+2*(n*m)+2*(n*o)+n*m*o,2*(m*o)+2*(n*m)+2*(n*o)+1)
//disp(V_V_corner, 'Volume to corner Volume VV DEA')
```

```
//DEAs extracted from the entire DEAs system
DEA_ss=XXX(1:n_s,1:n_s)  //Surface to surface
DEA_sg=XXX(1:n_s,n_s+1:n_t)
DEA_gs=XXX(n_s+1:n_t,1:n_s)  //Volume to surface
DEA_gg=XXX(n_s+1:n_t,n_s+1:n_t)  //Volume to volume

// Intermediate calculations
bb=[p(:,7)']  // Small areas of the surfaces of the discretised enclosure
Area=ones(n_s,1)*bb  //Areas as a vector
dd=[4*Beta*vp(:,4)']  // 4* extinction coef.*small volume
ddd=[4*abso*vp(:,4)']
B=ones(n_v,1)*ddd  // 4* extinction coef.*small volume as a vector
e=ones(n_s,1)*eps  // Emissivities as matrix
ee=ones(n_v,1)*eps
//Scattering albedos
ww=wi*ones(1,n_v)
wii=ones(n_v,1)*ww
www=ones(n_s,1)*ww
//Converting the Direct exchange areas to view factors
VF_ss=DEA_ss./Area
VF_gg=DEA_gg./B
////////////////////////////////////////////////////////////////
// (5) RADIATION HEAT TRANSFER NETWORK - Zonal method
//Developing the T matrix
for i=1:n_s
   for j=1:n_s
      if j==i then
         T(i,j)=(1/e(i,j))-(VF_ss(i,j).*((1-e(i,j))./e(i,j)))
      else
         T(i,j)=(-1)*VF_ss(i,j).*((1-e(i,j))./e(i,j))
      end
   end
end

// S matrix
S=DEA_ss.*e
// sg matrix
sg=DEA_sg

R=DEA_gs.*ee
Q=(DEA_gs./(ones(n_v,1)*bb)).*((1-ee)./ee)
U=(DEA_sg./(ones(n_s,1)*ddd)).*www

for i=1:n_v
   for j=1:n_v
      if j==i then
         WWW(i,j)=(1/(1-wii(i,j)))-VF_gg(i,j).*wii(i,j)
      else
         WWW(i,j)=(-1)*VF_gg(i,j).*wii(i,j)
      end
   end
end

V=DEA_sg.*(1-www)
X=DEA_gg.*(1-wii)
```

```
C=S+U*lsq(WWW,R)
D=V+U*lsq(WWW,X)
P=T-U*lsq(WWW,Q)

//Total exchange areas
YY=[T -U;-Q WWW]
ZZ=[S V;R X]
TEAs=lsq(YY,ZZ)
TEAs_SS=TEAs(1:n_s,1:n_s)
TEAs_SG=TEAs(1:n_s,n_s+1:n_t)
TEAs_GS=TEAs_SG'
TEAs_GG=TEAs(n_s+1:n_t,n_s+1:n_t)

Test1=sum(TEAs(1,:))
Test2=sum(TEAs(:,n_t))

// Emissive powers  [W/m2]
Eb_s=(5.67*(10^-8))*(Temp_s^4)  //Surface Emissive powers  [W/m2]
Eb_g=(5.67*(10^-8))*(Temp_g^4)  //Gas Emissive powers  [W/m2]
////////////////////////////////////////////////////////////////
// CASE (1) SPECIFIED SURFACE AND GAS TEMPERAURES
hs=(lsq(P,C)*Eb_s+lsq(P,D)*Eb_g)/1000
hg=(lsq(WWW,(Q*lsq(P,C)+R))*Eb_s+lsq(WWW,(Q*lsq(P,D)+X))*Eb_g)/1000
//disp(hs, 'Surface irradiation')
//disp(hg)

// (2) SPECIFIED SURFACE TEMPERAURES AND VOLUME HEAT SOURCE (in kW/m3,unknown Tg)
//HeatSource=5
//Qgg=HeatSource*vp(:,4)'
//Eb_g=(lsq((((eye(n_v,n_v)).*((ones(n_v,1))*ddd))-
lsq(WWW,(Q*lsq(P,D)+X))),(lsq(WWW,(Q*lsq(P,C)+R))*Eb_s+1000*Qgg')))
//hg=(lsq(WWW,(Q*lsq(P,C)+R))*Eb_s+lsq(WWW,(Q*lsq(P,D)+X))*Eb_g)/1000
//hs=(lsq(P,C)*Eb_s+lsq(P,D)*Eb_g)/1000
//Temp_g=abs((Eb_g/(5.67*(10^-8)))^0.25)
////////////////////////////////////////////////////////////////
// Common results
// Surface and gas radiation heat transfer [kW]
Q_s=(((eps.*bb)'.*Eb_s)/1000-hs)
Q_s_alternative=(((eps.*bb)'.*Eb_s)-(TEAs_SS'*Eb_s)-(TEAs_SG*Eb_g))/1000   //kW
Q_g=(ddd'.*Eb_g)/1000-hg
Q_g_alternative=(dd'.*Eb_g-(TEAs_GS*Eb_s)-(TEAs_GG*Eb_g))/1000   //kW

// Surface and gas radiation heat flux [kW/m2]
q_s=Q_s/bb(1,1)
disp(sum(Q_s), 'Total Q_s transferred in kW')
q_g=Q_g/bb(1,1)
disp(sum(Q_g), 'Total Q_g transferred in kW')
//disp(sum(q_g), 'Total q_g transferred in kW/m2')
Q_overall=sum(Q_s)+sum(Q_g)
//disp(Q_overall, 'Overall Q in kW')

disp(sum(Q_s(F_n,1)))
disp(sum(Q_s(B_n,1)))
disp(sum(Q_s(Bo_n,1)))
disp(sum(Q_s(T_n,1)))
```

```
disp(sum(Q_s(L_n,1)))
disp(sum(Q_s(R_n,1)))
////////////////////////////////////////////////////////////////
//PLOTS
TempBot=Temp_g(1:n*m,:)
TempExit=Temp_g((o-1)*(n*m)+1:n*m*o,:)
scf(0)  //Bottom Gas Temperature
zm=min(matrix(TempBot,n,m)); zM=max(matrix(TempBot,n,m))
xset("colormap",hotcolormap(32))
colorbar(zm,zM)
surf(matrix(TempBot,n,m),'facecol','interp')

scf(1)  //Exit Gas Temperature
zm=min(matrix(TempExit,n,m)); zM=max(matrix(TempExit,n,m))
xset("colormap",hotcolormap(32))
colorbar(zm,zM)
surf(matrix(TempExit,n,m),'facecol','interp')

//Surface Radiation Heat Fluxes [W/m2] for each surface
F_flux=q_s(F_n,1)  // FRONT Heat flux in kW/m2
B_flux=q_s(B_n,1)
Bo_flux=q_s(Bo_n,1)
T_flux=q_s(T_n,1)
L_flux=q_s(L_n,1)
R_flux=q_s(R_n,1)
//Plotting the heat flux distributions for each surface
scf(2)  //FRONT surface
zm=min(-matrix(F_flux,o,m)); zM=max(-matrix(F_flux,o,m))
xset("colormap",hotcolormap(32))
colorbar(zm,zM)
surf(-matrix(F_flux,o,m),'facecol','interp')

scf(3)  //BACK surface
zm=min(-matrix(B_flux,o,m)); zM=max(-matrix(B_flux,o,m))
xset("colormap",hotcolormap(32))
colorbar(zm,zM)
surf(-matrix(B_flux,o,m),'facecol','interp')

scf(4)  //BOTTOM surface
zm=min(-matrix(Bo_flux,n,m)); zM=max(-matrix(Bo_flux,n,m))
xset("colormap",hotcolormap(32))
colorbar(zm,zM)
surf(-matrix(Bo_flux,n,m),'facecol','interp')

scf(5)  //TOP surface
zm=min(-matrix(T_flux,n,m)); zM=max(-matrix(T_flux,n,m))
xset("colormap",hotcolormap(32))
colorbar(zm,zM)
surf(-matrix(T_flux,n,m),'facecol','interp')

scf(6)  //LEFT surface
zm=min(-matrix(L_flux,o,n)); zM=max(-matrix(L_flux,o,n))
xset("colormap",hotcolormap(32))
colorbar(zm,zM)
surf(-matrix(L_flux,o,n),'facecol','interp')
```

```
scf(7)  //RIGHT surface
zm=min(-matrix(R_flux,o,n)); zM=max(-matrix(R_flux,o,n))
xset("colormap",hotcolormap(32))
colorbar(zm,zM)
surf(-matrix(R_flux,o,n),'facecol','interp')

toc()
disp(toc(), 'time in seconds')
```